Theoretical Atomic Spectroscopy of Earthbound and Stellar Plasma

Grumer, Jon

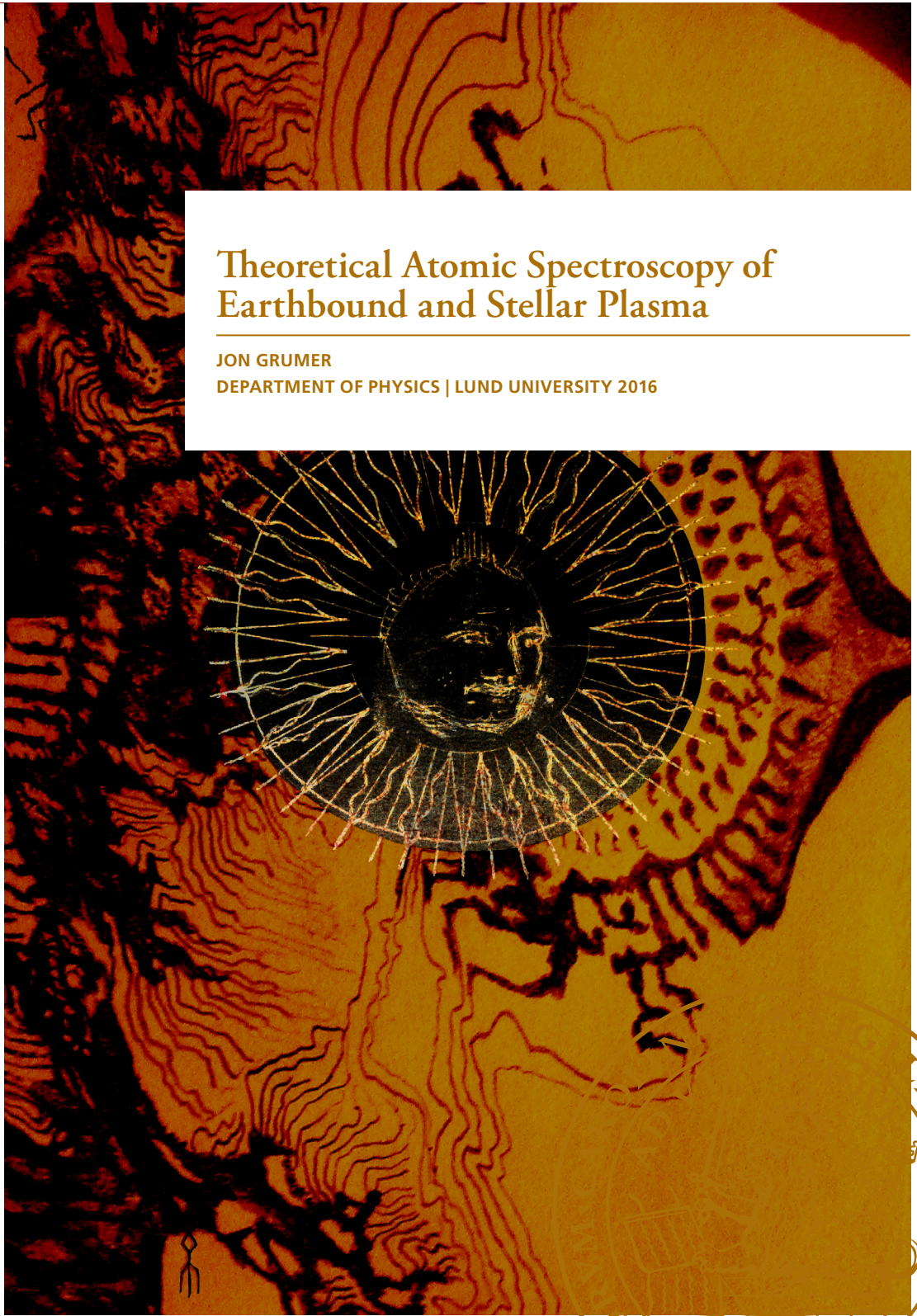

Theoretical Atomic Spectroscopy of Earthbound and Stellar Plasma

JON GRUMER
DEPARTMENT OF PHYSICS | LUND UNIVERSITY 2016

THEORETICAL ATOMIC SPECTROSCOPY OF EARTHBOUND AND STELLAR PLASMA

Jon Grumer

LUND
UNIVERSITY

2016

Thesis for the degree of Doctor of Philosophy

Department of Physics
Faculty of Science
Lund University

Thesis advisor:
Tomas Brage

Thesis co-advisors:
Per Jönsson and *Gediminas Gaigalas*

Faculty opponent:
Eva Lindroth

To be presented, with the permission of the Faculty of Science at Lund University, for public criticism in the Rydberg lecture hall (Rydbergsalen) at the Department of Physics, on the 21st of October 2016 at 9:15.

Organization	Document name
LUND UNIVERSITY Department of Physics Box 118 221 00 LUND Sweden	**DOCTORAL DISSERTATION** **Date of disputation** 2016-10-21 **Sponsoring organization**
Author(s) Jon Grumer	

Title and subtitle
Theoretical Atomic Spectroscopy of Earthbound and Stellar Plasma

Abstract
Motivated by spectroscopic analysis of astrophysical and laboratory plasma, this thesis concerns the fundamental structure and spectral properties of atoms and their ions. The *multiconfiguration Dirac-Hartree-Fock* (MCDHF) method is used to predict the emission or absorption of radiation, by atomic systems in general, and of heavy and highly charged ions in particular.

The first set of publications, paper A_I to A_{VII}, concerns ab-initio predictions of atomic structure and radiative transition rates, with a particular focus on *relativistic* and *electron-correlation effects*. Systematic and large-scale MCDHF calculations have been carried out, often in combination with *electron-beam ion trap* experiments.

The second set, B_I to B_{VIII}, presents a rigorous treatment of effects from non-spherical interactions with certain nuclei - *hyperfine interaction* - and external magnetic fields - *Zeeman interaction* - on atomic spectra. A general methodology has been developed and implemented in computer codes to include these perturbations in the wavefunctions and to determine their impact on the resulting spectra. Of particular interest are spectral *intensity redistributions* and *unexpected transitions*, and their applications to stellar abundance analyses, magnetic-fields effects in storage-ring experiments, and coronal magnetic-field measurements.

Key Words
atomic structure, atomic processes, electron correlation, spectroscopy, hyperfine structure, magnetic fields

Classification system and/or index terms (if any)

Supplementary bibliographical information	Language
	English
ISSN and key title	**ISBN**
	978-91-7623-996-4 (print) 978-91-7623-997-1 (pdf)
Recipient's notes	**Number of pages** 368 / **Price**
	Security classification

Theoretical Atomic Spectroscopy of Earthbound and Stellar Plasma

Cover Illustration:
Lalla Oledal

ISBN: 978-91-7623-996-4 (print)
ISBN: 978-91-7623-997-1 (pdf)

Printed in Sweden by Media-Tryck, Lund University, Lund 2016

POPULAR SUMMARY (IN SWEDISH)

Ljus är verkligen fantastiskt. Det kan ge oss känslomässiga upplevelser, som när det faller genom en trädkrona i en skog eller vid en blodröd fullmåne, men det gör det också möjligt för oss att uppfatta och förstå vår omgivning. Majoriteten av den information vi kan tillgodogöra oss om Universum, får vi genom det ljus som atomer och joner i olika kosmiska objekt sänder ut. Varje foton - den minsta energimängd ljus som kan överföra information - bär information i form av energi med en viss intensitet och våglängd. För att komma åt denna information låter man det till synes enfärgade ljuset, falla genom ett prisma så att det delas upp i färger av olika våglängder – ett så kallat spektrum.

Stjärnor, som vår egen sol, sänder ut ljus av alla våglängder, och den uppfattade färgen är ett mått på stjärnans temperatur, precis så som färgen på en järnbit ändras från gult, via violett och blått, till rött under upphettning. Undersöker man stjärnspektrumet närmare så upptäcker man smala mörka band som bryter av den kontinuerliga färgfördelningen. Dessa linjer uppstår då ljuset passerar genom stjärnans atmosfär och där delvis absorberas av atomer, joner eller molekyler. Ett exempel på ett sådant absorptionsspektrum från Solen visas i figur 1.1 på sida 5 i kapitel 1.

Varje grundämne i periodiska tabellen har ett helt eget unikt fingeravtryck med avseende på vilka våglängder det kan absorbera eller avge i form av fotoner. Så, genom att studera exempelvis absorptionsspektra från stjärnor, och jämföra med spektra för enskilda atomer eller joner bestämda via experiment i laboratorier eller matematiska modeller, kan vi bestämma vilka ämnen som absorberade det kontinuerliga ljuset och skapade de mörka absorptionslinjerna. Vet vi dessutom hur mycket ljus som olika ämnen förväntas

absorbera vid en viss färg, så kan vi bestämma den totala kemiska sammansättningen i stjärnans atmosfär. Det har visat sig att ytterligare information om miljön i vilken atomen befinner sig, såsom temperaturer, densiteter eller styrkan på magnetfält, också kan bestämmas på detta sätt.

Den här avhandlingen handlar om atomer och deras joner, och att genom kvantmekaniska modeller och datorsimuleringar förutsäga deras egenskaper, för just sådana syften som vid studier av stjärnatmosfärer. Av särskilt intresse är hur atomer påverkas av omgivande magnetfält, i exempelvis solens yttre atmosfär – den s.k. koronan. Även om Solen är den stjärna vi känner bäst, så är en av de största gåtorna för astronomer hur koronan kan ha en temperatur på miljontals °C, då solens yta endast är ungefär 6000 °C. Ett relaterat mysterium är vad för slags processer som ger upphov till de kraftfulla solstormar som, om de träffar jorden, ger upphov till norrsken, men kan också slå ut teknisk utrustning. Figure 1.3 på sida 10 visar en bild på enså kallad korona-massutkastning, som när den träffade jorden ett par dagar senare gav uppphov till kraftfullt norrsken. Ett exempel är från 2003 då 50 000 Malmöbor strömlösa under en timmes tid, och den bakomliggande orsaken tros vara jordmagnetiska strömmar orsakade av solstormar. Ett annat exempel är då Karlstads telefonstation natten till pingstdagen 1921, fattade eld på grund strömmar inducerade av en kraftig solstorm, med skador som förvärrades ytterligare av att även larmsystemet till brandkåren slogs ut[1]. Förklaringarna till solstormarna tros ligga i komplexa processer i de magnetfält som omsveper Solens yta. I dagsläget finns det dock inte några tillförlitliga metoder för att undersöka magnetfälten i koronan.

I den här avhandlingen undersöker vi, bland annat, en alternativ metod för att mäta magnetfälten i Solens atmosfär, med målet att förutsäga det så kallade rymdvädret.

1 Den totala kostnaden för branden och skadorna efter solstormen beräknades uppgå till 200 000 kronor, och anläggningen var försäkrad till 177 000 kronor. Försäkringen hade dock nyligen sagts upp av besparingskäl.

ACKNOWLEDGMENTS

During my time as a PhD student I have been privileged with working and socializing with so many kind and interesting people. In one way or another you have all contributed to this thesis. However, some have contributed more than others and deserve to be separately mentioned.

First of all, I would like to express my deepest gratitude to my supervisors, Tomas, Per and Gediminas. Thank you for these fantastic years; in the beginning you were my colleagues, and now you are also my close friends. To have supervisors which complement each other in the way you do, is something I have valued to inestimable amounts.

Next I would like to mention Martin and Yao Yan who took such good care of me the first time I came to Shanghai in 2009 for my Master's thesis. Martin, this thesis would not have been what it is without you!

When talking about Shanghai, I have to mention Roger at the Shanghai EBIT Lab. You are the best, Captain. I also want to express my gratitude to LuDi, I couldn't agree more with Martin: If anyone ever needs a fixer, he is the one to employ. I also want to especially mention Wenxian, for her hard work and for being one of the kinder persons I have met. Good luck in Boulder!

The division of mathematical physics at the department of physics in Lund. This is a great place to work! Not only because Katarina take such good care of all of us, but also because the atmosphere is so friendly and inspiring. Thank you all. I would also like to express my gratitude to Lennart, Florido and Gabrielle for always being there when I was in need of computer support, and also for

all the interesting conversations!

I want to express my particular gratitude to Charlotte for being my biggest inspiration of all, and for taking fantastic good care of me during my months at NIST in Maryland. I also want take the opportunity to thank all the other members of the Computational Atomic Structure (CompAS) team: Ian, Alan, Michel, Jacek, Pavel, Thomas, Simon, Laima, Livio and all you others for all the support and for all the fun times we have had!

The Lund-Malmö Centre for Atomic Systems (LUMCAS) - thank you Jörgen, Hampus, Henrik, Asli, Sven, Stefan, Rickard, Lennart, Lars, Hans and all the rest of you for fantastic years!

The teaching department at the science faculty (UDIF) - thank you Per-Olof, Car-Eric, Mikael and all you others for creating an incredible and, to my experience, unique teaching atmosphere!

I also want to thank Anders, Inga and Ola for housing me during the first years of my time in Lund - this was a fantastic time, you will always be close to me!

Huge hugs to all my friends at Möllan (and V. Hamnen - yes that's you Fredrik) in Malmö - you know who you are. I would especially like to thank Viktor, Johannes, Fredrik and David who all have stood by my side during the past years. And to Lalla, who is a huge inspiration to me, and who also made this thesis so much more interesting with the fantastic cover illustration!

At last I would like to give the biggest of thanks to my parents, Anne and Clas, and to my siblings, Signe and Magnus, and to the rest of my family for all the love and support they have given me through the years. Tack!

Peace out / Jon

SUMMARY OF PUBLICATIONS

The thesis is based on the results presented in the following peer-reviewed articles. The articles are independent although conveniently classified into two main groups, labeled A and B, and presented in projects when felt appropriate. Author contributions are given after each summary.

Group A: Accurate *multiconfiguration Dirac-Hartree-Fock* (MCDHF) calculations of atomic structure and radiative properties, large-scale *spectrum calculations* and *forbidden-line spectroscopy* for fusion- and astrophysical plasma diagnostics.

Group B: Rigorous treatment of effects from non-spherical perturbations from the nucleus (hyperfine interactions) and external magnetic fields (Zeeman interactions) on radiative atomic spectra as well as the development of a general methodology to include these symmetry-breaking perturbations in the wavefunctions and to determine radiative properties. In particular, these publications concern *intensity redistributions* and *unexpected transitions* in atomic spectra, and their applications to plasma diagnostics for abundance analyses in stellar atmospheres, the impact of magnetic fields in storage rings as well as coronal magnetic field measurements and, ultimately, space-weather meteorology.

Papers A_I and A_{II}: *Large-scale spectrum calculations with applications in fusion and astrophysical plasma diagnostics.*

[A_I] **Energy levels and radiative data for Kr-like W^{38+} from MCDHF and RMBPT calculations**
X. Guo, J. Grumer, T. Brage, R. Si, C. Chen, P. Jönsson, K. Wang, J. Yan, R. Hutton, and Y. Zou
J. Phys. B: At. Mol. Opt. Phys. **49** 13 (2016)

[A_{II}] **A spectral study of Te V from MCDHF calculations**
J. Ekman, J. Grumer, H. Hartman, and P. Jönsson
J. Phys. B: At. Mol. Opt. Phys. **46** 9 (2013)

Summary: These two papers address what could be termed *spectrum calculations* - systematic and accurate ab-initio calculations of a range of atomic eigenstates up to a certain excitation energy limit, as well as relevant radiative transition properties. The application of paper A_I, which concerns a detailed theoretical analysis of Kr-like W, is fusion plasma diagnostics; of particular relevance to the ~ €13 billion ITER fusion reactor under construction in southern France. In paper A_{II} we report on a spectrum calculation of four time ionized tellurium (Te V). With a cosmic abundance larger than for any element with atomic number greater than 40, Te is one of the most important heavy elements in astronomical studies. Detailed understanding of its atomic structure and spectra is therefore of great importance to analyze astronomical spectra for determination of e.g. element abundances in stars.

Contributions: For the scientific work presented in publication A_I, I was acting as supervisor for X.G., who was visiting us in Lund from Fudan University in Shanghai to learn about calculations with the GRASP2K code during some months in 2015. As a supervisor I took part in essentially all steps of the MCDHF modeling, as well as in the preparation of the manuscript, and lead the submission procedure. Paper A_{II} was done in close collaboration with J.E., who was driving the project. I took part in the design of the theoretical model, performed parts of the calculations, and contributed to the preparation of the manuscript, although the first version was mainly compiled by J.E.

Papers A_{III} to A_{VI}: *Forbidden-line spectroscopy of ions relevant to fusion plasma diagnostics.*

[A_{III}] **The M1 ground state fine structure transition in Ag-like Yb**
R. Zhao, J. Grumer, W. Li, J. Xiao, T. Brage, S. Huldt, R. Hutton, and Y. Zou
J. Phys. B: At. Mol. Opt. Phys. **47** 18 (2014)

[A_{IV}] **Coronal lines and the importance of deep-core–valence correlation in Ag-like ions**
J. Grumer, R. Zhao, T. Brage, W. Li, S. Huldt, R. Hutton, and Y. Zou
Phys. Rev. A **89** 6 (2014)

[A_{V}] **Forbidden-line spectroscopy of the ground-state configuration of Cd-like W**
Z. Fei, W. Li, J. Grumer, Z. Shi, R. Zhao, T. Brage, S. Huldt, K. Yao, R. Hutton, and Y. Zou
Phys. Rev. A **90** 5 (2014)

[A_{VI}] **Experimental and theoretical study of the ground-state M1 transition in Ag-like tungsten**
Z. Fei, R. Zhao, Z. Shi, J. Xiao, M. Qiu, J. Grumer, M. Andersson, T. Brage, R. Hutton, and Y. Zou
Phys. Rev. A **86** 6 (2012)

Summary: This set of papers tells a story about accurate determination of forbidden lines in open f-shell ground-configurations in heavy and highly ionized atomic systems, using a combination of *electron-beam ion trap* (EBIT) experiments and theoretical modeling in what could be called forbidden-line spectroscopy. The main motivation of this project was to understand the formation of forbidden lines in laboratory plasma, such as the tokamak plasma in the ITER fusion reactor, starting with a detailed analysis of highly ionized Ag-like ions with ground state configuration $4f$, and later expanded to the more complex Cd-like system with a $4f^2$ ground configuration at the high end of the isoelectronic sequence.

The Ag-like system consists of a single M1 transition, which requires very high accuracy for a trustworthy spectroscopic identification. Using the theoretical model developed in paper A_{VI}, which was further enhanced and analyzed in paper A_{IV}, we identify this line in Ag-like W and Yb, as presented in paper A_{VI} and A_{III} respectively. In paper A_V we analyze the ground configuration of highly ionized Cd-like ions, which consists of 13 fine structure levels connected by a number of forbidden transition. We establish the energy structure of the ground configuration in Cd-like W and successfully identify seven of the forbidden transitions by using a combination of theory and experiment.

Contributions: I was driving the theoretical work and performing a majority of the calculations in all these publications together with and under supervision of T.B., with the exception of the supportive RMBPT calculations in A_V, which were performed by W.L. The idea of an separate core-valence model for the Ag-like systems was introduced by T.B. Paper A_{IV} is purely theoretical and fully drafted by me with input from T.B., and I took an active part in the authoring of the other papers, especially in writing the theoretical parts.

Paper A_{VII}: *Magnetic-dipole transitions in negative ions.*

[A_{VII}] **Resolving a discrepancy between experimental and theoretical lifetimes in atomic negative ions**
T. Brage and J. Grumer
arXiv:1606.08361 [physics.atom-ph] (submitted to J. Phys. B: At. Mol. Opt. Phys.)

Summary: We have recently seen breakthroughs when it comes to measuring long lifetimes of bound states in negative ions (Bäckström et al 2015 PRL 114, 143003). The development of the experimental method has, however, recently been hampered by an apparent discrepancy between experimental and theoretical lifetimes in the fairly simple atomic anion, S^-. Since it has been hard to

see why computations would fail for this case, the experimental technique has been cast into doubt. In this paper we remove this discrepancy through a systematic theoretical study for this and some other negative ions. This could in turn serve as a confirmation of the identification of transitions in these systems. The hope is that these results will serve to validate earlier efforts and support further development of trapping techniques to measure long-lived states in atomic systems.

Contributions: This paper was done in close collaboration with T.B. who conceived the idea of the project. I took part in the whole research process; ranging from performing calculations to taking an active part in writing the manuscript.

Paper B_I to B_{II}: *Hyperfine induced intensity redistributions of spectral lines, in general and for accurate abundance analyses in the Sun and other stars.*

[B_I] **Hyperfine induced intensity redistribution in In II**
J. Grumer, M. Andersson, and T. Brage
J. Phys. B: At. Mol. Opt. Phys. **43** 7 (2010)

[B_{II}] **Hyperfine-dependent gf-values of Mn I Lines in the 1.49-1.80 μm H Band**
M. Andersson, J. Grumer, N. Ryde, R. Blackwell-Whitehead, R. Hutton, Y. Zou, P. Jönsson, and T. Brage
Astrophys. J Suppl. Series, **216** 1 (2015)

Summary: This project started already back in 2009 during my master thesis project at Fudan University, Shanghai, at the EBIT Laboratory lead by R.H. and Y.Z. Both these papers concern *hyperfine-induced intensity redistributions in atomic spectra* - the spectral shifts in wavelength and intensities due to the symmetry-breaking perturbation from non-spherical electromagnetic interactions with the nucleus. Publication B_I concerns singly ionized indium (In II), which has a perfect atomic structure for investigations of hyperfine-induced effects. Available high-resolution spectra from Fourier transform spectroscopy, made this a very suitable model system. The

paper presents a detailed analysis of the hyperfine-dependent effects on the spectral distribution of radiation. In connection to this work we developed much of the theoretical framework and codes, which have formed a basis for the *the relativistic hyperfine-Zeeman code* (RHYZE) program - a general-purpose code to determine wavefunctions and radiative properties under the perturbation of symmetry-breaking effects (see Ch. 6 for details).

The developed method was then extended to the much more complex and, from an astrophysical perspective, relevant system of neutral manganese (Mn I), as presented in paper B_{II}. The abundance of manganese in e.g. the atmosphere of the Sun, has previously been overestimated by several orders of magnitude due to a too crude treatment of hyperfine-induced effects on the spectrum. In this paper we combine our method with stellar atmosphere simulations and compare with observed spectra to validate and demonstrate the importance of hyperfine-induced effects. We also present new hyperfine-dependent atomic data which should be of use in future analyses of stellar spectra.

Contributions: The work leading up to both these papers was done in close collaboration with M.A who acted as my supervisor together with T.B. for my master thesis project. For paper B_I I wrote the software and performed all simulations, under supervision of and based on M.A.'s previous codes. I prepared all figures and wrote the original draft of the manuscript, which then was finalized together with M.A., with input from T.B. This project was the starting point for the implementation of our method to treat the symmetry-breaking perturbations into the RHYZE program, which is written by me. For paper B_{II}, M.A. conceived the idea of the project together with R.B-W. The development of the necessary codes was done collaboratively by me and M.A based on the previous project on In II. M.A. added in particular routines for semi-empirical adjustments of certain atomic parameters. The atomic structure calculations and simulations were also done collaboratively, although mainly by M.A. The simulations of the stellar at-

mospheres were carried out by N.R. The manuscript was written collaboratively by M.A, me and N.R with input from T.B. I was driving the finalization of the paper as well as the submission procedure.

Paper B_{III} - B_V: *Unexpected radiative transitions induced by symmetry-breaking perturbations from hyperfine interaction or external magnetic-fields.*

[B_{III}] **Analysis of the competition between forbidden and hyperfine-induced transitions in Ne-like ions**
M. Andersson, J. Grumer, T. Brage, Y. Zou, and R. Hutton
Phys. Rev. A **93** 3 (2016)

[B_{IV}] **Theoretical investigation of magnetic-field-induced $2p^5 3s^3P_{0,2}$ - $2p^6\ ^1S_0$ transitions in Ne-like ions without nuclear spin**
J. Li, J. Grumer, W. Li, M. Andersson, T. Brage, R. Hutton, P. Jönsson, Y. Yang, and Y. Zou
Phys. Rev. A 88.1 (2013)

[B_V] **Effect of an external magnetic field on the determination of E1M1 two-photon decay rates in Be-like ions**
J. Grumer, W. Li, D. Bernhardt, J. Li, S. Schippers, T. Brage, P. Jönsson, R. Hutton, and Y. Zou
Phys. Rev. A **88** 2 (2013)

Summary: These publications concern *unexpected transitions* induced by hyperfine interactions and external magnetic fields. The energy structures and spectral information of Ne-like ions are of great interest in many applications. In paper B_{III} we compare *hyperfine-induced transitions* with forbidden transitions for Ne-like ions with non-zero nuclear spin at the neutral end of the isoelectronic sequence. Paper B_{IV} is similar to the first one, but concerns another class of *unexpected transitions* in Ne-like ions, namely *magnetic-field induced transitions* - transition appearing due to the perturbation of an external magnetic field. The results presented in this publication were recently confirmed experimentally (Beiersdorfer et al.

2016 ApJ 817, 67). The last work in this group, paper A_V, concerns storage-ring measurements of the $2s2p\,^3P_0 \rightarrow 2s^2\,^1S_0$ E1M1 two-photon decay in Be-like ions. The bending magnets of the ring give rise to an additional magnetic-field induced decay channel connecting these states which will impact the extraction of the two-photon rate. We present an elaborate model for the atomic structure and predict the rate of the induced transition of all ions in the isoelectronic sequence ranging from Be-like boron ($Z = 5$) to uranium ($Z = 92$). By comparing with existing theoretical models for the E1M1 rate, we show that the magnetic-field induced transition dominates or is of the same order for low- and mid-Z ions for a typical storage-ring field strength.

Contributions: The work resulting in paper B_{III} was initiated by M.A. and T.B. The calculations were mainly performed by M.A, and I took part in the development of the underlying theoretical method and in writing the software. M.A. wrote the majority of the draft of the paper and then left the field. Thereafter I lead the process of finalizing the paper in close collaboration with T.B. T.B and P. J. initiated the work presented in paper B_{IV}. The project was done in close collaboration with J.L., who was visiting us in Lund at the time. The design of the methods and calculations were performed collaboratively with J.L. with input from the other authors. J.L. carried out most of the relativistic *magnetic-field-induced transition* (MIT) calculations, I did the non-relativistic calculations and verified the results. Finally, paper B_V was done in collaboration with the experimental group of S.S at the heavy ion storage-ring at the Max-Planck-Institut für Kernphysik in Heidelberg. I was driving the entire process of this project - I initiated the contact with S.S, designed the theoretical model with support from P.J. and T.B., performed all calculations and wrote the draft of the manuscript and compiled all figures, with exception for the section concerning the storage-ring measurements, which was written by S.S.

Paper B_{VI}: *An overview of unexpected transitions.*

[B_{VI}] **Unexpected transitions induced by spin-dependent, hyperfine and external magnetic-field interactions**
J. Grumer, T. Brage, M. Andersson, J. Li, P. Jönsson, W. Li, Y. Yang, R. Hutton, and Y. Zou
Phys. Scr. **89** 11 (2014)

Summary: This proceeding outlines the concept of unexpected transitions due to symmetry-breaking spin-dependent, hyperfine and external magnetic-field interactions, in a general fashion.

Contributions: This publication was compiled in close collaboration with T.B. and M.A. The spin-dependent section was drafted by T.B., I wrote the section on magnetic-field induced effects and M.A. the section on hyperfine dependent properties. I produced most of the figures with the exception of the ones related to hyperfine-interaction and the angular distribution, which were done by M.A. and J.L., respectively.

Papers B_{VII} to B_{VIII}: *A novel method to probe magnetic fields in the solar corona to predict solar storms with applications in space-weather meteorology.*

[B_{VII}] **A novel method to determine magnetic fields in low-density plasma facilitated through accidental degeneracy of quantum states in Fe^{9+}**
W. Li, J. Grumer, Y. Yang, T. Brage, K. Yao, C. Chen, T. Watanabe, P. Jönsson, H. Lundstedt, R. Hutton, and Y. Zou
Astrophys. J. **807** 1 (2015)

[B_{VIII}] **Atomic-level pseudo-degeneracy of atomic levels giving transitions induced by magnetic fields, of importance for determining the field strengths in the solar corona**
W. Li, Y. Yang, B. Tu, J. Xiao, J. Grumer, T. Brage, T. Watanabe, R. Hutton and Y. Zou
Astrophys. J. **826** 2 (2016)

Summary: In this on-going project we suggest a novel method to measure magnetic-fields in low-density plasma, such as in the solar corona, via a *magnetic-field-induced transition* in Fe X. The measurement of the relatively weak magnetic fields in the solar corona remains one of the major challenges in solar physics, and is of importance to the prediction of solar events such as flares or coronal mass ejections, and ultimately space-weather forecasting. In Fe X we have found a unique system - it is abundant in the solar atmosphere and it has a rare quasi-degenerate energy structure of a few cm^{-1} which results in a strongly enhanced *magnetic-field-induced transition*. It is our belief that measurement of line intensity ratios involving this *magnetic-field-induced transition* could be used to determine the strength of coronal magnetic fields. The main method is presented, for the first time, in paper $\mathrm{B}_{\mathrm{VII}}$, while we in paper $\mathrm{B}_{\mathrm{VIII}}$ present an experimentally determined value for the quasi-degeneracy.

Contributions: This project is the result of an intense collaboration between the groups in Lund, lead by T.B., and in Shanghai, lead by R.H. My involvement in the project has been in the development of the theoretical methods to determine the magnetic-field sensitive *magnetic-field-induced transition* rate together with T.B. and P.J., and to implement the methods in a general-purpose software (Rhyze), under supervision of P.J. The majority of the atomic structure calculations and the evaluation of the *magnetic-field-induced transition* rates was done by W.L. who also performed the plasma modeling. I took part in the whole procedure leading up to paper $\mathrm{B}_{\mathrm{VII}}$, while for paper $\mathrm{B}_{\mathrm{VIII}}$, which is mostly experimental, my contribution was mostly through discussions and in preparing the paper for submission.

OTHER SCIENTIFIC CONTRIBUTIONS In addition to peer-reviewed articles appearing in scientific journals, the work included in this thesis has also been presented through a number of talks at scientific conferences and meetings, ranging from classic atomic physics and spectroscopy conferences, such as EGAS, ASOS and ICAMDATA, to astrophysics meetings such as HINODE - the annual international meeting for the solar satellite Hinode which is governed by the Japanese (JAXA/ISAS), United States (NASA), UK (STFC) and European (ESA) space agencies - as well as on a joint meeting between the Swedish Institute of Space Physics (IRF) and Swedish Civil Contingencies Agency (MSB) on space weather forecasting.

CONTENTS

Part I

INTRODUCTION

"*Space is the Place*"

— Sun Ra

1

BACKGROUND AND MOTIVATION

Natural science is a certain way of knowing about the world - it embodies the description, prediction, and understanding of natural phenomena, based on observational and empirical evidence [1]. The scientific method requires scientific advances to be validated through rigorous quality control mechanisms such as peer review and reproducibility of findings. Explanations which cannot be founded on empirical evidence, are not part of science. Einstein's *theory of relativity*, the *evolutionary theory*, first formulated by Darwin in 1859 in his book "On the Origin of Species", or *plate tectonics*, are examples of successful families of theories within physics, biology, and geology. More modern examples of scientific theories inhabit comparatively recent disciplines such as climate science, cognitive science, molecular biology or geographic information science (GIS).

Physics in particular, is concerned with the study of the most elementary constituents of the Universe and their motion through space and time. Via mathematical models it attempts to describe how these constituents interact with one and another through fundamental forces such as gravitation or the electromagnetic force, and the result of these interactions, ranging from the formation of galaxies to the prediction, and recent discovery, of the Higgs boson. This thesis concerns the fundamental structure and radiative properties of atoms and ions; how the atomic electrons interact with each other, with the nucleus, as well as with external magnetic fields, and ultimately how atomic systems interact with light for the purpose of analyzing laboratory and astrophysical spectra.

1.1 THE ATOM AND THE UNIVERSE

It is the current belief [2] that 4.6% of all matter in the Universe is directly visible. The remaining 95.4% is of an exotic nature which does not interact with photons, hence it is invisible to us and therefore referred to as cold dark matter and dark energy [3]. Around 99% of the visible part of the Universe is made up plasma; ionized clouds consisting of ions, free electrons and photons, continuously emitted and absorbed by the ions [3, 4]. Despite being the dominating phase of ordinary matter, plasma is something that many of us find strange and unfamiliar. It is indeed interesting to note that we live in an environment which almost exclusively belongs to the remaining 1% - being solids, liquids and ordinary gases.

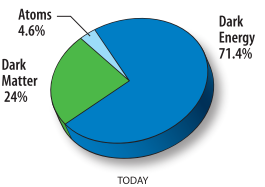

credit: NASA/WMAP [2]

Information about the very earliest stages in the evolution of the Universe, from the time before any stars or galaxies had formed, travels to us by blackbody background radiation. These and other photons are signatures of various astronomical phenomena and originate from radiaitve processes in nuclei, atoms and molecules. So, if we can understand how the photons were formed, how they are affected on their journey through intergalactic and interstellar space, and finally how to capture and record their characteristics, represented by spectral distributions, we can learn much about the Universe. Photons therefore play a crucial role to someone who would like to study the Universe, simply because they act as the *fundamental information carriers*[1] between a distant astronomical object, say a galaxy or a star, and an observer using a space-borne telescope or just you starring at the stars[2].

As an initial example of an actual spectrum, we show in Fig. 1.1 the

1 See also cosmic rays (high-energy atoms and protons) and the very recently discovered gravitational waves [5].

2 Disclaimer: make sure you wear protective eyewear when watching the Sun.

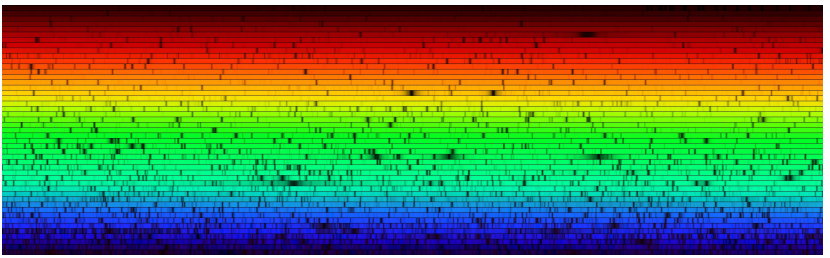

Figure 1.1: The solar spectrum generated from observations with the Fourier Transform Spectrometer at the McMath-Pierce Solar Facility at the National Solar Observatory on Kitt Peak, Arizona (cropped and rescaled, *credit: N.A.Sharp, NOAO/NSO/Kitt Peak FTS/AURA/NSF* [6]).

visible range of the solar spectrum, as recorded by the National Solar Observatory on Kitt Peak in Arizona. The Sun emits continuous blackbody radiation of all colors, so the dark patches seen in the specturm have to arise from absorption in the atmospheres of the Sun and the Earth. The wavelength and intensities of these darker regions contain fundamental information about the *abundance of elements* in the atmospheres, but one can also extract additional information such as *electron densities*, *temperatures* or *magnetic-field structures*.

An excellent example of how spectroscopy can be used to increase our knowledge about the Universe, is the discovery of helium - the second most abundant element in the Universe (24% of the total elemental mass), after hydrogen (75%). Despite its dominant abundance in the Universe as a whole, the first evidence of helium was not found on Earth, instead it was observed as a yellow line at 587.49 nanometers in the spectrum of the Sun's chromosphere during a solar eclipse on August 18, 1868 by the French astronomer J. Janssen in Guntur, India, and later the same year by the English astronomer N. Lockyer [7, p. 256]. It took another 14 years before the Italian physicist L. Palmieri found traces of helium on Earth by observation of the same yellow spectral line in an analysis of

the lava at Mount Vesuvius [8, p. 201]. Lockyer, together with the English chemist E. Frankland, named the element after the Greek word for the Sun (helios) [9].

We can visit the moon and bring home a piece of rock to a laboratory for analysis, or we can send spacecrafts to Mars and investigate its geology and habitability potential, but these are about the only examples where such direct studies are within reach. In the vast majority of cases we have to resort to analysis of light through *plasma spectroscopy*.

1.2 PLASMA SPECTROSCOPY

Plasma spectroscopy, being the study of emitted or absorbed electromagnetic radiation from an ionized media, manifests itself as one of the oldest and most fundamental tools in physics and astronomy. Quantitative analyses of the spectra from astronomical or earth-bound plasma sources require a detailed understanding of atomic structures as well as radiative and collisional processes. The spectral distribution of emitted or absorbed radiation is sensitive to variations in plasma parameters such as particle densities and temperatures, element type and their ionization stages, the magnitude and direction of external magnetic and electric fields, and more fundamentally on basic atomic properties such as transition wavelengths and oscillator strengths. The determination of such basic atomic parameters is however often far from trivial.

1.2.1 *The Fusion Energy Dream*

Much of the work in this thesis is motivated by the analysis and understanding of various plasmas, not only astrophysical ones. It has been a long-standing dream to bring the "fire" of the Sun down to Earth and harness its energy as a solution to the escalating energy

crisis. Fusion energy is produced by the melding of light nuclei into heavier ones - in the Sun hydrogen is fused to helium via the proton–proton chain reaction. Each such process yields energies of the order of MeV's, which could be compared to, say, the 13.6 eV gained by adding an electron to a hydrogen nucleus. Realizing this "fusion dream" is, however, a hard-won game due to the strong repulsion between the protons, which the Sun is overcoming with its massive gravitational pressure. On Earth we have to resort to speed. By accelerating the nuclei to high velocity, their electrostatic repulsion can be beaten and the nuclei have a chance to end up close enough for the attractive nuclear force to kick in and fusion to take place.

The Tokamak fusion plasma in the *International Thermonuclear Experimental Reactor* (ITER) [10, 11] (a *megaproject*[3] under construction in southern France), has to reach a temperature of at least 150 million °C for the fusion process to start - this is ten times the temperature at the core of the Sun [13]. The plasma is confined with strong dynamic magnetic fields in order to keep it stable at these extreme temperatures, which puts high demands on the plasma diagnostics. Fig. 1.2 shows the inside of the Tokamak vessel in *Joint European Torus* (JET), which has an equivalent setup to the one in ITER.

The plasma facing wall material of choice in the *divertor* of the ITER Tokamak, will be tungsten[4]. The divertor, which was first introduced in the 1950's, essentially functions as the exhaust system of the Tokamak. It allows for online removal of waste material, i.e. heavy contaminating ions sputtered form the vessel lining, under operation of the reactor. See the channel in the lower part of the JET Tokamak in Fig. 1.2.

An early attempt to make use of tungsten in a fusion vessel was

3 Extremely large-scale investment projects [12]. The current total cost of the ITER project is ~€13 billion.

4 The word tungsten comes from a combination of the two Swedish words for "heavy" and "stone".

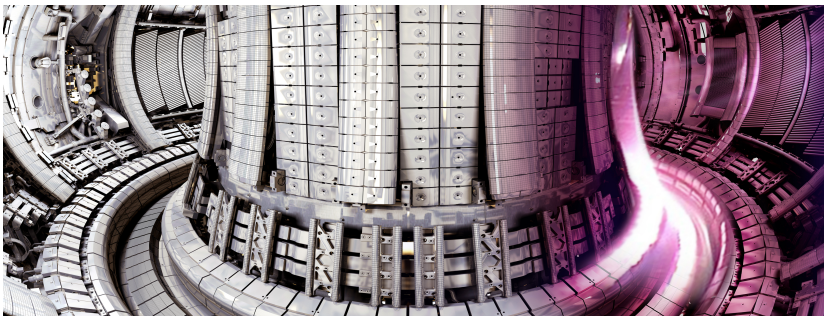

Figure 1.2: A picture of the JET Tokamak vessel superimposed with a section of plasma in pink (authentic color) [14]. (*credit: EUROfusion*).

in the *limiter* of the Princeton Large Torus in the late 1970's. The limiter, which was used extensively in the 1980's as a replacement of the divertor, was a small piece of material projecting into the outer edge of the main plasma confinement area so that ions escaping from the plasma would strike the limiter and thereby protecting the walls of the chamber from damage. It was however soon realized that the problems with contaminating material being deposited into the plasma remained; the introduction of the limiter had simply changed where the sputtering was taking place. The large radiation losses caused by the contaminating tungsten atoms/ions, still gave a significant degradation of the plasma performance [15], and the limiter was therefore abandoned. This lead to the re-introduction of the divertor now used in modern fusion devices.

Tungsten is the most heat-resistant material we know of, but atoms will nevertheless be sputtered and contaminate the fusion plasma. The main problem with tungsten is that it, as a heavy element, has ions with many electrons which generate a lot of radiation, in particular through intense X-ray emissions. Even a very small abundance of tungsten will cool the plasma substantially. The situation is similar to the plasma in a fluorescent tube, where a single

Mercury atom dominates the radiative output over 1000 Argon atoms [16]. The ratio of tungsten to hydrogen/helium in a tokamak plasma such as in ITER, should be even smaller - the radiative power of tungsten can be estimated to dominate at a ratio of around 1/10000 [17].

The existence of tungsten impurities in fusion plasmas seems to be a necessary evil. It is crucial to monitor the tungsten influx and transport to control and keep the fusion process stable, which is most conveniently done through spectroscopic studies of their emitted radiation. The tungsten charge state distribution provides a good estimation of the radiation loss from the plasma, but requires identification of spectroscopic lines with the correct element and ionization stage, and matched with an oscillator strength, which puts a high demand on accurate atomic data from theoretical and laboratory predictions. As an example, researchers recently determined the density of tungsten ions in high temperature deuterium plasmas at the JET facillity via X-ray spectroscopy, supported by atomic structure calculations for the spectrum analysis [18].

There is however a lack of atomic data for tungsten ions, see e.g. the NIST Atomic Spectra Database [19], much explained by their complex electron structure. Ions in the range between, say, W^{18+} to W^{24+} have either more than four 4f holes or electrons in the outer shell, leading to a large amount of levels even in their ground configurations. Studies of tungsten ions is therefore very difficult and before the idea that ITER would use tungsten as the plasma-facing divertor material, no real motivation to perform such investigations existed. The charge distribution models are therefore often inaccurate and lack important contributions from e.g. ionization from metastable states in the complex ground configurations [16], which is something we address in some of the work presented in this thesis.

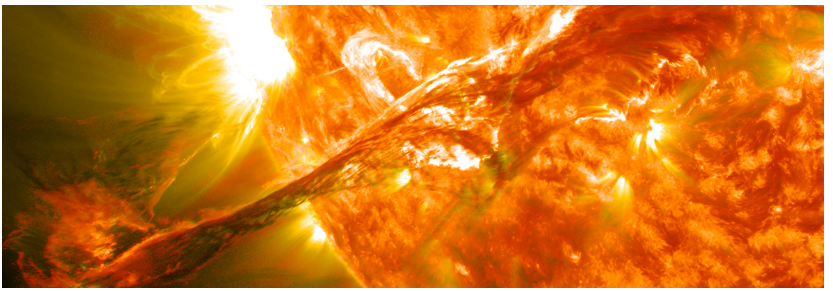

Figure 1.3: Picture taken by the *Solar Dynamics Observatory* (SDO) [20] on August 31, 2012 of a *coronal mass ejection* (CME) bursting out into space at more than 1500 km/s. The CME did not hit Earth directly, but connected with the magnetosphere and caused an Aurora on September 3 (*credit: NASA/GSFC/SDO*).

1.2.2 *Space Weather and the Solar Corona*

One of the most intriguing and mysterious plasma environments to date is probably the solar corona - the aura of hot plasma which makes up the outermost atmosphere of the Sun, reaching millions of kilometers into space. Its high temperature results in extreme plasma conditions in which unusually highly ionized ions are formed[5], which led to the suggestion in the end of the 19:th century that the corona contained a previously unknown element named "coronium". This was resolved by Edlén and Grotrian around 1940 by identification of the coronal lines as forbidden transitions from metastable levels in the ground configurations of highly ionized iron ions - the green Fe XIV line at 5303 Å and the red Fe X line at 6374 Å. The interested reader is referred to the George Darwin Lecture by Edlén [23] and the publications [24, 25] for further details on the discovery of the coronal lines. The discovery of the existence of these ions in the corona suggested surprisingly high temperatures at millions of °C, which is about a thousand times

5 See e.g. Slemzin et al. [21] and Del Zanna and Mason [22] for recent reviews of spectroscopic diagnostics of the corona.

higher than the temperatures at the solar surface. The formation of the extreme coronal temperatures remains to be understood and makes up an active area of research. It is the current belief that the high coronal temperatures are related to violent events such as solar flares or *coronal mass ejection*'s (CME's), formed by obscure magnetic field processes [26, 27].

The existence of magnetic fields in the solar atmosphere was first noticed by G. E. Hale in 1908 who saw the familiar splitting of spectral lines due to the Zeeman effect in solar spectra from sun spots [28]. These fields seem to play a fundamental role in the violent dynamics of the Sun's atmosphere, which ultimately governs the space weather surrounding Earth and all other planets in the solar system. Failure to predict coronal events such as flares or *coronal mass ejection*'s (CME's), could have a drastic impact on essentially all systems and technologies, in orbit, and on Earth. Flares sometimes produce strong x-rays which might block high-frequency radio waves used for communication, or solar energetic particles that could damage satellite electronics. CME's can give rise to geomagnetic storms in Earths' atmosphere, which not only cause the Aurora, but potentially also strong degrading currents in power grids with possible serious outcomes. This so-called *space weather* will have an impact on everything and everyone who depend on modern technology.

Determination of the relatively weak coronal magnetic fields remains one of the major challenges to solar physics. Knowledge about the fields is indeed crucial to our understanding of the dynamics in the corona, and ultimately for the prospect of conducting *space weather meteorology* in order to prepare ourselves for geomagnetic storms [29, 30]. Fig. 1.3 shows a picture of a CME escaping into space at high-speed from the solar corona, taken by the *Solar Dynamics Observatory* (SDO) at August 31 in 2012.

The origin of coronal eruptions such as the CME in Fig. 1.3 is thought to be related to conversion of magnetic to thermal energies through complex magnetic re-connection processes in the

coronal plasma [31], but the magnetic fields are too weak to be measured via traditional methods. One important result presented in this work is the development of a novel method to probe coronal magnetic-field strengths based on *magnetic-field-induced transition*'s (MIT's), a class of so-called *unexpected optical transitions* in atoms with intensities that are sensitive to the strength of the surrounding fields. The MIT of interest in the corona originates from Fe X (Fe^{9+}) and lies in the *extreme ultraviolet* (XUV) spectral region[6]. Fig. 1.4 shows an example XUV spectrum of the Solar corona recorded by the Hinode (Solar-B) mission[7], where the Fe X MIT belongs to the blended structure at 257.26 Å.

1.3 FURTHER ASPECTS OF THE STUDY OF ATOMS

Finally, we should not forget that the atom is interesting in itself, being a natural laboratory for theoretical and experimental physicists. The interactions amongst the atomic electrons and between the electrons and the nucleus are of electromagnetic nature, which can be described within the framework of *quantum electrodynamics* (QED) - arguably the most accurate physical theory to date[8]. The fact that the interactions of interest to predict the atomic structure are well-known, in contrast to, say, the interactions within the nucleus [33], makes the atom a perfect testing ground for many-body theory and correlation effects [34–36]. This remains a persistent motivation throughout the work featured in this thesis.

Other interesting fields within fundamental atomic physics, not touched upon in this work, involve time-dependent light-matter interaction studies on atto-second time scales [38, 39], the search for

6 The XUV spectral range spans the region from 1240 to 100Å.

7 The main science goals of the Hinode mission are to investigate the mechanisms responsible for heating the corona and to determine the mechanisms behind coronal events such as flares and CME's

8 The QED interaction parameter, the finestructure constant, $\alpha \approx 1/137$, is known to 0.2 parts in a billion [32]

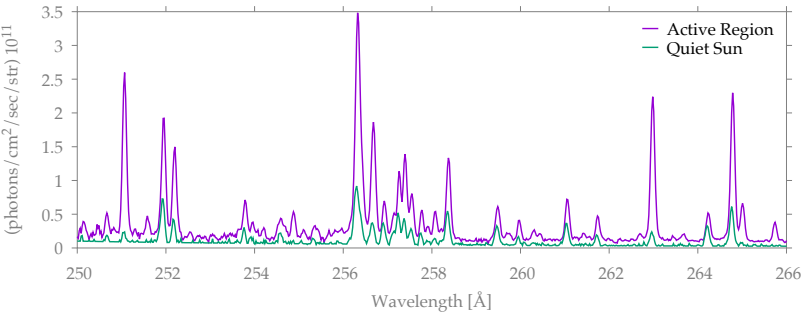

Figure 1.4: XUV spectrum of the solar corona as recored by the Hinode satellite [37]. The purple line correspond to observations of active regions (AR) (e.g. loop structures) and the green line to the quiet sun (QS) [21, 22].

parity-violating effects [40], space-time variations of fundamental constants, such as the fine-structure constant[9] [43, 44] and construction of the next generation of super-accurate atomic clocks [45] where a recent and, to this thesis, relevant development has been the incorporation of radiative effects induced by hyperfine interactions [46], and much more. See for example the comprehensive book "*Springer Handbook of Atomic, Molecular and Optical Physics*" [47] or numerous review articles such as the one by Mårtensson-Pendrill [48]).

All in all, understanding the fundamental function of atoms and their interactions with photons, and ultimately how they make up everything within us and around us, is key to building knowledge about the history of the Universe. I hope this work is a small step in that direction.

9 Recent observations of quasar absorption spectra point towards the existence of a spatial gradient in the value of α [41, 42].

1.4 THESIS OUTLINE

The remainder of this introduction, Part I, is focused on giving a comprehensible background to the concepts and theoretical framework used in the included papers. We begin in Ch. 2 with a basic, and relatively qualitative, review of atomic many-body theory as well as a motivation and introduction to the relativistic *multiconfiguration Dirac-Hartree-Fock* (MCDHF) approach, which is the many-body method of choice in this work. Ch. 3 summarizes the relativistic theory of radiative transition for a general many-electron system - i.e. the emission or absorption of photons. Ch. 4 gives a brief discussion about various many-body methods, their implementation into computer codes and, in particular, *the General-purpose Relativistic Atomic Structure Package* (GRASP2K) code. We then outline in Ch. 5 how to treat effects from additional perturbations to the atomic system from the atomic nucleus (hyperfine interaction) and from external magnetic-fields (Zeeman interaction) and the determination of radiative transition rates between the resulting perturbed eigenstates. After introducing the RHYZE code in Ch. 6, which has been developed to determine perturbed eigenstates in the general case as well as radiative transition rates of any multipole and radiative lifetimes, we evaluate the impact of such perturbations on the atomic spectrum. This subject is separated into two parts; Ch. 7 deals with *hyperfine-induced intensity redistributions* in spectra, and Ch. 8 with an exotic class of spectral features appearing due to the perturbations called *unexpected radiative transitions*. Both of these topics are central concepts in this work. Part I is then finished with a brief conclusion in Ch. 9.

Part II is devoted to the scientific articles included in this thesis[10]. See also the *Summary of Publications* in the thesis preamble for an overview of the articles.

10 Note that Part II has been removed from the electronic version of the thesis for copyright reasons. The reader is instead referred to the journals where the papers are published.

2

RELATIVISTIC ATOMIC THEORY AND METHODS

The past decades have seen a strong development of relativistic atomic structure theory. The general theory and methodology used in this work is outlined in a number of recent text books. To mention a few, Strange's book on relativistic quantum mechanics [49] and the book on atomic structure theory by Johnson [50], give an excellent introduction to the relativistic treatment of atoms. The book by Grant outlines in great detail realtivistic theory and modelling of atoms and molecules, and in particular the MCDHF method [36], which is central to this work. Lindgren's new book on relativistic many-body theory [51] uses a field-theretical approach, and can be regarded as a relativistic continuation of the well-known book by the same author and Morrison [34]. Finally, a recent review article by Fischer et al. on multiconfiguration methods [52] covers much of the theory and methodology applied in this work.

In the following we will draw inspiration from these sources and just briefly introduce the subject of relativistic multiconfiguration many-electron theory, motivate approximations and the choice of method, and refer to the literature for further details.

2.1 INTRODUCTION TO THE ATOMIC MANY-BODY PROBLEM

Theoretical physics plays the role of predicting different measurable physical quantities - observables - which in combination with experiments, in the form of laboratory measurements or astronomical observations, allow us to build better physical models and increase our understanding of the world around us.

The basic task for most quantum theorists is, in one way or another, connected to solving partial differential equations - the Schrödinger equation for non-relativistic theories, or the Dirac equation in a relativistic framework. In a stationary-state regime with a Hamiltonian operator, H, corresponding to the total kinetic and potential energy of the system under consideration, such an equation can be represented by the well-known eigenvalue problem,

$$(H - E_\alpha)\,\Psi_\alpha = 0 \tag{2.1}$$

which is solved to obtain stationary wavefunctions, Ψ_α, with energy spectrum, E_α. The label α is such that it provides enough information to distinguish at-least non-degenerate states. Once the wavefunctions have been obtained, it is possible to determine other physical observables such as radiative transition rates or isotope shifts. The wavefunction representing a many-body system, such as an atom with more than one electron, is however an extremely complex entity and as such the determination of physical quantities ends up being a true challenge to theory.

For an atom consisting of N electrons, each individual electron has three spatial, $\mathbf{r}$, and one spin, σ, degree of freedom. The total wavefunction thus becomes a $4 \times N$ multidimensional function,

$$\Psi_\alpha(\mathbf{q}_1, \mathbf{q}_2, \ldots, \mathbf{q}_N) \tag{2.2}$$

where $\mathbf{q}_i = (\mathbf{r}_i, \sigma_i)$. Exact solutions to (2.1) can not be found for $N > 1$ and one has to resort to some approximate scheme. Douglas R. Hartree expressively argued for the need of approximate solutions:

> *"One way of representing a solution quantitatively would be by a table of its numerical values, but an example will illustrate that such a table would be far too large ever to evaluate, or to use if it were evaluated. Consider, for example, the tabulation of a solution [of (2.1)] for one stationary state of Fe [$Z = 26$] . Tabulation has to be at discrete values of the variables, and 10 values of each variable would provide only*

> *a very coarse tabulation; but even this would require* 10^{78} *[*$10^{3\times Z}$*] entries to cover the whole field; and even though this might be reduced to, say,* $5^{78} \approx 10^{53}$ *by use of the symmetry properties of the solution, the whole solar system does not contain enough matter to print such a table. And, even if it could be printed, such a table would be far too bulky to use. And all this is for a single stage of ionization of a single atom.*"
>
> — Douglas R. Hartree [53]

In brief, most theoretical models start off in an independent-particle approach - an approximation in which it is assumed that the individual one-particle properties are of dominant nature and the many-body contributions come in as smaller perturbations. This allows for a separate treatment of each particle which then can be combined into a many-body description of the complete system through methods of varying complexity and advantages, based on e.g. variational methods, such as *Hartree-Fock* (HF), *configuration interaction* (CI) and *multiconfiguration self-consistent field* (MCSCF), perturbative approaches such as *Møller-Plesset many-body perturbation theory* (MP-MBPT), as well as the well-known *coupled cluster* (CC), *density functional theory* (DFT) and *quantum monte-carlo* (QMC) methods.

In the present work we exclusively utilize a combination of the relativistic MCDHF method, to obtain one-electron wavefunctions, and *relativistic configuration interaction* (RCI) to include further electron correlation effects as well as contributions from the Breit interaction and one-loop QED corrections in the form of the electron self-energy and vacuum-polarization. But, before introducing this method in some more detail, the situation may be simplified further by making use of the symmetry properties inherent in the wavefunction.

2.2 THE WAVEFUNCTION AND THE ROLE OF SYMMETRY

A certain symmetry of a physical system can be related to a physical quantity which is preserved or remains unchanged under some transformation. Identifying and learning how to take advantage of these symmetries is essential when dealing with the quantum mechanical many-body problem.

A first fundamental symmetry observation is that any *isolated system*[1] in a quantum state $|\alpha\rangle$ must be completely invariant under continuous *coordinate rotations* in three-dimensional space, simply due to the presumed isotropy of space. Similarly, the state of a isolated system remains unaltered under *coordinate inversion*[2]. These two observations implies that quantum states of e.g. free nuclei, atoms or molecules can be labeled by a definite total angular momentum, J, its projection, M, and by parity, π, such that

$$|\alpha\rangle \rightarrow |\gamma J^{\pi} M\rangle \quad . \tag{2.3}$$

where γ is an additional label introduced to uniquely identify the states. The rotational invariance of isolated systems further implies that there is a $(2J+1)$-fold degeneracy among the states which only differ in their projection quantum number, M, which therefore is suppressed in the following. If, however, the system is perturbed by an external field of definite direction in three-dimensional space, the rotational symmetry will be broken and the M-degeneracy lifted. We will return to this in Ch. 5 when discussing effects introduced by the influence of an external magnetic field.

The quantum theory of angular momentum of many-body systems is embodied in what is called *Racah* (or Racah-Wigner) algebra [54–56]. With group-theoretical roots, Racah algebra introduces *irreducible spherical tensor operators* as central building blocks. This

1 An isolated system is really isolated in the sense that it does not exchange any matter or energy with its surroundings.

2 Ignoring the weak interaction which is not invariant under parity transformation.

lead to the derivation of fundamental relations such as the *Wigner-Eckart theorem*, which factors out fundamental symmetry information of a matrix element. In brief, Racah algebra provides, in a most elegant fashion, calculational and notational simplifications which have proven decisive for the evaluation of matrix elements between complex many-electron configurations. It should be emphasized that Racah algebra only deals with the angular part of the wavefunction - the evaluation of the radial integral is straightforward once the radial functions have been obtained. With these tools at hand, one can then readily deal with questions such as,

- How to form a totally anti-symmetric many-electron basis from one-electron functions?
- How to ensure that this basis also conserves parity and angular momentum?
- How to construct irreducible tensor operators that applies to this basis?
- How to evaluate matrix elements for such operators between these basis states efficiently?
- How to transform eigenstates from one coupling scheme to another, e.g. jj $\rightarrow$ LSJ?

There are a number of books covering the subject of angular momentum theory and Racah algebra for general many-electron systems. To select two, the well-known book on non-relativistic atomic structure theory by Cowan [57] is very useful, in particular since it connects the sometimes quite abstract angular momentum algebra to the actual atomic many-electron problem in a clear self-contained package. And, when in need, never doubt the exhaustive compilation of angular momentum expressions and tensor algebra by Varshalovich et al. [58].

2.3 HARTREE ATOMIC UNITS

Before we begin discussing relativistic effects and many-body methods, we introduce the *Hartree atomic units*, which will prove especially convenient to atomic structure theory.

In Hartree's system of natural units the numerical value of four fundamental constants are set to unity; the electron mass, m, the electron charge, e, the reduced Planck's constant, $\hbar$, and the Coulomb's constant $k_e = 1/(4\pi\epsilon_0)$. These definitions will then clear many of the mathematical expressions appearing in atomic theory of unnecessary constants, but they might also cause confusion when left out, so we will sometimes include them nevertheless.

The atomic unit of energy is the *Hartree*, E_h, which is equal to two Rydbergs[3], $E_h = \hbar c\alpha/a_0 = 2Ry \approx 27.2$ eV, where $\alpha \approx 1/137$ is the (unitless) fine-structure constant, and the Bohr radius $a_0 \approx 0.52$ Å, is the atomic unit of length. Mass is measured in units of the electron mass, $m \approx 9.1 \times 10^{-31}$ kg, and charge in the electron's charge, $e \approx 1.6 \times 10^{-19}$ C. In addition, the atomic unit of time is $\hbar/E_h \approx 24 \times 10^{-18}$ s and the unit of velocity is then $a_0 E_h/\hbar = c\alpha \approx c/137 \approx 2.2 \times 10^6$ m/s.

2.4 MOTIVATION TO A RELATIVISTIC TREATMENT

Relativistic effects clearly become more and more apparant the faster particles move - with fundamental implications such as mass increase and time dilation. It was long thought that a relativistic treatment of the relatively slow-moving ($v \ll c$) valence electrons, which determine most physical and chemical properties, was unimportant. Even Dirac himself argued that relativistic effects would be negligible in atomic physics and chemistry in the

3 Rydberg used a slightly different value for the electron mass and charge in his definition of atomic units.

opening paragraph of his most cited paper from 1929[4]:

> *"This general theory of quantum mechanics is now almost complete, the imperfections that still remain being in connection with the exact fitting of the theory with relativity ideas. These give rise to difficulties only when high-speed particles are involved, and are therefore of no importance in the consideration of atomic and molecular structure and ordinary chemical reactions, in which it is, indeed, usually sufficiently accurate if one neglects relativity variation of mass with velocity and assumes only Coulomb forces between the various electrons and atomic nuclei. The underlying physical laws necessary for the mathematical theory of a large part of physics and the whole of chemistry are thus completely known, and the difficulty is only that the exact application of these laws leads to equations much too complicated to be soluble. It therefore becomes desirable that approximate practical methods of applying quantum mechanics should be developed, which can lead to an explanation of the main features of complex atomic systems without too much complications."*
>
> — P. A. M. Dirac [60]

Today, despite Dirac's prediction, many of us rely on the theory of special and general relativity almost every day through technical innovations, such as the GPS system which. Accurate prediction of geographical location, necessary for e.g. self-navigating robots or precise clock-synchronization, depend heavily on relativistic corrections. This is of course hard to relate to since they are hidden in the software in e.g. the technical apparatus on-board satellites - but there is a much more hands-on example, and that is the yellow shimmering color of solid gold.

The lure of gold has been the downfall of many - from alchemists persistent endeavor to achieve transmutation, to gold diggers filled with false hope during the 19th century gold rush. But, as we will

4 See also the analyze of Dirac's famous paper by Kutzelnigg [59].

see, if it was not for relativistic effects, gold would actually be boringly grey-ish like the majority of the other metals.

The "*Albert Einstein World Award of Science*" gold medal. Note its relativistic yellow gleam! (*credit: the World Cultural Council [61]*).

The importance of relativistic effects in atomic physics, chemistry and solid state physics in general, and of gold in particular, has recently been highlighted by Gorin and Toste [62] and reviewed in numerous articles, especially by Pyykkö [63–66] (who also recently suggested a new relativistic periodic table up to $Z = 172$ based on *Dirac-Hartree-Fock* (DHF) calculations [67]), but also by Schwerdtfeger [68] and Autschbach [69] and many others.

In the following we will try to motivate our usage of a relativistic quantum mechanics in two steps; first by a simple argument in which we combine the Bohr's simplistic atomic model with the special theory of relativity, and then by comparing radial electron densities and energies from non-relativistic HF with those from relativistic DHF calculations. We then relate the findings to the band-structure and reflectivity of solid gold in a qualitative manner.

2.4.1 *The Relativistic Bohr Model*

One of the most basic consequences of special relativity is that the mass of a particle increases towards infinity as its velocity, v, approaches the speed of light c. Mathematically the relativistic mass is expressed as

$$m_r = m \Big/ \sqrt{1 - (v/c)^2}\,, \tag{2.4}$$

where m is the mass of the particle at rest ($m = 1$ a.u. for an electron). In a simplistic Bohr picture of a hydrogenic one-electron atom, the average velocity, energy, and orbital radius of an atomic electron, are given by

$$\langle v \rangle = Z \Big/ n, \quad \langle r \rangle = Z \Big/ \left[m_r \langle v \rangle^2 \right], \quad \langle E \rangle = -m_r Z^2 \Big/ \left[2n^2 \right] \tag{2.5}$$

in atomic units, where n is the principal quantum number, and m_r is the relativistic electron mass (2.4).

The gold atom has a nuclear charge of $Z = 79$ and its atomic ground-state has the electron configuration

$$1s^2\,2s^2\,2p^6 \ldots 5s^2\,5p^6\,5d^{10}\,6s\,,$$

in standard spectroscopic notation $(nl)^w$, where l is the orbital angular momentum quantum number and w the subshell occupation. Its 1s-electrons, which are closest to the nucleus and subject to strong electrostatic interaction from all 79 protons (ignoring the small shielding from the other 1s electron), have, according to (2.5) a speed of 58% of c ($v/c = 79/137$ in a.u.). Using this in (2.4) gives a substantial 22% mass increase, which implies a decrease of the Bohr radius from $1/79 \approx 0.013$ a.u. to $1/(1.22 \times 79) \approx 0.010$ a.u., that is about -18%. This relativistic radial contraction, which applies to, at least, all s and p^- ($p_{j=1/2}$) orbitals, then results in greater ionization energies of these electrons. We will return to this shortly, for now we just note that the linear dependence on the electron mass in the total energy as predicted by the relativistic Bohr model (2.5) implies a -22% decrease in the total energy of the 1s electron - that is, an increased binding energy.

2.4.2 *Direct and Indirect Relativistic Effects*

Being an inner-shell electron, the 1s electron in heavy elements is obviously strongly relativistic. But how does relativity affect the much more physically and chemically active outer electrons, such as the 5d and 6s electrons in gold? To answer this we perform a non-relativistic HF calculation and compare the results with those from a relativistic DHF calculation.

Starting with the radial expectation value, we get for the 6s orbital that

$$\langle r\rangle^{6s}_{\mathrm{HF}} = 3.70 \text{ a.u.} \quad \rightarrow \quad \langle r\rangle^{6s}_{\mathrm{DHF}} = 3.06 \text{ a.u.}$$

from which it is clear that the 6s orbital undergoes a relativistic contraction of -17%. This so-called *direct relativistic effect* affects all s and p^- electrons since they all have a non-negligible density in the vicinity of the nucleus. The contraction can clearly be seen if we plot the radial electron densities of 6s from HF and DHF wavefunctions, see Fig. 2.1a.

For the 5d orbital on the other hand, where both the relativistic orbtials are considered, we get

$$\langle r\rangle_{\mathrm{HF}}^{5\mathrm{d}} = 1.54 \text{ a.u.} \quad \rightarrow \quad \langle r\rangle_{\mathrm{DHF}}^{5\mathrm{d}^+} = 1.62 \text{ a.u.}, \quad \langle r\rangle_{\mathrm{DHF}}^{5\mathrm{d}^-} = 1.54 \text{ a.u.}$$

So for 5d the effect is apparently smaller, but interestingly enough we see, not a relativistic contraction as in the 6s-case but instead, a radial expansion. This is the result of a, so-called, *indirect relativistic effect* caused by the increased screening of the nucleus by the relativistically contracted s and p^- electrons. This effect can be seen for many electrons with high angular momentum, which are radially located relatively far out from the nucleus. Just like for 6s, a comparison between the non-relativistic and relativistic radial densities for $5d^+$ shows a small expansion in its radial distribution, see Fig. 2.1b.

As an example of an observable relativistic effect, consider the ionization energy of neutral gold. In a relatively simple model one can predict the ionization energy from the difference between the ground-state energy of singly ionized gold, Au^+, with that of neutral gold and compare the non-relativistic and the relativistic results. The ground state of Au^+ has the configuration $5d^{10}$ and neutral gold an additional 6s electron. From the HF model the non-relativistic ionization energy becomes 5.92 eV, while the relativistic DHF calculation, including the Breit interaction and leading order QED effects, results in 7.65 eV - that is an increase of 29% towards the experimental value at 9.22 eV [70], mainly explained by the relativistic contraction of the 6s electron. Adding contributions from electron correlation makes the relativistic result converge towards and reach the experimental value, which is not the case for the non-relativistic model.

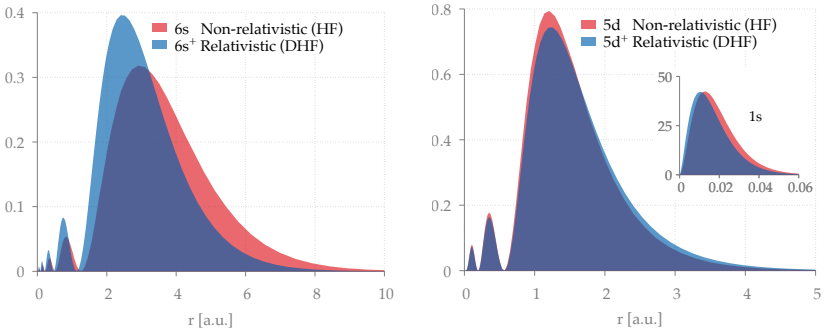

(a) Direct effect: contraction of 6s

(b) Indirect effect: expansion of 5d

Figure 2.1: Comparison between non-relativistic and relativistic radial densities of 6s and 5d electrons from HF and DHF calculations. The contraction of 1s is shown in the (b) inset plot (-12% in this model), which, together with the other s and p^- orbitals, results in the radial expansion of 5d and other high-l orbitals. Note that only $5d^+$ is included since the relativistic effect on $5d^-$ is negligible in this case.

2.4.3 *The Relativistic Yellow Color of Gold*

But what about the original question - what actually makes solid gold "golden"? The answer is hidden in the band-gap between the top of the filled 5d-band and the Fermi level in the half-filled 6s-band. For a single gold atom we know that the absorption of the blue light in gold is due to a radiative transition in which a 5d electron is excited to a 6s electron, or more accurately the magnetic dipole transition $5d^{10}6s \rightarrow 5d^{9}6s^{2}$. The critical parameter here is then the energy difference between these two configurations which is related to binding energy of the 5d and 6s electrons which in turn depends on their radial density distribution, as was shown in Fig. 2.1. Since the 5d-electrons are slightly moved upward in the energy spectrum by the indirect relativistic shift induced by the increased screening from the inner electrons, whereas the 6s-

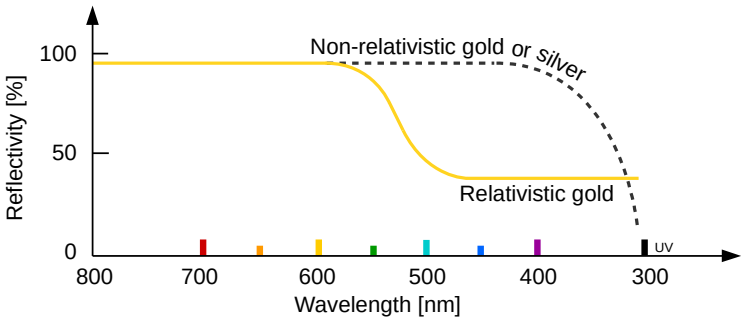

Figure 2.2: Schematic spectral reflectance curves for relativistic (solid yellow line) versus non-relativistic (dashed grey line) gold in solid form. The non-relativistic curve has a behaviour much similar to the true curve for silver. The relativistic wavelength shift corresponds to a shift in energy of about 1.5 eV [66] and is responsible to why gold is golden and not silvery.

electrons become tighter bound by the direct relativistic radial contraction - the band-gap becomes smaller.

In a non-relativistic model, the energy separation between the 5d and 6s bands lies in the UV region which then is shifted towards the middle of the visible energy-range by the relativistic effects. Thereby it will absorb all blue wavelengths while all yellow and red wavelengths are reflected. Fig. 2.2 shows a schematic plot of the relativistic and non-relativistic reflectivity, illustrating the impact of this relativistic shift on the perceived color of gold in solid form. Non-relativistic gold is therefore white, just like silver and the majority of the other metals, and the yellow color of gold is indeed a product of relativity.

2.5 THE ATOMIC MANY-BODY HAMILTONIAN

The atom is ultimately a mash-up of charged particles and photons, and as such it can be described by a combination of QED

and many-body physics - two parts with a seemingly complicated relationship. The "best" fully relativistic covariant Hamiltonian we know of is the Bethe-Salpeter equation, first introduced for bound-state problems in 1951 by Salpeter and Bethe [71, 72] and by Gell-Mann and Low [73]. This equation does, in principle, predict all kinds of electron correlation and QED effects.

The Bethe-Salpeter equation is however extremely hard to solve for a number of reasons, essentially due to its theoretical formulation in relation to how one normally treats many-body systems in quantum mechanics. One major problem is that the equation is based on field theory and therefore lacks a direct connection to the conventional Hamiltonian approach of relativistic quantum mechanics. Another intricacy is that its solutions, which are on four-component form, involve individual time variables for two particles - one for the particle and another for its anti-particle, which becomes even more complicated in the many-particle regime when each particle has its own local time. This is very different from the normal quantum-mechanical picture in which there is a single time variable for the total system. There are nevertheless recent attempts to construct a joint many-body-QED theory by extending the Bethe-Salpeter equation to the multireference case resulting in the so-called Bethe-Salpeter-Bloch equation. However, as interesting as this subject may be (see the recent book by Lindgren for details [51]) it falls outside the scope (and required accuracy for our purposes) of this thesis.

A good working basis for a quantitative relativistic many-body treatment has proven to be the *Dirac-Coulomb-Breit* (DCB) Hamiltonian, where the fully relativistic electron-electron interaction is replaced by the regular Coulomb interaction, $1/r_{ij}$, and corrected for by leading QED terms by the *retarded Breit interaction* [51] which includes the transverse magnetic interaction as well as retardation effects due to the finite speed of the exchanged virtual photons.

Consider a general Hamiltonian for a fixed number of electrons, N, in a central nuclear potential, $V_{nuc}(r)$, resulting from an extended

nuclear charge distribution[5]. It is convenient to express the many-body Hamiltonian in terms of a sum over one h_i and two-particle h_{ij} operators,

$$H = \sum_i^N h_i + \sum_{i<j}^N h_{ij} \,. \tag{2.6}$$

The *one-particle* term is usually taken as the Dirac Hamiltonian,

$$h_i^D = c\boldsymbol{\alpha}_i \cdot \mathbf{p}_i + \beta_i c^2 + V_{nuc}(r_i), \quad \mathbf{p} = -\imath\boldsymbol{\nabla}\,, \tag{2.7}$$

where $\boldsymbol{\alpha}_i$ and β_i are the Dirac matrices for particle i. The Dirac-α is a three component vector of matrices with components

$$\alpha_s = \begin{pmatrix} \mathbf{0}_2 & \sigma_s \\ \sigma_s & \mathbf{0}_2 \end{pmatrix}, \qquad s = x,\, y,\, z \tag{2.8}$$

where $\mathbf{0}_2$ is a (2×2) zero-matrix, and σ_s the Pauli matrices,

$$\sigma_x = \begin{pmatrix} 0 & 1 \\ 1 & 0 \end{pmatrix}, \; \sigma_y = \begin{pmatrix} 0 & -\imath \\ \imath & 0 \end{pmatrix}, \; \sigma_z = \begin{pmatrix} 1 & 0 \\ 0 & -1 \end{pmatrix}. \tag{2.9}$$

The Dirac-β matrix is a diagonal matrix defined as

$$\beta = \begin{pmatrix} \mathbf{1}_2 & \mathbf{0}_2 \\ \mathbf{0}_2 & -\mathbf{1}_2 \end{pmatrix}, \text{ where } \mathbf{1}_2 = \begin{pmatrix} 1 & 0 \\ 0 & 1 \end{pmatrix}. \tag{2.10}$$

The *two-particle* Hamiltonian can as a first approximation be represented by the instantaneous electron-electron Coulomb interaction

$$h_{ij}^C = 1/r_{ij} = 1/|\mathbf{r}_i - \mathbf{r}_j|\,, \tag{2.11}$$

which together with the single-particle Dirac operator h^D, gives the extensively used *Dirac-Coulomb* (DC) Hamiltonian,

$$H^{DC} = \sum_i^N h_i^D + \sum_{i<j}^N h_{ij}^C \,. \tag{2.12}$$

5 It is important for heavy nuclei to replace the point-like representation and use an actual extended representation of the nuclear charge, such as the Fermi distribution.

2.5.1 *The Coulomb Cusp Condition*

Note that the Coulomb interaction is singular for $\mathbf{r}_i = \mathbf{r}_j$ such that the DC Hamiltonian diverges to infinity whenever two electrons coincide, i.e. each electron is surrounded by a classically forbidden region known as the *Coulomb hole*.

As a simplified illustration, inspired by Knowles et al. [74], consider a non-relativistic model of the He-like two-electron system for which highly accurate wavefunctions are easily constructed. The non-relativistic two-electron Hamiltonian can for a point-like nucleus of infinite mass be written,

$$H = \sum_{i=1}^{2} \left(-\frac{1}{2}\nabla_i^2 - \frac{Z}{r_i} \right) + \frac{1}{r_{12}}, \tag{2.13}$$

in Cartesian coordinates with the origin at the nucleus, with singularites in the inter-electronic repulsion term at $r_{12} = 0$ and in the two attractive nuclear terms at $r_i = |\mathbf{r}_i| = 0$. For the left-hand side of the Schrödinger equation $H\psi = E\psi$ to remain finite at these points, the "infinities" must be canceled by equal "infinities" of opposite sign. This is equivalent to that the *local energy*,

$$\epsilon(\mathbf{r}_1, \mathbf{r}_2) = \frac{H\psi(\mathbf{r}_1, \mathbf{r}_2)}{\psi(\mathbf{r}_1, \mathbf{r}_2)}, \tag{2.14}$$

remains constant and equal to the eigenenergy, E, at all points in space. Since the electrons are not always close to the nucleus, the only remaining terms that can accomplish this cancellation are the kinetic operators $-\nabla_1^2/2 - \nabla_2^2/2$. The Schrödinger equation then implies that if these operators are to produce such infinite local energies, the wavefunction must be *non-differentiable* at the coalescence points.

To analyze the effects the singularities have on the wavefunction

we follow Knowles et al. and transform to center-of-mass and relative coordinates,

$$\mathbf{R} = \frac{1}{2}(\mathbf{r}_1 + \mathbf{r}_2)\,, \qquad \mathbf{r} = \mathbf{r}_2 - \mathbf{r}_1 \tag{2.15}$$

which gives the Hamiltonian,

$$H = -\frac{1}{4}\nabla^2_{\mathbf{R}} - \frac{2}{r_1} - \frac{2}{r_2} - \nabla^2_{\mathbf{r}} + \frac{1}{r} \tag{2.16}$$

The ground-state of He-like systems ($1s^2\,{}^1S$) is spherically symmetric, such that one can approximate the wavefunction by simple expansion in r around $r = 0$ at a given distance from the nucleus, say $r_1 = r_2$ a.u.,

$$\psi = a_0 + a_1 r + a_2 r^2 + \dots \tag{2.17}$$

Insertion in the Schrödinger equation gives [74, Eq. 17],

$$0 = \frac{1}{r}\,(a_0 - 2a_1) + (a_1 - 6a_2 - 4/R - E) + r(\dots \tag{2.18}$$

In order for the energy expression to be finite across $r = 0$, then the terms that multiply $1/r$ must cancel, such that $a_0 = 2a_1$, or,

$$\left.\frac{\partial\psi}{\partial r}\right|_{r=0} = \frac{1}{2}\psi\Big|_{r=0}\,, \tag{2.19}$$

a result known as the *inter-electronic Coulomb cusp condition*. This implies that the wavefunction has a linear dependence on r as the electrons move away from eachother in any direction, implying a characteristic discontinuous first derivative in the wavefunction for spatially coinciding electrons. The inter-electronic cusp in the He-like ground-state wavefunction is visualized in Fig. 2.3 for fixed electron radii $|\mathbf{r}_1| = |\mathbf{r}_2|$ as a function of the relative angle θ between $\mathbf{r}_1$ and $\mathbf{r}_2$.

The Hamiltonian (2.16) also provides an analogous *nuclear cusp condition*, representing the coalescence of the electrons with a point-like nucleus,

$$\left.\frac{\partial\psi}{\partial r_i}\right|_{r_i=0} = -Z\psi(r_i = 0)\,, \tag{2.20}$$

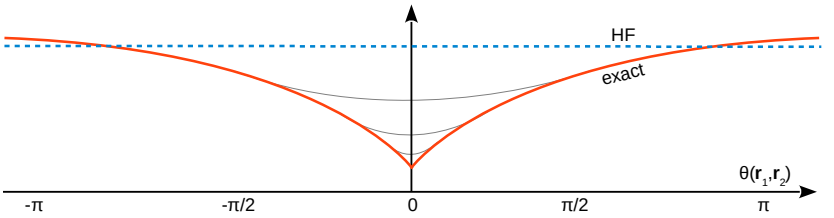

Figure 2.3: Schematic representation of the spherically symmetric He-like ^1S ground-state wavefunction (solid thick red line) plotted at fixed radii $|\mathbf{r}_1| = |\mathbf{r}_2|$ as a function of the relative angle θ between $\mathbf{r}_1$ and $\mathbf{r}_2$. The exact wavefunction is compared to a mean-field HF solution which completely fails to account for the cusp behavior at $r_{12} = 0 \Leftrightarrow \theta = 0$, but may be improved by a successively enlarged CI wavefunction (thin solid gray lines).

so that the singularities at the nucleus are balanced by kinetic terms proportional to $1/r_i$.

While the singularity at $r_i = 0$ due to the nuclear cusp can be treated exactly, the description of the non-smooth behavior in the the wavefunction at $r_{ij} = 0$ poses a major obstacle to computational models, and is the main underlying reason for the slow convergence of CI wavefunctions with respect to the size of the many-body basis set expansion.

The problem can be circumvent via *explicitly correlated wavefunctions* in which the Hamiltonian is expressed in terms of interelectronic distances r_{ij}, such as the *Hylleraas method* [75]. Such methods are however only feasible for systems containing up to a few electrons in general, due to the rapidly increasing number of interelectronic coordinates.

2.5.2 *The Breit Interaction*

The Coulomb interaction corresponds to the first order term in the QED description of the interaction between two charged particles via exchange of virtual photons. The next-in-line relativistic corrections are given by the *retarded Breit interaction*, which adds to the electrostatic Coulomb interaction contributions from magnetic interactions as well as retardation effects due to the finite speed of the exchanged virtual photons. This subject is indeed quite involved, but the interested reader can find a relatively simple introduction in the book by Strange [49, Ch. 10.1] before moving on to the more rigorous derivations in e.g. the book by Grant [36] or Lindgren [51].

The retarded Breit Hamiltonian (real part) can be written as [36, Eq. (4.9.21)],

$$h_{ij}^{B}(\omega) = -\frac{(\boldsymbol{\alpha}_i \cdot \boldsymbol{\alpha}_j)\cos(\omega_{ij} r_{ij}/c)}{r_{ij}} + (\boldsymbol{\alpha}_i \cdot \boldsymbol{\nabla}_i)(\boldsymbol{\alpha}_j \cdot \boldsymbol{\nabla}_j)\frac{\cos(\omega_{ij} r_{ij}/c) - 1}{\omega_{ij}^2 r_{ij}/c^2} \tag{2.21}$$

in which $\omega_{ij} c = |\epsilon_i - \epsilon_j|$ is the difference between the one-particle energies representing the energy of the exchanged virtual photon between electron i and j. The gradient operator $\boldsymbol{\nabla}_i$ acts on the spatial coordinates of electron i in the expressions $\mathbf{r}_{ij} = \mathbf{r}_i - \mathbf{r}_j$ and $r_{ij} = |\mathbf{r}_{ij}|$.

By taking the long-wavelength limit $\omega_{ij} \to 0$ one retains Breit's original frequency-independent form [76] known as the *instantaneous Breit interaction* [36, Eq. (4.9.22)],

$$h_{ij}^{B}(0) = -\frac{1}{2r_{ij}}\left\{\boldsymbol{\alpha}_i \cdot \boldsymbol{\alpha}_j + \frac{(\boldsymbol{\alpha}_i \cdot \mathbf{r}_{ij})(\boldsymbol{\alpha}_j \cdot \mathbf{r}_{ij})}{r_{ij}}\right\} \tag{2.22}$$

which neglects effects to α^4 and higher orders, but is sufficient in most cases since the corrections from the frequency-dependent

part generally is very small. This is the commonly adopted form of the Breit correction in the present work.

Adding the Breit-interaction, given by one of the forms above, to the Coulomb interaction, gives

$$h_{ij}^{CB} = h_{ij}^{C} + h_{ij}^{B}(\omega)\,, \tag{2.23}$$

which together with the one-particle contributions in (2.6) is known as the DCB Hamiltonian.

We finally would like to point out that the well-known quasi-relativistic Breit-Pauli Hamiltonian, which is used to improve non-relativistic one-component models, can be obtained from the DCB Hamiltonian by decoupling of the positive and negative energy solutions via a so-called Foldy-Wouthuysen transformation [36]. This reveals quasi-relativistic one-electron terms like the spin-orbit interaction and two-electron terms such as the orbit-orbit or spin-other-orbit interactions.

2.5.3 *Some Important Remarks*

The DC and DCB Hamiltonians have proven to work well in atomic structure calculations, but in using these one should be aware of two things:

1. First of all, these Hamiltonians do not satisfy basic relativistic invariance requirements, that is, invariance under Lorentz transformations, in contrast to the initially discussed fully invariant Bethe-Salpeter equation. It is often claimed that calculations based on these Hamiltonians are "fully" relativistic, but this is only true up to first order in α in the DC case, or α^2 in the case of the DCB Hamiltonian with the instantaneous Breit interaction.

2. These operators suffer from another rather severe shortcoming in that they are not bound from below - nothing prevents

the electrons from "falling into the Dirac sea", take negative energy solutions and thereby becoming positrons. Positive energy solutions can therefore mix with and obtain contributions from negative solutions, which then has to be projected out. This obscure phenomena came to be known as the *The Brown-Ravenhall disease* [77]. In *relativistic many-body perturbation theory* (RMBPT) the solution is to introduce projection operators in the DCB Hamiltonian which is known as the No-Virtual Pair Approximation (NVPA) [78]. See Heully et al. [79] for a discussion on the importance of including negative-energy states.

However, in *self-consistent field* (SCF) calculations of DHF type, such as the method adopted in the present work, one can generally leave out the projection operators since the adopted boundary conditions and resitriction on the one-electron solutions effectively excludes the negative energy solutions [36].

2.5.4 *Radiative QED corrections*

Interactions between an isolated atomic system with the *QED vacuum field* should at least be treated up to the same order in α as the Breit interaction. The dominant *radiative* QED contributions, of order α^2, are the one-loop *electron self-energy* and *vacuum polarization* corrections.

The *electron self-energy* corresponds to the interaction of the atomic electrons with their own radiation field. There is however no generalized expression, or operator for that matter, of the self-energy for an N-electron atom, so one has to resort to values from hydrogenic calculations. The total contribution from the self-energy can then be obtained by summing up such one-electron contributions [80], in the simplest picture scaled by a screened nuclear charge, and weighted by the generalized occupation number in the many-electron wavefunction.

The *vacuum polarization* is the additional screening introduced by the electron-positron pair-production in the field of the nucleus. The situation is similar to the self-energy in that there is no actual many-electron operator which can be included in the total Hamiltonian. The vacuum polarization is instead usually accounted for by correcting the nuclear Coulomb potential, using e.g. the Uehling (second-order) and the Källén-Sabry (fourth-order) potentials [81]).

It should be noted that Shabaev et al. [82] very recently suggested a non-local QED operator, which they also made publicly available last year via the *Computer Physics Communications International Program Library* (CPC-IPL) [83] as a general Fortran routine: QEDMOD [84]. This should allow for a straightforward inclusion of radiative one-loop corrections in general many-body eigenvalue problems based on the DCB Hamiltonian.

2.5.5 *Nuclear Motional Corrections*

It is implicit in the above formalism that the nuclear mass is infinite. There are however cases when one must include the effect of a finite nuclear mass on the atomic energy levels, i.e. corrections to the atomic structure due to the motion (recoil) of the nucleus.

The lowest order *nuclear motional effects* are usually separated into the *normal* and *specific mass shift*, which can be written as general operators and included in relativstic many-body calculations [85]. Higher order corrections have been derived independently by Shabaev [86, 87] and Palmer [88], leading to the so-called *recoil operator*. In addition to the nuclear motional corrections, there is also the *field shift* arising from the change in nuclear charge distributions between different isotopes. Information about the charge distribution of a certain isotope can be extracted from observations of the field shifts in combination with a theoretical model for the atom and for the nucleus, as demonstrated by e.g. Papoulia et al. [89].

These effects have however not been investigated in this thesis, and are just briefly mentioned here for the completeness of the present general discussion on atomic structure.

2.6 REDUCTION TO RADIAL EQUATIONS

It is conventional in atomic structure theory to attack the general many-electron problem by assuming that all electrons move *independently* of each other in an average field due to the nucleus, $V_{\text{nuc}}(r)$, and the other electrons, $u(\mathbf{r})$. For now we assume the average electron potential to be common to all electrons in difference from e.g. HF where it is non-local. This is the well-known *independent-particle model*. The situation is simplified further by applying the *central-field model* in which it is assumed that the average electron field is central, $u(\mathbf{r}) \to u(r)$, so that each individual electron moves in a total *central* average potential due to the nucleus the other electrons,

$$V_{\text{av}}(r) = V_{\text{nuc}}(r) + u(r)\,.$$

By adopting these approximations we may modify the one-electron Hamiltonian (2.7) according to,

$$h_i^{\text{D}} = c\boldsymbol{\alpha}_i \cdot \mathbf{p}_i + \beta_i c^2 + V_{\text{av}}(r_i)\,. \tag{2.24}$$

This allows for the following separation of the DC Hamiltonian, (2.12),

$$H^{\text{DC}} = H_0 + H_1\,; \quad \begin{cases} H_0 = \sum_i^N h_i^{\text{D}} \\ H_1 = \sum_{i<j}^N \frac{1}{r_{ij}} - \sum_i^N V_{\text{av}}(r_i) \end{cases}\,. \tag{2.25}$$

Now, assume that a set of orbitals $\{\phi_{a_i}(\mathbf{q}_i)\}$, where a_i is a quantum label and $q_i = (\mathbf{r}_i, \sigma_i)$ as usual, satisfy the single-particle Dirac equation, based on the modified Dirac operator (2.24),

$$h_i^{\text{D}}\phi_{a_i}(\mathbf{q}_i) = \epsilon_{a_i}\ \phi_{a_i}(\mathbf{q}_i) \tag{2.26}$$

with eigenvalues $\{\epsilon_{a_i}\}$. These approximations imply that the N-electron eigenfunction of H_0 can be written as a product of such orbitals (which remains to be anti-symmetrized),

$$\phi_{a_1}(\mathbf{q}_1)\,\phi_{a_2}(\mathbf{q}_2)\,\ldots\,\phi_{a_N}(\mathbf{q}_N) \tag{2.27}$$

with a total eigenenergy given by the sum of the corresponding one-particle energies,

$$E^{(0)}_{a_1 a_2 \cdots a_N} = \epsilon_{a_1} + \epsilon_{a_2} + \ldots + \epsilon_{a_N}\,. \tag{2.28}$$

Futhermore, the central-field formulation of the average potential results in a separation of the radial, angular and spin coordinates such that one can write the above orbitals as products of radial and a spin-angular functions.

The spin-angular functions, called *spherical spinors*, $\Omega_{jlm}(\theta,\phi)$, are formed from products of *spherical harmonics*, Y_{lm_l}, which are eigenfunctions of the orbital angular momentum operators $\mathbf{l}^2$ and l_z, and *spinors*, χ_μ, which are eigenfunctions of the spin operators $\mathbf{s}^2$ and s_z. These functions are defined as two-component vectors with two possible values $j = l \pm 1/2$,

$$\Omega_{l+1/2,l,m}(\theta,\phi) = \begin{pmatrix} \sqrt{\frac{l+m+1/2}{2l+1}}\,Y_{lm-1/2}(\theta,\phi) \\ \sqrt{\frac{l-m+1/2}{2l+1}}\,Y_{lm+1/2}(\theta,\phi) \end{pmatrix} \tag{2.29}$$

$$\Omega_{l-1/2,l,m}(\theta,\phi) = \begin{pmatrix} -\sqrt{\frac{l-m+1/2}{2l+1}}\,Y_{lm-1/2}(\theta,\phi) \\ \sqrt{\frac{l+m+1/2}{2l+1}}\,Y_{lm+1/2}(\theta,\phi) \end{pmatrix} \tag{2.30}$$

for spin up and down states respectively. The spherical spinors are eigenfunctions of $\boldsymbol{\sigma}\cdot\mathbf{l}$, and therefore also of the operator,

$$\mathcal{K} \equiv -1 - \boldsymbol{\sigma}\cdot\mathbf{l}\,, \tag{2.31}$$

where $\boldsymbol{\sigma}$ is the vector of Pauli matrices (2.9), so that

$$K\Omega_{jlm}(\theta,\phi) = \kappa\Omega_{jlm}(\theta,\phi) \tag{2.32}$$

with eigenvalues $\kappa = \mp(j + 1/2)$ for $j = l \pm 1/2$. The κ quantum number therefore *collectively* denotes both the orbital l and total angular momentum j. This allows for the more compact, yet unique, notation $\Omega_{jlm}(\theta, \phi) \equiv \Omega_{\kappa m}(\theta, \phi)$. The spherical spinors are orthonormal in κ and m,

$$\int_0^{\pi} \sin\theta \int_0^{2\pi} \Omega^{\dagger}_{\kappa' m'}(\theta, \phi)\Omega_{\kappa m}(\theta, \phi)\, d\theta d\phi = \delta_{\kappa\kappa'}\delta_{mm'} \quad (2.33)$$

and since the spherical harmonics are eigenfunctions of the parity operator, P, with eigenvalues, $\pi = (-1)^l$, so are also the spherical spinors; $P\Omega_{\kappa m} = (-1)^l\Omega_{\kappa m}$. Note that the $\pm\kappa$-spinors differ by one unit of orbital angular momentum, and are therefore of opposite parity.

Total one-electron eigenfunctions to the central-field Dirac equation (2.26) can then be defined by combining spherical spinors with radial functions to form 4-component vectors called *Dirac-orbitals*,

$$\phi_{n\kappa m}(\mathbf{q}) = \frac{1}{r}\begin{pmatrix} P_{n\kappa}(r)\Omega_{\kappa m}(\theta, \phi) \\ \iota Q_{n\kappa}(r)\Omega_{-\kappa m}(\theta, \phi) \end{pmatrix} \quad (2.34)$$

where $\mathbf{q} = \{\mathbf{r}, \sigma\}$ and ι is the imaginary unit. The non-degenerate $|n\kappa\rangle \Leftrightarrow |njl\rangle$ eigenstates are usually labeled by the *spectroscopic notation*,

$$1s_{1/2},\ 2p_{1/2},\ 2p_{3/2},\ 3s_{1/2},\ 3p_{1/2},\ 3p_{3/2},\ 3d_{3/2},\ 3d_{5/2} \ldots,$$

where n is the principle radial quantum number (which together with l gives the node-structure of the radial functions), the letters correspond to orbital angular momentum (or azimuthal) quantum numbers

$$s,\ p,\ d,\ f,\ g,\ h \ldots \quad \Leftrightarrow \quad l = 0,\ 1,\ 2,\ 3,\ 4,\ 5 \ldots,$$

and the subscript denotes the total angular momentum quantum number, j.

The separation into radial and spin-angular functions has the important implication that the spin and angular dependent parts can

be treated analytically, using the earlier mentioned angular momentum framework, and what remains is the determination of the radial functions, $P_{n\kappa}(r)$ and $Q_{n\kappa}(r)$. Insertion of the Dirac-orbitals (2.34) into (2.26) leads to the coupled first-order differential equations,

$$\begin{aligned}\left(V_{av}+c^2\right)P_{n\kappa}+c\left(\frac{d}{dr}-\frac{\kappa}{r}\right)Q_{n\kappa}&=\epsilon_{n\kappa}P_{n\kappa}\\ -c\left(\frac{d}{dr}+\frac{\kappa}{r}\right)P_{n\kappa}+\left(V_{av}-c^2\right)Q_{n\kappa}&=\epsilon_{n\kappa}Q_{n\kappa}\end{aligned}\tag{2.35}$$

which are to be solved for each electron, in the common average potential, V_{av}, under the orthonormality condition,

$$\int\left[P_{n\kappa}(r)P_{n'\kappa}(r)+Q_{n\kappa}(r)Q_{n'\kappa}(r)\right]dr=\delta_{nn'}\,.\tag{2.36}$$

2.6.1 *Example: the Central Coulomb Field*

It is instructive to consider the special case when the average field is taken as a simple Coulomb potential, $V_{av}=-Z/r$, for which it is possible to solve this system of equations exactly[6]. The resulting spectrum of eigenenergies is given by,

$$\begin{aligned}E_{n\kappa}&=mc^2\Bigg/\sqrt{1+\frac{\alpha^2Z^2}{(\gamma+n-k)^2}}\\&=mc^2\left[1-\frac{\alpha^2Z^2}{2n^2}-\frac{\alpha^4Z^4}{2n^3}\left(\frac{1}{k}-\frac{3}{4n}\right)+\mathcal{O}\left(\alpha^6Z^6\right)\right]\end{aligned}\tag{2.37}$$

where the electron mass $m=1$ in the atomic units used here, $\gamma^2=\kappa^2-\alpha^2Z^2$ where the positive square root is chosen to ensure particle solutions, $k=|\kappa|$ and the expansion is in powers of αZ. The first term in the expansion over αZ is simply the rest energy of the electron, the second the non-relativistic energy in a

6 See e.g. Ch. 2.7 in the book by W. Johnson [50].

Coulomb-field. The third term is the leading fine-structure correction which lifts the degeneracy between e.g. $2p_{1/2}$ and $2p_{3/2}$ in hydrogen. Note that this expression has to be shifted by $-mc^2$ to fit with the corresponding non-relativistic energies.

Fine-structure splittings such as in 2p is predicted well by the Dirac equation, but the fact that the energy depends on $|\kappa|$, and not κ, implies a degeneracy between $\pm\kappa$-states of equal n (and thus also j). The most famous example of such a degeneracy is probably the one between the $2s_{1/2}$ and $2p_{1/2}$ states in hydrogen. Their energy separation is predicted to be zero by the Dirac equation, while its experimental value actually is ≈ 0.0354 cm^{-1}. This discrepancy is the well-known *Lamb shift*, which spurred major progress in theoretical physics in general and QED in particular, leading to the development of the radiative QED corrections, such as the self-energy and vacuum polarization discussed in Sec. 2.5.4.

The importance of the discovery and evaluation of the Lamb shift is hard underestimate. In Dirac's own words:

> "*No progress was made for 20 years. Then a development came, initiated by Lamb's discovery and explanation of the Lamb shift, which fundamentally changed the character of theoretical physics.*"
>
> — P. A. M. Dirac [90, p. 27]

The complete analytic form of the Dirac-Coulomb wavefunctions can be found in text books such as Johnson's [50, Eq. (2.151-152)], but as an example, consider the $1s_{1/2}$ ($n = 1$ $\kappa = -1$) ground-state in hydrogenic systems,

$$P_{1\,-1}(r) = \sqrt{\frac{1+\gamma}{2}}\sqrt{\frac{2Z}{\Gamma(2\gamma+1)}}\,(2Zr)^{\gamma}e^{-Zr} \tag{2.38}$$

$$Q_{1\,-1}(r) = \sqrt{\frac{1-\gamma}{2}}\sqrt{\frac{2Z}{\Gamma(2\gamma+1)}}\,(2Zr)^{\gamma}e^{-Zr} \tag{2.39}$$

where Γ is the gamma function. Notice that the ratio between the two functions is $\approx 2/\alpha Z \approx 2 \times 137/Z$ so that $Q_{n\kappa}(r)$ is several orders of magnitude smaller than $P_{n\kappa}(r)$ for low-Z. $P_{n\kappa}(r)$ and $Q_{n\kappa}(r)$ are therefore referred to as the *large* and *small* components of the Dirac wavefunction respectively.

It can be shown that the number of nodes in the large component, $P_{n\kappa}(r)$, is given by $(n-l-1)$, just as in the familiar non-relativistic case. The small component, $Q_{n\kappa}(r)$, has $(n-l-1)$ nodes for $\kappa < 0$, but one more, $(n-l)$, for $\kappa > 0$. The node structure is indispensable to the implementation of SCF methods such as HF, essentially to ensure that the physical states of interest have been found.

Finally, it should be clarified that the energy spectrum $E > mc^2$ given above is just one half of the actual energy spectrum predicted by the Dirac-equation. As was mentioned earlier in relation to the *Brown-Ravenhall disease* in section 2.5.3, it also has a corresponding set of negative solutions, $E < -mc^2$, referred to as Dirac's "*negative energy sea*". These solutions represent anti-particles, manifested in the wavefunction through a sign-change in γ, which in turn results in a swapped relation in magnitude between the large and small radial components.

In order to prevent particles from falling into the negative energy sea in an attempt to minimize their energy, Dirac famously argued that these energy states actually are filled, and that regular particles correspond to excitations in this field, leaving holes representing anti-particles. This line of argument has (arguably) mostly been confusing to the atomic structure community, while electron holes is an important concept in e.g. solid state physics, where for example both negatively charged electrons and positively charged holes can carry current in doped semi-conductors, or compound particle-hole states represent localized quasi-particles called *excitons*.

2.7 THE MANY-BODY BASIS

Before turning to the MCDHF method, we introduce the *configuration state function* (CSF) many-electron basis and argue for the advantages of using angular-momentum coupled basis states of definite total angular momentum.

2.7.1 *Coupled vs. Uncoupled Basis Sets*

The simplest form of an anti-symmetric N-body product wavefunction (2.27) which also obeys the Pauli exclusion principle, is arguably the $N \times N$ *Slater determinant* (SD),

$$\begin{aligned}\psi_N^{SD}(\mathbf{q}_1\mathbf{q}_2\ldots\mathbf{q}_N;\, a_1 a_2 \ldots a_N) \\ \equiv \frac{1}{\sqrt{N!}} \begin{vmatrix} \phi_{a_1}(\mathbf{q}_1) & \phi_{a_1}(\mathbf{q}_2) & \ldots & \phi_{a_1}(\mathbf{q}_N) \\ \phi_{a_2}(\mathbf{q}_1) & \phi_{a_2}(\mathbf{q}_2) & \ldots & \phi_{a_2}(\mathbf{q}_N) \\ \ldots & \ldots & \ldots & \ldots \\ \phi_{a_N}(\mathbf{q}_1) & \phi_{a_N}(\mathbf{q}_2) & \ldots & \phi_{a_N}(\mathbf{q}_N) \end{vmatrix}\end{aligned} \tag{2.40}$$

where $\phi_{a_i}(\mathbf{q}_i)$ is a Dirac orbital (2.34) for the i:th electron, and $a_i \Leftrightarrow n_i\kappa_i m_i \Leftrightarrow n_i l_i j_i m_i$. Once the radial orbitals are determined, using e.g. the simplistic Coulombic mean-field model discussed above, the determinental functions are completely known and matrix elements can be evaluated using the *Slater-Condon rules* [91, 92], or the extended *Löwdin-rules* to treat non-orthogonal orbitals [93].

As an example, consider the uncoupled determinental wavefunction of a two-electron system (here represented by a single generic angular momentum, j, for simplicity). This function is then constructed from the product of two $|j_i m_i\rangle$ states that are eigenfunc-

tions of the angular momentum operators $\mathbf{j}_i^2$ and j_{iz} with eigenvalues $j_i(j_i+1)\hbar^2$ and $m_i\hbar$,

$$\psi_2^{SD}(\mathbf{q}_1\mathbf{q}_2; j_1m_1j_2m_2) \tag{2.41}$$
$$= \frac{1}{\sqrt{2}}\Big[\phi_{j_1m_1}(\mathbf{q}_1)\phi_{j_2m_2}(\mathbf{q}_2) - \phi_{j_1m_1}(\mathbf{q}_2)\phi_{j_2m_2}(\mathbf{q}_1)\Big].$$

There are however important advantages of instead using *coupled basis functions*, which, by construction, are eigenfunctions of the total angular momentum, $\mathbf{J}^2$, its projection, J_z, and parity, π, operators - and thus labeled by the *total* quantum numbers (JM). As a simple introduction, consider again the two-electron example above. A corresponding coupled set of states then can be formed according to the vector-coupling expansion over the uncoupled $j_1j_2m_1m_2$-states corresponding to SD's,

$$\big|j_1j_2JM\big\rangle = \sum_{m_1,m_2} \big\langle j_1j_2m_1m_2\big|j_1j_2JM\big\rangle\big|j_1j_2m_1m_2\big\rangle \tag{2.42}$$

where the sums over m_1 and m_2 runs over all possible projections of the associated j's, the overlaps $\big\langle j_1j_2m_1m_2\big|j_1j_2JM\big\rangle$ are *Clebsh-Gordan coefficients* and the coupled states are eigenfunctions of the $\mathbf{j}_1^2$, $\mathbf{j}_2^2$, $\mathbf{J}^2 = (\mathbf{j}_1+\mathbf{j}_2)^2$ and $J_z = j_{1z}+j_{2z}$ operators.

A coupled representation has a number of important advantages, ranging from improved computational properties to physical interpretability:

1. *divide-and-conquer* - a coupled basis directly breaks the interaction matrices into blocks of different J, which then can be treated separately. This should speed up computations substantially.

2. *labeling* - the fact that the coupled functions are eigenfunctions to the total angular momentum operators makes it immediately apparent which J that is associated with a certain eigenstate, of e.g. the DCB Hamiltonian. This is advantageous when comparing with experiments through databases such as the NIST Atomic Spectra Database [19].

3. *coupling scheme* - choosing the coupling scheme which best represents the coupling conditions of the configuration under investigation (e.g. jj- or LSJ-coupling) should give relatively pure eigenvectors and it becomes possible to assign, in addition to J, further quantum numbers to the eigenstate (e.g. the LS-term, $^{2S+1}$L) .

4. *basis transformation* - it is also possible to transform between different coupling representation via transformation matrices. This is useful to provide insight about e.g. the above mentioned coupling conditions, or simply because a certain community is more familiar with a, say, LSJ- than jj-labeling of the energy levels and radiative transitions.

5. *evaluation of matrix elements* - the coupled basis functions can of course be expressed in terms of the uncoupled functions, and the coupled matrix elements could therefore be evaluated as linear combinations of matrix elements between individual SD's - cf. (2.42). The above listed advantages would then be counter-balanced by the increased level of complexity introduced in the determination of this linear combination. This is luckily not the case due to the sophisticated mathematical techniques of Racah [54–56] which allows for a *direct evaluation* of matrix elements in the coupled representation.

6. *qualitative estimates* - coupled functions provide qualitative estimates of physical observables, such as transition rates.

The abundant amount of symmetry information built into a coupled basis, makes it possible to directly analyze what type of basis states that are of importance when calculating energies or other observables. The book on non-relativistic computational atomic structure by C. F. Fischer et. al. [35] contains many good general guidelines.

2.7.2 *The Configuration State Function*

For the reasons discussed in the previous section, we introduce a coupled basis in the form of *configuration state function*'s (CSF's) corresponding to a general N-electron configuration consisting of q subshells of equivalent electrons,

$$(n_1\kappa_1)^{w_1}\,(n_2\kappa_2)^{w_2}\ldots(n_q\kappa_q)^{w_q},\ \sum_k^q w_k = N \tag{2.43}$$

where w_k is the occupation number of the k:th subshell. The CSF's are explicitly anti-symmetrized products of Dirac orbitals, coupled to total angular momentum via standard angular momentum coupling techniques, in a similar fashion to the two-electron case (2.42).

The construction is however non-trivial in general due the anti-symmetry requirement, and is done using a recursive procedure for one subshell of equivalent electrons at a time. An antisymmetric function for a subshell k of w_k electrons is built from a linear combination of antisymmetrized $(w_k - 1)$-electron functions called parent states, coupled to a one-electron $n\kappa$-state while preserving antisymmetry. The $(w_k - 1)$ function is in turn determined in exactly the same way; from a linear expansion of $(w_k - 2)$ parent functions coupled to a one-electron state. This iterative scheme continues until there are no electrons left in the subshell.

The expansion coefficients in these expansions are determined via the method of *coefficients of fractional parentage*[7]. These coefficients are such that terms corresponding to unwanted symmetric product states cancels in the total linear expansion, which results in a fully anti-symmetric function for each of the individual subshells. The coupled product of all these forms a *partially* anti-symmetric

7 The method of coefficients of fractional parentage is indeed quite complex at a first glance. The author finds the example of $p^2 + p$ in Cowan's book [57, Ch. 9.5] illustrative.

N-electron function that is anti-symmetric only with respect to coordinate permutations *within* each subshell,

$$\psi^{\wp}(\gamma J^{\pi} M) \equiv \prod_{k}^{q} \left(Q_k \middle| (n_k \kappa_k)^{w_k} \tilde{\alpha}_k \tilde{\nu}_k J_k M_k \right\rangle \tag{2.44}$$

where Q_k denotes the set of electron coordinates $\{\mathbf{q}_i\}_k$ belonging to the k:th subshell, $\tilde{\nu}_k$ is the seniority number introduced by Racah [55, 56] to distinguish between subshells $(nk)^w$ (or $(nlj)^w$) up to g^w, under some restrictions [52]. The supplementary label $\tilde{\alpha}_k$ is necessary for subshells with $j \geqslant 9/2$. This is the so-called *seniority* representation of $\psi^{\wp}$; note that there is an equivalent *quasi-spin* representation with advantages for the treatment of the spin-angular part in complex systems, but which we leave out in the present discussion (see e.g. [36] and references therein for details).

The additional anti-symmetrization required between the subshells, is obtained via an explicit coordinate permutation scheme applied to coordinates belonging to electrons of *different* subshells ($Q_k \leftrightarrow Q_{k'}; k \neq k'$) under the restriction that the ordering of the coordinates within each subshell is in increasing order to avoid double counting[8]. Finally we define the CSF as the normalized and *totally antisymmetrized* N-electron function,

$$\psi^{\text{CSF}}_{\alpha} \equiv \left(\mathbf{q}_1 \mathbf{q}_2 \ldots \mathbf{q}_N \middle| \gamma J^{\pi} M \right\rangle = \sqrt{\frac{\prod_k w_k!}{N!}} \sum_{\mathcal{P}} (-1)^p \psi^{\wp}_{\mathcal{P}\alpha} \tag{2.45}$$

where $\alpha = \gamma J^{\pi} M$ is a collective label as in (2.3), the square-root pre-factor is a normalization constant corresponding to the number of unwanted permutations within each subshell, p is the parity of permutation $\mathcal{P}$, and γ denotes the electron configuration, intermediate coupling information (in jj-coupling, e.g. J_{12}, J_{123} etc.), as well as additional quantum numbers necessary to uniquely specify the state. The total parity of the CSF is given by

$$\pi = (-1)^{\sum_i^N l_i} = (-1)^{\sum_k^q w_k l_k}, \tag{2.46}$$

8 In the non-relativistic case, see e.g. Cowan [57, Ch. 9.8], as well as the articles by Fano [94] and Robb [95] for details.

which is directly determined from the electron configuration (2.43).

2.7.3 *Matrix Elements in CSF Representation*

The general expression for the CSF is indeed quite involved. The evaluation of matrix elements of symmetric operators may however be simplified greatly by taking advantage of the symmetry properties built into the CSF basis. We limit the present discussion to CSF's belonging to the *same electron configuration* and note that it is straightforward to adopt the same line of arguments for the general case [57, Ch. 13.9].

We begin by noting that the anti-symmetry of the CSF's implies that the corresponding matrix elements of general one- and two-electron operators f_i and g_{ij} are independent of the indexes i and j, such that,

$$\left\langle \psi_\alpha^{\mathrm{CSF}} \right| \sum_i^N f_i \left| \psi_{\alpha'}^{\mathrm{CSF}} \right\rangle = N \left\langle \psi_\alpha^{\mathrm{CSF}} \right| f_N \left| \psi_{\alpha'}^{\mathrm{CSF}} \right\rangle \tag{2.47}$$

$$\left\langle \psi_\alpha^{\mathrm{CSF}} \right| \sum_{i<j}^N g_{ij} \left| \psi_{\alpha'}^{\mathrm{CSF}} \right\rangle = \frac{N(N-1)}{2} \left\langle \psi_\alpha^{\mathrm{CSF}} \right| g_{N-1,N} \left| \psi_{\alpha'}^{\mathrm{CSF}} \right\rangle \tag{2.48}$$

where the operators f_N and $g_{N-1,N}$ act only on the variables $\mathbf{q}_N$ or $\mathbf{q}_{N-1}$, $\mathbf{q}_N$ by convention.

In addition, starting with the *one-particle matrix elements* (2.47), it can be shown that all permutations $\mathcal{P}$ in (2.45) results in the same numerical value for the matrix element. It is therefore enough to consider elements between the much simpler partially antisymmetric functions of basic unpermuted ordering, $\psi^{\wp}$, given by (2.44). The matrix elements (2.47) thus reduce to a sum over groups of

equivalent electrons belonging to different subshells k of occupation w_k [57, Ch. 9.9],

$$\left\langle \psi_\alpha^{\mathrm{CSF}} \middle| \sum_i^N f_i \middle| \psi_{\alpha'}^{\mathrm{CSF}} \right\rangle = \sum_k^q w_k \left\langle \psi_\alpha^{\wp} \middle| f_{(k)} \middle| \psi_{\alpha'}^{\wp} \right\rangle \tag{2.49}$$

where $f_{(k)}$ operates on the last electron coordinate of the k:th subshell.

The *two-particle matrix elements* (2.48) can be simplified in a similar manner, with the additional consideration of the fact that permutations of electron coordinates in the functions $\psi_{\mathcal{P}\alpha}^{\wp}$ can result in non-vanishing interactions either *within* (1), or *between* (2) subshells:

1. The permutations are equal, $\mathcal{P} = \mathcal{P}'$, and such that the coordinates $N-1$ and N of occur in the *same subshell*, $(n_k \kappa_k)^{w_k}$,

2. The permutations are such that the coordinates occur in different subshells, $(n_k \kappa_k)^{w_k}$ and $(n_{k'} \kappa_{k'})^{w_{k'}}$, and:

   a) they are exactly equal ($\mathcal{P} = \mathcal{P}'$) such that the coordinates $\mathbf{q}_{N-1}$ and $\mathbf{q}_N$ occur in the same two subshells, k and k', in both $\psi_{\mathcal{P}\alpha}^{\wp}$ and $\psi_{\mathcal{P}'\alpha'}^{\wp}$ with $(-1)^{p+p} = +1$.

   b) or they differ only in that coordinates of subshell k and k' are swapped in $\psi_{\mathcal{P}\alpha}^{\wp}$ and $\psi_{\mathcal{P}'\alpha'}^{\wp}$, thereby differing by a single permutation such that $(-1)^{p+p'} = -1$.

This two-particle matrix element thus consists of three terms,

$$\begin{aligned} \left\langle \psi_\alpha^{\mathrm{CSF}} \middle| \sum_{i<j}^N g_{ij} \middle| \psi_\alpha^{\mathrm{CSF}} \right\rangle &= \sum_k \frac{w_k(w_k-1)}{2} \left\langle \psi_\alpha^{\wp} \middle| g_{(kk)} \middle| \psi_{\alpha'}^{\wp} \right\rangle \\ &+ \sum_{k<k'}^q w_k w_{k'} \left[\left\langle \psi_\alpha^{\wp} \middle| g_{(kk')} \middle| \psi_{\alpha'}^{\wp} \right\rangle - \left\langle \psi_\alpha^{\wp} \middle| g_{(kk')} \middle| \psi_{\alpha'}^{\wp(ex)} \right\rangle \right] . \end{aligned} \tag{2.50}$$

The first and second terms represent interactions within and between subshells belonging to wavefunctions $\psi^{\wp}$ exactly the same

permutation ordering. The second so-called *direct* term represents interactions between two different subshells. The third term is exactly the same as the second except that the last coordinate of the k:th and k':th subshell is exchanged in the ket-state, denoted by the superscript (ex). This matrix element is known as the *exchange* interaction. The $g_{(kk')}$ operator acts on the last electron coordinates of the k:th and k':th subshells.

2.8 THE MCDHF METHOD

The corner stone of the MCDHF approach is the approximate representation of the atomic energy eigenstate in terms of an *atomic state function* (ASF), given by a linear expansion over n_{CSF} CSF's (2.45),

$$\Psi_i^{ASF} = \left|\Gamma_i J_i^{\pi_i}; \mathcal{E}_i^{DC}\right\rangle \equiv \sum_{r=1}^{n_{CSF}} c_{ri} \left|\gamma_r J^{\pi}\right\rangle \tag{2.51}$$

where c_{ri} is the expansion coefficient of the r:th CSF belonging to the i:th *atomic state function* (ASF), γ_r is a label used to uniquely define the r:th CSF and the Γ is a label usually defined from the dominating component in the expansion (in e.g. jj- or LS-coupling). The ASF's form an orthonormal set so that two eigensolutions i and j satisfy,

$$\mathbf{c}_i^{\dagger}\mathbf{c}_j = \delta_{ij}\,, \tag{2.52}$$

where $\mathbf{c}_i = (c_{1i}, c_{2i}, \ldots c_{n_{CSF}i})^{\dagger}$ is an eigenvector representing the i:th eigenstate.

The energy of an atomic state $\Gamma_i J_i^{\pi_i}$ under the ASF approximation is given by

$$\begin{aligned}\mathcal{E}_i^{DC} &= \left\langle \Gamma_i J_i^{\pi_i} \middle| H^{DC} \middle| \Gamma_i J_i^{\pi_i} \right\rangle \\ &= \mathbf{c}_i^{\dagger} \mathbf{H}^{DC} \mathbf{c}_i \\ &= \sum_r^{n_{CSF}} \sum_s^{n_{CSF}} c_{ri} c_{si} H_{rs}^{DC} = \sum_r^{n_{CSF}} c_{ri}^2 H_{rr}^{DC} + \sum_{r \neq s}^{n_{CSF}} c_{ri} c_{si} H_{rs}^{DC} \end{aligned} \quad (2.53)$$

where $\mathbf{H}^{DC}$ is the matrix of the DC Hamiltonian (2.12) in the CSF representation. The DC Hamiltonian may be replaced by the DCB Hamiltonian in a straightforward manner. It is in general useful to consider the simpler diagonal and the off-diagonal contributions separately, but since we try to keep the discussion as compact as possible, we will describe them together.

The CI method simply diagonalizes the Hamiltonian matrix in a representation of CSF's built from *fixed orbitals*, leading to atomic eigenstates given by the mixing coefficients of the ASF eigenvectors $\mathbf{c}_i$ with corresponding energy eigenvalues, $\mathcal{E}_i^{DC}$. The MCDHF method is essentially a sequence of CI steps during which the radial Dirac orbitals used to construct the CSF's and thus the Hamiltonian matrix, are adjusted by solving a set of one-electron equations similar to (2.35). This corresponds to an iterative non-linear procedure which is continued until self-consistence is achieved in both the mixing coefficients and the radial orbitals. The full MCDHF scheme will be outlined after a brief introduction to the calculation of the energy matrix elements.

2.8.1 *Energy Matrix Elements*

The matrix elements $\mathbf{H}_{rs}^{DC}$ in (2.53) can be expressed in terms of *spin-angular coefficients* (which also contains effective subshell occupations), and *radial integrals*. They can be obtained in a similar fashion as in the methodology leading up to (2.49) and (2.50),

but with additional consideration to off-diagonal contributions. As usual the elements are separated in one- and two-body terms,

$$\begin{aligned} H_{rs}^{DC} &= \langle \gamma_r J^\pi M | H^{DC} | \gamma_s J^\pi M \rangle \\ &= \sum_{ab} t_{ab}^{rs} I(a,b) + \sum_k \sum_{abcd} v_{abcd;k}^{rs} R^k(ab,cd) \end{aligned} \tag{2.54}$$

where e.g. a represents subshell $n_a\kappa_a$ and k is a parameter associated to the regular Legendre expansion of the inter-electronic Coulomb potential,

$$\frac{1}{r_{12}} = \sum_k \frac{r_<^k}{r_>^{k+1}} \mathcal{P}_k\big(\cos(\theta)\big) \tag{2.55}$$

where $r_< = \min(r_1, r_2)$, $r_> = \max(r_1, r_2)$ and θ the relative angle between $\mathbf{r}_1$ and $\mathbf{r}_2$. The sum over k has bounded limits which depend on the total angular momenta j_a and j_b of the subshells under consideration [36, Ch. 7.3].

The parameters t_{ab}^{rs} and $v_{abcd;k}^{rs}$ are *spin-angular coefficients*. In the special case of diagonal elements, the former is reduced to the occupation number $t_{aa}^{rr} = w_a^r$ of subshell a in the r:th CSF, just like in (2.49). The evaluation of these coefficients is however much more involved in the general off-diagonal case. All of the work presented in this thesis, and to large extent the whole computational atomic structure community, relies upon the efficient determination of t and v via the latest angular-momentum methods developed by Gaigalas et al. and the Vilnius group [96–98]. This approach is based on a combination of second quantization in the coupled tensorial form, angular momentum theory in the orbital, spin and quasispin spaces, as well as graphical techniques.

The radial *one-body integral* is given from the Dirac operator (2.7) and the Dirac orbitals (2.34),

$$I(a,b) = \delta_{\kappa_a \kappa_b} \int_0^\infty \Big\{ P_a(r) \Big[V_{\text{nuc}}(r) P_b(r) - c \left(\frac{d}{dr} - \frac{\kappa_a}{r} \right) Q_b(r) \Big] + Q_a(r) \Big[c \left(\frac{d}{dr} + \frac{\kappa_a}{r} \right) P_b(r) + \left(V_{\text{nuc}}(r) - 2c^2 \right) Q_b(r) \Big] \Big\} dr \,. \tag{2.56}$$

The radial *two-body integral* is determined from an expansion of the inter-electronic Coulomb interaction in terms of Legendre polynomials (2.55), which results in the *relativistic Slater integrals*,

$$R^k(ab, cd) = \int_0^\infty \frac{1}{r} \Big[P_a(r) P_c(r) + Q_a(r) Q_c(r) \Big] Y^k(bd; r) dr \,, \tag{2.57}$$

with relativistic Y^k-functions defined by,

$$Y^k(bd; r) = r \int_0^\infty \frac{r_<^k}{r_>^{k+1}} \Big[P_b(s) P_d(s) + Q_b(s) Q_d(s) \Big] ds \,. \tag{2.58}$$

2.8.2 *The Self-consistent MCDHF Scheme*

To derive the MCDHF equations we begin by requiring the ASF eigenenergy E_i^{DC} (2.53) to be stationary with respect to variations in the n_{CSF} mixing coefficients $\mathbf{c}_i$ and the sets of radial functions $\{P(r)\}$ and $\{Q(r)\}$, under appropriate orthonormality constraints. Formally we apply the variational principle [53] to an energy functional formed from the just derived DC matrix element (2.53) together with Lagrange multipliers, λ, introduced to ensure radial

normalization as well as orthogonality between the Dirac orbitals with equal κ, and thus between the CSF's [36, 52],

$$\mathcal{F}\left[\{c\},\{P\},\{Q\};\Gamma J^{\pi}\right] \equiv \left\langle \Gamma J^{\pi}\middle|H^{DC}\middle|\Gamma J^{\pi}\right\rangle + \sum_{ab} \delta_{\kappa_a\kappa_b}\lambda_{ab}\mathcal{C}_{ab} \quad (2.59)$$

representing a single eigenstate ΓJ^{π}, where the orthornormality constraint between subshell a and b is defined as

$$\mathcal{C}_{ab} \equiv \int \left[P_a(r)P_b(r) + Q_a(r)Q_b(r)\right] dr - \delta_{n_a n_b} = 0\,. \quad (2.60)$$

As was hinted earlier, the MCDHF approach consists of two fundamental and very distinct phases - the CI phase and the orbital-determination phase.

The CI phase: For a given set of radial functions $\{P_{n\kappa}(r), Q_{n\kappa}(r)\}$, initially given by e.g. screened hydrogenic orbitals, the requirement that E^{DC}_{Γ} should be stationary with respect to the variations in the mixing coefficients δc_i subject to (2.52) leads to the energy eigenvalue problem,

$$\left[\mathbf{H}^{DC} - \mathcal{E}^{DC}_i \mathbf{1}\right]\mathbf{c}_i = 0\,. \quad (2.61)$$

This gives multiple solutions $\{\mathbf{c}_i, \mathcal{E}^{DC}_i\}$ among which the appropriate one corresponding to the desired eigenstate ΓJ^{π} has to be selected, since this will define the energy functional (2.59). A subset of eigenvectors can be solved for via e.g. the Davidson algorithm [99].

The orbital-determination phase: On the other hand, for a given set of mixing coefficients, $\mathbf{c}_i$, the stationary condition of energy functional $\mathcal{F}$ (2.59) with respect to the coupled variations in the

radial functions $\delta P_{n\kappa}(r)$ and $\delta Q_{n\kappa}(r)$ leads to a the set of *coupled integro-differential equations* - the MCDHF equations:

$$w_a \begin{bmatrix} V_{+1}(a;r) & -c\left(\frac{d}{dr} - \frac{\kappa_a}{r}\right) \\ c\left(\frac{d}{dr} + \frac{\kappa_a}{r}\right) & \left(V_{-1}(a;r) - 2c^2\right) \end{bmatrix} \begin{bmatrix} P_a(r) \\ Q_a(r) \end{bmatrix} = \sum_b \epsilon_{ab}\delta_{\kappa_a\kappa_b} \begin{bmatrix} P_b(r) \\ Q_b(r) \end{bmatrix}, \quad (2.62)$$

where w_a is the effective occupation number of subshell a deduced from the CI step (2.61). The equations are then solved for each subshell to obtain pairs of bound state radial functions $P_{n\kappa}(r)$ and $Q_{n\kappa}(r)$, under the boundary conditions,

$$\begin{aligned} &P_a(r=0) = 0\,, \quad Q_a(r=0) = 0 \\ &P_a(r\to\infty) = 0\,, \quad Q_a(r\to\infty) = 0 \\ &P'(r\to 0) > 0\,, \end{aligned} \quad (2.63)$$

where the latter is chosen by convention. Positive energy solutions can be enforced by essentially requiring $P_{n\kappa}(r)$ to be larger than $Q_{n\kappa}(r)$ [100], e.g. given by the sign of γ in (2.38) and (2.39).

The energy matrix $\epsilon_{ab} = \epsilon_{n_a n_b}$ is determined from the above introduced Lagrange multipliers to ensure orthogonality between orbitals of same κ. The average and central-field MCDHF potential is defined by its action on a radial orbital,

$$V_\beta(a;r)R_a^\beta \equiv V_{\rm nuc}(r)R_a^\beta + Y(a;r)R_a^\beta + X^\beta(a;r)\,, \quad (2.64)$$

where $R_a^\beta(r)$ is defined as $P_a(r)$ for $\beta = +1$ and $Q_a(r)$ for $\beta = -1$. This potential is constructed from a radial *nuclear charge distribution* of choice, $V_{\rm nuc}(r)$, the *direct* term, $Y(a;r)$, and the non-local *exchange* term, $X(a;r)$. The expressions for the generalized direct and exchange potentials, involving in addition to diagonal terms also off-diagonal contributions, are quite lengthy and as such we do not give them here but refer the reader to Eq. (43) and (44) of Dyall et al. [101], or alternatively Eq. (7.3.10) and (7.3.11) in the

book by Grant [36]. Note the shift of $-mc^2$ in (2.62) with respect to the previously derived independent particle central-field equations (2.35); introduced here for the solutions to agree with the corresponding non-relativistic eigenenergies.

The secular problem (2.61) and the MCDHF equations (2.62) have to be solved simultaneously in an iterative SCF procedure until convergence in the behavior of the radial orbitals as well as the expansion coefficients.

A small modification of the single ASF MCDHF method via the so-called *extended optimal level* (EOL) scheme [36, 101] allows for a simultaneous optimization of up to hundreds of eigenstates. This is accomplished by defining an alternative energy functional from a weighted linear combination of single-state functionals (2.59), such that a corresponding *set of eigenstates* are optimized, instead of just one.

The EOL energy functional is expressed in terms of the statistical weight of each targeted eigenstate, i, such that it takes the form of a weighted sum over n_{ASF} eigenenergies,

$$\mathcal{F}^{\text{EOL}}\left[\{c\},\{P\},\{Q\}\right] \equiv \frac{\sum_i^{n_{\text{ASF}}}(2J_i+1)\mathcal{E}_i^{\text{DC}}}{\sum_i^{n_{\text{ASF}}}(2J_i+1)} + \sum_{ab}\delta_{\kappa_a\kappa_b}\lambda_{ab}\mathcal{C}_{ab}\,. \quad (2.65)$$

The EOL method is used throughout this work, but it should be noted that there exists numerous other similar MCDHF schemes for determination of multiple states, such as the *extended average level* scheme which only accounts for diagonal elements in the variational process [36, Ch. 7.3].

The full MCDHF SCF scheme for calculation of n_{ASF} ASF's in a basis of n_{CSF} CSF's, can now be summarized in 7 steps:

1. *Define energy expression:* The energy functional (2.65) is determined from an estimated set of mixing-coefficients vectors,

$\{\mathbf{c}_i^{\text{est}},\ i = 1, \ldots,\ n_{\text{ASF}}\}$.

2. *Calculate the* MCDHF *potential:* The total average potential $\mathcal{V}$ (2.64) is calculated from an estimated set of radial functions, $\{P_a^{\text{est}}(r)\}$ and $\{Q_a^{\text{est}}(r)\}$.

3. *The orbital-determination phase:* Solve the MCDHF equations (2.62) in the just determined potential resulting in a new set of improved radial functions , $\{P_a^{\text{new}}(r)\}$ and $\{Q_a^{\text{new}}(r)\}$.

4. *Improve radial functions:* Obtain an improved set of radial functions according to,

$$\begin{pmatrix} P_a^{\text{est}}(r) \\ Q_a^{\text{est}}(r) \end{pmatrix} \rightarrow (1-\eta_a) \begin{pmatrix} P_a^{\text{new}}(r) \\ Q_a^{\text{new}}(r) \end{pmatrix} + \eta_a \begin{pmatrix} P_a^{\text{est}}(r) \\ Q_a^{\text{est}}(r) \end{pmatrix}$$

   where $0 \leqslant \eta_a < 1$ are damping/acceleration parameters, dynamically defined depending on the current convergence trend.

5. *The CI-phase:* Solve the secular problem (2.61) with a Hamiltonian matrix obtained from the new improved radial functions, $\{P_a^{\text{est}}(r)\}$ and $\{Q_a^{\text{est}}(r)\}$. This gives a new set of mixing-coefficient vectors, $\mathbf{c}_i^{\text{new}}$.

6. *Improve eigenvectors:* The set of mixing-coefficient vectors are improved according to

$$\mathbf{c}_i^{\text{est}} \rightarrow (1-\xi_i)\,\mathbf{c}_i^{\text{new}} + \xi_i \mathbf{c}_i^{\text{est}}\,,$$

   where $0 \leqslant \xi_i < 1$ are damping/acceleration parameters. Note that ξ is typically set to zero in practical implementations of the MCDHF method.

7. *Check convergence:* If the improved set of mixing-coefficient vectors $\{\mathbf{c}_i^{\text{est}}\}$ and radial functions $\{P_a^{\text{est}}(r)\}$ and $\{Q_a^{\text{est}}(r)\}$ all agree with the previous sets to within a specified tolerance, then exit the SCF loop. If not, then restart at *step 1*.

This SCF procedure is illustrated in Fig. 2.4.

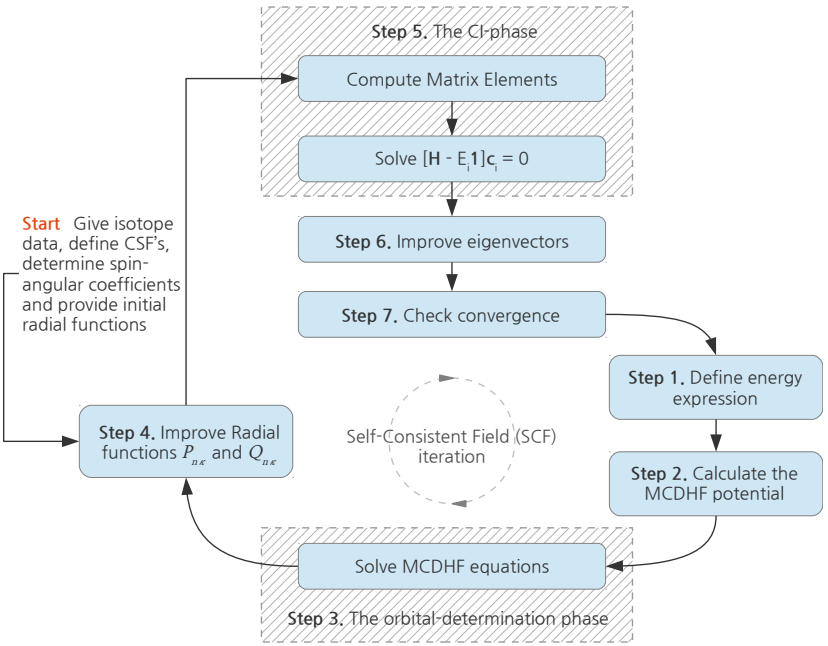

Figure 2.4: The MCDHF SCF procedure, divided into 7 steps as described in the text. The iterations are continued until convergence in both the mixing coefficients and the shape of the radial one-electron functions.

2.8.3 *Excited States - the HUM Theorem*

The MCDHF procedure applies also to excited states via an extension of the regular variational principle to multiconfigurational wavefunctions known as the *Hylleraas-Undheim-MacDonald* (HUM) theorem [35]. Consider an expansion of a certain symmetry J^π, the HUM theorem then states that an increase of the basis-size from M to $M+1$, implies an inequality relation among the energy eigenvalues,

$$\dots E_{k-1}^{M} \leqslant E_{k}^{M+1} \leqslant E_{k}^{M} \dots \tag{2.66}$$

of the excited states,

$$\left\{ \left| \Psi^{\text{ASF}}(\Gamma_i J^\pi) \right\rangle ; \, i = 1, \dots, k, \dots \right\}^{M},$$

under the requirement that state k is orthogonal to all lower states. Thus, for a hypothetically complete basis set representing the J^π symmetry under consideration, the k:th lowest eigenvalue of the system of size M is an upper bound to the corresponding energy of the k:th *exact* excited state,

$$E_{k}^{\text{exact}} \leqslant E_{k}^{M}, \tag{2.67}$$

so that the approximate energy calculated for an excited state of a certain symmetry, will always be an upper bound to the exact energy of the same state. Note that the $k-1$ lower states do not have to be exact solutions for the theorem to be valid.

2.9 THE ACTIVE SPACE METHOD

Before moving on the last subject of this chapter which is classification of electron correlation, we outline a systematic scheme to generate a CSF basis set in the so-called *active space method*:

1. *Define the multireference:* The starting point of this approach is to first identify the zeroth-order wavefunction $\psi^{(0)}$ for the system at hand in terms of a set of important and strongly interacting CSF's. By strongly interacting we mean large mixing coefficients for some eigenstate i, which to first order in some interaction H are given by,

$$c_{ri} \approx \frac{\left\langle \psi^{\text{CSF}}(\gamma_r J^\pi) \middle| H \middle| \psi^{\text{CSF}}(\gamma_0 J^\pi) \right\rangle}{E_0 - E_r}, \tag{2.68}$$

   where $\psi^{\text{CSF}}(\gamma_0 J^\pi)$ is some initial reference state and $r \neq 0$. These CSF's form what is termed the *multireference* (MR) set, and should at least include the dominating CSF's of each physical state of interest, say $1s^2\,2s^2\;J = 0$ for the ground-state of Be-like systems. Additional CSF can then be included in the MR to improve the zeroth-order representation, for the Be-like ground-state that would e.g. be to add the two $1s^2\,2p_\pm^2\;J = 0$ CSF's. The construction of the MR constitute one of the most crucial points in multiconfigurational methods; a subject to which we will return to in the following section during the discussion about static electron correlation.

2. *Define an active set of orbitals:* The next step is to define an *active set* (AS) of one-electron Dirac orbitals consisting of at least the orbitals which build the CSF's in the MR set. A subset of these which build the CSF's dominating the physical states, are required have the expected number of nodes, as specified by the spectroscopic notation nlj and discussed in Sec. 2.6.1. These are referred to as *spectroscopic orbitals*. The remaining orbitals are classified as *correlation orbitals*. The correlation orbitals are different from the spectroscopic ones in the sense that they are not restricted to take a certain node-structure; i.e. their n quantum numbers have no real meaning and are just labels.

3. *Define a set of substitution rules:* The third and last step is to define a set of *rules* describing what type of orbital substitutions are allowed from the CSF's belonging to the MR, to

orbitals within the AS defined in step 2. In some more detail, these rules typically specify the maximum number of substitutions that are allowed from each of the subshells of the reference CSF's. If one orbital is allowed to be substituted from a certain subshell, it is called a *single* (S) substitution. *Double* (D) substitutions correspond to the substitution of two electrons belonging to the same or two different subshells. Three substitutions are called *triple* (T), four *quadruple* (Q) and so one. The fact that the DC (or DCB) Hamiltonian is a two-electron operator suggests that on one should at least include S and D substitutions. Higher order effects are often better captured by expanding the set of reference CSF's in the MR.

The active space approach for constructing a CSF basis set, can be summarized as follows,

$$\begin{aligned}\left\{\phi(n_i\kappa_i),\, i=1,\ldots,n_{AS}\right\}^{AS}&\\ +\left\{\psi_i^{(0)},\, i=1,\ldots,n_{MR}\right\}^{MR}&\\ +\left[\textit{rules}\right]&\\ \longrightarrow\left\{\psi_i^{(1)},\, i=1,\ldots,n_{CSF}\right\}^{\text{CSF basis}}&.\end{aligned}\tag{2.69}$$

If the space of CSF's generated from the defined MR, AS and set of rules, consists of all possible CSF's allowed by the Pauli principle and the present angular momentum coupling scheme, it is called a *complete active space* (CAS). The CAS expansion easily takes unmanageable proportions for larger AS's, and further constraints on the generation procedure would have to be imposed. A convenient approach to deal with this is define additional restriction on e.g. the subshell occupation numbers. This is called the *restricted active space* (RAS) method [102] and is the most commonly adopted scheme in practice.

Expansions of RAS type have the important property of being *closed under de-excitation*, i.e. that the CSF's which are generated by replacing one orbital from subshell $n\kappa$ with an orbital from a subshell $n'\kappa'$ where $n' < n$, already exists in the original set of CSF's.

This implies that RAS expansions can handle general orbital rotations; a result which is of fundamental importance during orthogonalization of two independently optimized sets of orbitals via so-called *biorthogonal transformation* techniques [103]. Such transformations are often necessary during calculation of parity-breaking radiative transition properties (e.g. E1, M2 and E3 multipoles), since calculations generally are performed for states of a single parity at a time. We will return to this subject in the section concerning radiative transitions in the following chapter.

2.10 ELECTRON CORRELATION

The most common starting point for solving the atomic many-electron problem is probably the well-known HF approximation with the anti-symmetric wavefunction represented by a single Slater determinant. In this approximation, each electron is assumed to move independently in a field determined by the nucleus and the other electrons; there is, so to say, no correlation in the movement of the electrons. With this in mind, the concept of *correlation energy* was coined by Löwdin in 1955 [104] as the difference between the exact energy to the non-relativistic many-body Schrödinger equation, E_{exact} and the single-determinant HF energy, $E_{\text{SD}}^{\text{HF}}$.

However, in the relativistic many-electron approach used in the present work, we will define correlation energy slightly different; the contributions from correlation will first of all be defined in the regime of a relativistic DC (or DCB) Hamiltonian, possibly including also contributions from leading order QED effects, instead of the regular non-relativistic Hamiltonian. Another difference is that we make use of the angular-momentum coupled CSF basis introduced earlier, which can be represented by a linear combination of determinants. With this set-up, our notion of electron correlation energy is defined by,

$$E^{\text{corr}} = E^{\text{exact}} - E_{\text{CSF}}^{\text{DHF}}, \tag{2.70}$$

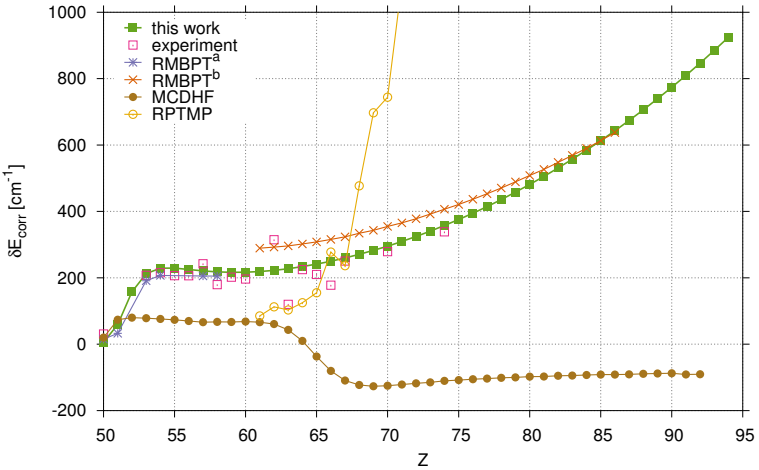

Figure 2.5: Estimated absolute contributions from electron correlation to the $4f\,^2F^o$ fine structure separation ($\delta E_{corr} = E^{method} - E^{DHF}_{CSF}$ where the "method" superscript should be replaced by the corresponding label in the legend) for experiment and other available theory (RMBPT[a] [105], RMBPT[b] [105] (from [106]), MCDHF [107] and relativistic perturbation theory with a model potential (RPTMP) [106, 108]).

where E^{DHF}_{CSF} is the result from a single-CSF DHF calculation.

It is useful to separate electron correlation contributions into Fermi, static and dynamic correlation:

1. *Fermi Correlation* The correlation energy which arises from the Pauli antisymmetry of the wavefunction - the Fermi statistics. This contribution is accounted for already at the single-determinental level and as such it is not classified as *correlation energy* in the definition of Löwdin, but is mentioned here nevertheless for completeness of the discussion.

2. *Static Correlation* The part of the electron-electron interaction which corresponds to the long-range rearrangement of the electron charge density due to strongly interacting CSF's,

to first-order defined by (2.68), is called static correlation[9]. This type of correlation is treated by the CSF's included in the MR set, as defined in Sec. 2.9. Systems with an abundance of static correlation are generally unfit to treat via pure perturbative methods, and best attacked with non-perturbative multireference approaches, such as CI or MCSCF, through a carefully designed MR set[10].

Analyzing static correlation by the means of *Z-dependent perturbation theory* [35, Ch. 4.2] reveals that the CSF's to be included in the MR are the ones of equal parity and which are built from a set of orbitals $n\kappa$ having the same principal quantum numbers, n, as the main reference state(s) of interest. These CSF's are said to belong to the *complex*, a term coined by Layzer [109–111], which forms the most fundamental starting point for the construction of an appropriate MR set.

3. *Dynamic Correlation* The remaining correlation energy not resulting from the bulk of strongly interacting CSF's, is called dynamic correlation.

    a) *Short-range Dynamic Correlation* The part of the dynamic correlation which is related to the representation of the inter-electronic Coulomb cusp, arising from the singularity of $1/r_{ij}$ close to the point of electron coalescence where $r_{ij} = 0$ (see the discussion in Sec. 2.5.1 for further details). Fig. 2.3 illustrates this effect in the He-like ground-state wavefunction compared to a HF solution. The HF wavefunction lacks the cusp and therefore overestimates the probability for two electrons to be close to each other, resulting in an overestimation of the electron-electron repulsion energy. Contributions from

9 Static correlation is also known as near-degeneracy or non-dynamical correlation.

10 Defining the MR can indeed be a complicated task for complex systems of many electrons. It often requires a detailed analysis of the system at hand since its form can have a huge impact on the performance of the correlation model.

short-range dynamic correlation are especially prominent for pairs of electrons with opposite spin, i.e. singlet states in LSJ coupling, since the electrons are allowed to occupy the same region in space.

b) *Long-range Dynamic Correlation* The correlation in the movement between electrons located far away from each other; i.e. not in a cusp-environment.

Since a DHF solution is the starting point for most relativistic methods, it is often useful to compare different models by just the correlation energy. As an example of this we use a result from one of the papers in this thesis [A_{VI}] on the ground-term energy separation and the connecting forbidden M1 transition in Ag-like ions. Fig. 2.5 shows how the electron correlation energy contribution to the $4f\ ^2F$ fine-structure separation varies along Ag-like iso-electronic sequence for a calculation made by us, compared to experiment and some other calculations.

2.11 CORRELATION CLASSIFICATION OF THE CSF'S

The representation of the atomic eigenstates in terms of ASF's allows for an additional classification of electron correlation, given by groups of CSF's analyzed with respect to the zeroth-order wavefunction, $\psi^{(0)}$, formed from the MR set. For the present discussion we restrict the MR to a single-reference state, $\psi^{(0)}(\gamma J^{\pi})$. Most fundamentally we distinguish between those CSF's that are formed from S substitutions $\{\psi^{(S)}\}$ and those formed from D substitutions, $\{\psi^{(D)}\}$.

In non-relativistic theory it can be convenient to further classify the $\{\psi^{(S)}\}$ set into groups of CSF's representing *radial correlation* as well as *spin* and *orbital* polarization [35, Ch. 4.2.2]. S substitutions from inner ns-subshells, representing polarization of the core, are of fundamental importance to the calculation of atomic properties

with a strong dependence the wavefunction in the vicinity of the nucleus, such as hyperfine interaction or nuclear recoil effects. We will return to the treatment of hyperfine interaction in Ch. 5.

In order to classify the set of CSF's formed from D substitutions, $\{\psi^{(D)}\}$, we first need to divide the electron configuration into *core* and *valence* subshells. Deciding on an electron core is directly related to the definition of the *substitution rules* in the RAS approach in Sec. 2.9, and as such it is one of most important decisions in the construction of correlation models. It is generally a good idea to define all subshells belonging to the outermost *shell* (all subshells with same principal quantum number) as valence subshells. This might not always be possible for heavy nuclei with many electrons, in which case the choice of core becomes a delicate task. The situation generally becomes harder at the neutral end of an isoelectronic sequence, and worst are the negative ions where the amount of correlation energy is as large as it can be in comparison with the central nuclear potential. The calculation of wavefunctions and physical properties of negative ions is indeed a complex task which requires much insight and experience with correlation calculations (see e.g. the work on isotope shifts in the S^- and Cl^- electron affinities by Carette et al. [112–114]).

Let a and b be two occupied orbitals of a CSF in a MR set. The set of CSF's formed from substitution of a and b with virtual orbitals in the AS may be classified according to different correlation types:

1. *Valence-Valence Correlation* The orbitals a and b belong to the valence subshells. CSF's of this type represents correlation among the outer electrons, and thus termed *valence-valence correlation* (VVC).

2. *Core-Valence Correlation* One of the orbitals a and b belongs to the valence and the other to the core subshells. This group of CSF's represents interactions between the core and valence electrons, and is therefore referred to as *core-valence correlation* (CVC).

3. *Core-Core Correlation* Both a and b belong to the core. These CSF's represents electron correlation within the core, thus called *core-core correlation* (CCC).

2.12 CHAPTER SUMMARY

This chapter has aimed at introducing and motivating relativistic many-body theory and methods for atomic systems, and the MCDHF approach in particular.

We first argued for the need of approximate methods due to the complexity of the atomic many-electron wavefunction. We then motivated the need for a relativistic treatment in heavy systems, or systems which are sensitive to the inner electrons which move at relativistic speeds. In this discussion we introduced the important concepts of direct relativistic effects - contraction of inner orbitals - and indirect relativistic effects - expansion of outer orbitals due to the increased screening of the contracted orbitals.

Next we introduced the relativistic atomic many-body Hamiltonian. We discussed the Coulomb interaction and its reclusive cusp condition - the discontinuity in the derivative of the wavefunction at $r_{ij} = 0$ which is very difficult to represent, and thus one of the major challenges to many-electron methods. The Breit interaction which represents transverse magnetic and retardation effects was introduced to correct for the simplistic Coulomb-interaction. And finally we discussed radiative QED corrections from one-loop electron self-energy - self-interaction via virtual photons - and vacuum polarization - electron-positron pair-production in the field of the nucleus.

After that we discussed the independent particle and central field approximations which allowed for derivation of radial differential equations and we showed the solutions for a simple Coulomb central field potential. This was followed by a motivation and defi-

nition of the angular-momentum coupled and explicitly antisymmetrized many-electron CSF basis, and the basic ideas behind evaluation of one- and two-electron matrix elements in this representation.

We then introduced the MCDHF approach in some detail. We outlined the fundamental theory and summarized the self-consistent procedure in seven steps. In relation to this, we outlined the active space approach for a systematic generation of CSF basis sets. We then finally ended this chapter by introducing and defining the concept of electron correlation as a representation of many-electron effects.

3

RADIATIVE MULTIPOLE TRANSITIONS

In the theory of QED, electrons are limited to interactions with photons (neglecting much weaker effects[1]).

The ground-state for the electromagnetic field is known as the *QED vacuum*. Taking interactions of the atomic electrons with this field into account will perturb the stationary states described by e.g. an ASF. Stationary energy eigenstates are therefore never true eigenstates of the Hamiltonian describing the actual physical system, resulting in non-zero overlaps of an excited state with e.g. the ground-state, to which it will decay by emission of, at least, one photon. This is why all atomic states, with the sole exception of the ground-state, have finite radiative lifetimes. Without the fundamental interaction between charged particles (electrons) and photons[2], as predicted by the theory of QED, isolated atoms and ions would stay forever in their excited states.

It can be shown with time-dependent perturbation theory [50] that the probability for a spontaneous emission of a photon per unit time (in atomic units) due to the transition from a stationary excited atomic eigenstate Ψ_j to a lower state Ψ_i, is given by,

$$A_{j\to i} = 2\pi \left|\left\langle \Psi_i \middle| H_{int} \middle| \Psi_j \right\rangle\right|^2 \rho_i \,, \tag{3.1}$$

1 I.e. contributions from e.g. the *weak interaction* between electrons and Z^0 bosons, and *electron capture* in which the nucleus absorbs an inner atomic electron so that a proton transforms to a neutron under the emission of an electron neutrino, $p + e^- \to n + \nu_e$.

2 The coupling strength between charged particles and photons is scaled by the fine-structure constant, $\alpha \approx 1/137$, which acts as the coupling constant for the electromagnetic force.

a result known as *Fermi's golden rule*, where ρ_i is the density of final states. H_{int} is a suitable many-body Hamiltonian describing the electron-photon interaction,

$$H_{int} = \sum_{l}^{N} h_{int}(x_l)\,, \tag{3.2}$$

where the sum runs over all N electrons, $x = (ct, \mathbf{r})$ is the space-time four-vector. The interaction of a single electron with an external free-photon field, $h_{int}(x_l)$, is given by the scalar ϕ and vector $\mathbf{A}$ potentials[3],

$$h_{int}(x) = e\{-c\boldsymbol{\alpha}\cdot\mathbf{A}(\mathbf{r},\omega) + \phi(\mathbf{r},\omega)\}\, e^{-\imath\omega t}\,, \tag{3.3}$$

where $\hbar\omega$ is the electromagnetic energy at the space-time point $x = (ct, \mathbf{r})$ and the dot-less $\imath$ denotes the imaginary unit $\sqrt{-1}$.

Apart from energies, the most important physical observable for atomic systems, is probably the "intensity" of emitted or absorbed radiation. The interaction between light and matter is central to our understanding of the universe, which makes the quantum theory of radiative transitions a fundamental part of atomic structure theory. As an example, in order to analyze optical spectra from, a stellar atmosphere to obtain information on element abundances or temperatures, a detailed knowledge about the radiative transitions are required.

In the following we closely follow the work of Grant [36, 115] and outline how transition rates can be evaluated in a relativistic many-electron framework.

3.1 THE FREE-RADIATION FIELD ON MULTIPOLE FORM

We saw in Eq. (3.3) that, in order to fully specify the interaction Hamiltonian we need to find a convenient representation of the

3 Note that we have left out all gauge-dependent terms for the time being.

scalar ϕ and vector $\mathbf{A}$ free-photon fields. In relativistic theory, the fields are expressed in terms of the four-potential [36, Ch. 8.1.2],

$$a_\mu(x;\omega) = \big(\phi(x;\omega),\ -c\mathbf{A}(x;\omega)\big)_\mu\,, \tag{3.4}$$

where $\mu \in \{0,1,2,3\}$ is a relativistic index. The four-potential is required to satisfy the relativistic version of Maxwell's equations; the *wave equation* (I) and *Lorenz (transversality) condition*[4] (II),

$$\begin{cases} (\mathrm{I}) & \Box a_\mu(x;\omega) &= 0 \\ (\mathrm{II}) & \partial_\mu a_\mu(x) &= 0\,, \end{cases} \tag{3.5}$$

respectively, where $\Box = \partial^\mu\partial_\mu = (\partial/c\partial t)^2 - \boldsymbol{\nabla}^2$ is the d'Alembertian operator in Minkowski space where implicit summation over covariant and contravariant indices are implied.

As was hinted in (3.3), the solutions exhibit harmonic time dependence $e^{-\imath\omega t}$. Considering the spacial parts, the wave equation (I) has scalar plane-wave solutions with of the form $\phi(\mathbf{r};\omega) = e^{\imath\tilde{\mathbf{k}}\cdot\mathbf{r}})$, where $\tilde{\mathbf{k}}$ is the wavenumber[5] satisfying $|\tilde{\mathbf{k}}|^2 = \omega^2$, which is conveniently expressed as an expansion over multipole operators [36, Eq. (8.1.12)],

$$\phi_{k,q}(\mathbf{r};\omega) = \left(1 - \imath\frac{\omega}{c}G_k\right)\imath^k(2k+1)\,j_k(\omega r/c)\,C^k_q(\theta,\varphi) \tag{3.6}$$

where C^k_q is the q:th component of a renormalized spherical harmonic of rank k,

$$C^k_q(\theta,\varphi) = \sqrt{\frac{4\pi}{2k+1}}Y_{k,q}(\theta,\varphi)\,, \tag{3.7}$$

and $j_k(\omega r/c)$ are Bessel functions given by the expansion,

$$j_k(\omega r/c) = \frac{(\omega r/c)^k}{(2k+1)!!}\left\{1 - \frac{(\omega r/c)^2}{2(2k+3)} + \dots\right\} \qquad |\omega r/c| \ll 1\,. \tag{3.8}$$

4 The *Lorenz condition* is frequently called the *Lorentz condition* because of confusion with Hendrik Lorentz, who gave name to *Lorentz covariance/invariance*.

5 The tilde is introduced to clearly distinguish the scalar wavenumber $|\tilde{\mathbf{k}}| = \tilde{k}$ from the tensor rank, k.

The *gauge parameter* G_k can in theory be set to any value without changing the field equations [36, Ch. 2.6.3]. The two most common choices are however,

$$G_k = \begin{cases} \sqrt{(k+1)/k} & \textit{Babushkin (length) gauge} \\ 1 & \textit{Coulomb (velocity) gauge}\,. \end{cases} \tag{3.9}$$

The scalar solution (3.6) and the Lorenz condition (II) (3.5), which can be expressed on the non-relativistic form,

$$\operatorname{div} \boldsymbol{A} + \frac{1}{c^2}\frac{\partial \phi}{\partial t} = 0\,, \tag{3.10}$$

gives three independent *vector potential* solutions [115],

$$c\boldsymbol{A}^{e}_{k,q}(\boldsymbol{r};\omega)\,, \quad \text{and} \quad c\boldsymbol{A}^{m}_{k,q}(\boldsymbol{r};\omega)\,, \quad c\boldsymbol{A}^{l}_{k,q}(\boldsymbol{r};\omega)\,, \tag{3.11}$$

representing potentials of electric (e), magnetic (m) and longitudinal (l) type respectively. Both $\boldsymbol{A}^e$ and $\boldsymbol{A}^m$ are polarized perpendicular to the photons propagation vector such that $\boldsymbol{A}^e \cdot \tilde{\boldsymbol{k}} = 0$, and are therefore referred to as transverse potentials. $\boldsymbol{A}^l$ is polarized in the direction of the photon propagation, which gives its name. These solutions are mutually orthogonal with respect to integration over the unit sphere.

Following Grant [36, Eq. (8.1.10-11)] one can express the potentials explicitly in terms of compound spherical tensor operators,

$$\begin{aligned} c\boldsymbol{A}^{e}_{k,q}(\boldsymbol{r};\omega) = &-\imath^{k+1}\sqrt{k(2k+3)}\left[\boldsymbol{e}\otimes \boldsymbol{C}^{k+1}\right]^{k}_{q} j_{k+1}(\omega r/c) \\ &-\imath^{k-1}\sqrt{(k+1)(2k-1)}\left[\boldsymbol{e}\otimes \boldsymbol{C}^{k-1}\right]^{k}_{q} j_{k-1}(\omega r/c) \end{aligned} \tag{3.12}$$

$$\begin{aligned} c\boldsymbol{A}^{l}_{k,q}(\boldsymbol{r};\omega) = &-\imath^{k+1}\sqrt{k(2k+3)}\left[\boldsymbol{e}\otimes \boldsymbol{C}^{k+1}\right]^{k}_{q} j_{k+1}(\omega r/c) \\ &+\imath^{k-1}\sqrt{(k+1)(2k-1)}\left[\boldsymbol{e}\otimes \boldsymbol{C}^{k-1}\right]^{k}_{q} j_{k-1}(\omega r/c) \end{aligned} \tag{3.13}$$

$$c\mathbf{A}^{m}_{k,q}(\mathbf{r};\omega) = -\imath^{k}(2k+1)\left[\boldsymbol{e}\otimes\mathbf{C}^{k}\right]^{k}_{q} j_{k}(\omega r/c) \tag{3.14}$$

where,

$$\left[\boldsymbol{e}\otimes\mathbf{C}^{k\pm 0,1}\right]^{k}_{q}, \tag{3.15}$$

are compound tensors of the photon polarization vector $\boldsymbol{e} = \mathbf{r}/|\mathbf{r}|$ (which is perpendicular to the propagation vector $\tilde{\mathbf{k}}$), and renormalized spherical harmonics (3.7), coupled to total rank k, and $j_{k}(\omega r/c)$ are the Bessel functions given by (3.8).

It can be shown [115] that the solutions to (3.10) of electric type, $\mathbf{A}^{e}$, are independent of admixtures from the longitudinal vector potential, $\mathbf{A}^{l}$, and as such freely set by the gauge parameter according to,

$$\mathbf{A}^{e}_{k,q}(\mathbf{r};\omega) \rightarrow \mathbf{A}^{e}_{k,q}(\mathbf{r};\omega) + G_{k}\mathbf{A}^{l}_{k,q}(\mathbf{r};\omega)\,, \tag{3.16}$$

while $\mathbf{A}^{m}_{k,q}(\mathbf{r};\omega)$ is independent of G_{k}. The scalar $\phi_{k,q}$ and vector potentials $\mathbf{A}^{e}_{k,q}$, $\mathbf{A}^{l}_{k,q}$ and $\mathbf{A}^{m}_{k,q}$ are irreducible spherical tensor operators of rank k.

3.2 TRANSITION OPERATORS

Considering the three vector potential solutions on multipole expansion representation, we can separate the one-electron interaction operator h_{int} (3.3) into separate operators for multipole transitions of electric (Ek) and magnetic (Mk) type.

An effective Ek operator can be expressed on a generalized form in terms of the gauge parameter G_{k},

$$\Omega^{E(k)}_{q}(G_{k}) = \Omega^{e(k)}_{q}(0) + G_{k}\Omega^{l(k)}_{q}\,, \tag{3.17}$$

where,

$$\Omega_q^{e(k)}(0) = -c\boldsymbol{\alpha}\cdot\mathbf{A}^e_{k,q}(\mathbf{r};\omega) \tag{3.18}$$

$$\Omega_q^{l(k)} = \phi_{k,q}(\mathbf{r};\omega) - c\boldsymbol{\alpha}\cdot\mathbf{A}^l_{k,q}(\mathbf{r};\omega)\,. \tag{3.19}$$

The Mk operator is given by the magnetic vector potential,

$$\Omega_q^{M(k)} = -c\boldsymbol{\alpha}\cdot\mathbf{A}^m_{k,q}(\mathbf{r};\omega)\,, \tag{3.20}$$

and is therefore gauge-independent.

The $\Omega_q^{E/M(k)}$ operators are 4×4 irreducible spherical tensor operators of rank k, so that it is possible to exploit Racah algebra on the corresponding matrix elements, e.g. to extract certain symmetry properties with the Wigner-Eckart theorem.

In relation to this, Grant [115] discuss that for the gauge-invariance of Ek transitions to be valid, the wavefunctions must satisfy *local charge conservation* at each space-point x, i.e. that physically acceptable wave equations must have a four-current density $j^\mu = (c\rho, \mathbf{j})$ which satisfies the *continuity equation*,

$$\partial_\mu j^\mu = \frac{\partial\rho}{\partial t} + \operatorname{div}\mathbf{j} = 0 \tag{3.21}$$

where $\rho(x)$ is the electron density at x and $\mathbf{j}$ is the associated electron current. Grant argues that, although this is true for exact wavefunctions in general, it is well-known that wavefunctions determined with multireference SCF techniques such as DHF or MCDHF, or their non-relativistic equivalents, give transition properties which are sensitive to the value of G_k. This can be attributed to the fact that the each SCF orbital is determined from non-local potentials coupled to the other orbitals, and as such the concept of local charge conservation becomes much more complex in SCF methods [115]. Nevertheless, a weak dependence on the gauge parameter is generally accepted as a good indication on that effectively complete wavefunctions have been obtained.

3.3 MANY-ELECTRON MATRIX ELEMENTS

The operators (3.17) and (3.20) define one-electron operators while we in the end want to determine many-electron amplitudes in a representation given by the ASF's obtained from MCDHF calculations. To accomplish this we first expand the matrix element in terms of matrix elements between CSF's weighted by mixing coefficients. These are then in turn decoupled into one-electron matrix elements [101, Eq. (60)],

$$\begin{aligned}\left\langle \Gamma_i J_i^{\pi_i} \middle|\middle| \widetilde{\mathbf{\Omega}}^{\Pi(k)}(\omega) \middle|\middle| \Gamma_j J_j^{\pi_j} \right\rangle \\ = \sum_{rs} c_{ri} c_{sj} \sum_{a,b} d^k_{a,b}(i,j) \left\langle n_a \kappa_a \middle|\middle| \mathbf{\Omega}^{\Pi(k)}(\omega) \middle|\middle| n_b \kappa_b \right\rangle , \quad (3.22)\end{aligned}$$

where the $d^k_{a,b}(i,j)$'s are the generalized spin-angular coefficients discussed in the section on the MCDHF method. Note that the *many-electron* transition operator on the left-hand side is denoted with a tilde to distinguish it from the *one-electron* operator.

3.4 ONE-ELECTRON AMPLITUDES

The reduced one-particle matrix element in (3.22) is energy dependent through the scalar, ϕ^k, and vector $\mathbf{A}^k$ potentials which are expressed in terms of spherical Bessel functions $j_{k\pm1}(\omega r/c)$ for the electric and longitudinal parts, and $j_k(\omega r/c)$ for the magnetic.

Following [36, Ch. 8.2.1] we express the reduced one-particle matrix element as,

$$\left\langle n_a \kappa_a \middle|\middle| \mathbf{\Omega}^{\Pi(k)}(\omega) \middle|\middle| n_b \kappa_b \right\rangle = \left\langle j_a \middle|\middle| \mathbf{C}^k \middle|\middle| j_b \right\rangle \mathbf{M}^{e,m}_{ab}(\omega; G_k) , \quad (3.23)$$

where reduced matrix elements of the renormalized spherical harmonics (3.7) are given by,

$$\begin{aligned}&\langle j_a||\mathbf{C}^k||j_b\rangle \\ &\quad = (-1)^{j_a+1/2}\sqrt{(2j_a+1)(2j_b+1)}\begin{pmatrix} j_a & k & j_b \\ 1/2 & 0 & -1/2\end{pmatrix}, \end{aligned} \tag{3.24}$$

and $\mathbf{M}^{e,m}_{ab}(\omega; G_k)$ is a radial matrix element which can be expressed in terms of three fundamental integrals, $I^{\pm}_k$ and J^+_k given by

$$J^+_k(\omega) = \int_0^\infty \Big(P_a(r)P_b(r) + Q_a(r)Q_b(r)\Big)\, j_k(\omega r/c)\, dr \tag{3.25}$$

$$I^{\pm}_k(\omega) = \int_0^\infty \Big(P_a(r)Q_b(r) \pm Q_a(r)P_b(r)\Big)\, j_k(\omega r/c)\, dr \tag{3.26}$$

where j_k is a spherical Bessel function (3.8).

The electronic multipole amplitude resulting from the interaction (3.17) on radial Dirac orbitals,

$$\mathbf{M}^e_{ab}(\omega; G_k) = \mathbf{M}^e_{ab}(\omega; 0) + G_k\mathbf{M}^l_{ab}(\omega), \tag{3.27}$$

can be expressed in terms of the radial integrals (3.25) and (3.26) as follows,

$$\begin{aligned}\mathbf{M}^e_{ab}(\omega;0) = \imath^k\Bigg\{&\sqrt{\frac{k+1}{k}}\Big[(\kappa_a-\kappa_b)I^+_{k-1} - kI^-_{k-1}\Big] \\ &-\sqrt{\frac{k}{k+1}}\Big[(\kappa_a-\kappa_b)I^+_{k+1} + (k+1)I^-_{k+1}\Big]\Bigg\}\end{aligned} \tag{3.28}$$

$$\begin{aligned}\mathbf{M}^l_{ab}(\omega) = \imath^k\Bigg\{&(2k+1)J^+_k - \Big[(\kappa_a-\kappa_b)I^+_{k-1} - kI^-_{k-1}\Big] \\ &-\Big[(\kappa_a-\kappa_b)I^+_{k+1} - (k+1)I^-_{k+1}\Big]\Bigg\}\end{aligned} \tag{3.29}$$

The magnetic multipole amplitude due to the interaction (3.20) is given by,

$$\mathbf{M}^{m}_{ab}(\omega) = -\imath^{k+1}\frac{2k+1}{\sqrt{k(k+1)}}(\kappa_a - \kappa_b)I^{+}_{k}\,. \tag{3.30}$$

These radial matrix elements determines the total many-electron amplitude through (3.23) and (3.22).

3.5 RELATIVISTIC TRANSITION RATES

Following the work of Grant[6] [36, 101, 115] the rate of spontaneous emission of photons with multipolarity Πk = *electric dipole* (E1), *magnetic dipole* (M1), *electric quadrupole* (E2), *magnetic quadrupole* (M2) etc., due to the transition $j \to i$ of energy $\hbar\omega = (\mathcal{E}_j - \mathcal{E}_i)$ between two atomic eigenstates represented by ASF's,

$$\left|\Gamma_j J_j^{\pi_j}; \mathcal{E}_j\right\rangle \to \left|\Gamma_i J_i^{\pi_i}; \mathcal{E}_i\right\rangle, \tag{3.31}$$

induced by a relativistic multipole radiation operator $\widetilde{\mathbf{\Omega}}^{E/M,k}(\omega)$, is given by

$$A^{\Pi k}_{j\to i}(\omega) = \sum_{M_i M_j q} A^{\Pi,k}_{q}(\omega; \Gamma_i J_i^{\pi_i} M_i, \Gamma_j J_j^{\pi_j} M_j)\Big/ g_{J_j}$$

6 Note that the derivations by Grant often use Wigner's covariant 3j m-symbol instead of the regular 3j-symbol. The relation between these notations is

$$\begin{pmatrix} m & k & j' \\ j & q & m' \end{pmatrix}_{\text{(covariant)}} = (-1)^{j-m}\begin{pmatrix} j & k & j' \\ -m & q & m' \end{pmatrix}_{\text{(regular)}}.$$

The more well-known regular form is used in the current presentation to avoid confusion.

$$
\begin{aligned}
&= \sum_{M_i M_j q} \frac{2}{g_{J_j}} \left(\frac{\omega}{c}\right) \left| \left\langle \Gamma_i J_i^{\pi_i} M_i \middle| \widetilde{\Omega}_q^{\Pi(k)}(\omega) \middle| \Gamma_j J_j^{\pi_j} M_j \right\rangle \right|^2 \\
&= \sum_{M_i M_j q} \frac{2}{g_{J_j}} \left(\frac{\omega}{c}\right) \left| (-1)^{J_i - M_i} \begin{pmatrix} J_i & k & J_j \\ -M_i & q & M_j \end{pmatrix} \right. \\
&\qquad \left. \times \left\langle \Gamma_i J_i^{\pi_i} \middle\| \widetilde{\boldsymbol{\Omega}}^{\Pi(k)}(\omega) \middle\| \Gamma_j J_j^{\pi_j} \right\rangle \right|^2 \\
&= 2 \left(\frac{\omega}{c}\right) \frac{\left| \left\langle \Gamma_i J_i^{\pi_i} \middle\| \widetilde{\boldsymbol{\Omega}}^{\Pi(k)}(\omega) \middle\| \Gamma_j J_j^{\pi_j} \right\rangle \right|^2}{(2k+1) g_{J_j}} . \qquad (3.32)
\end{aligned}
$$

This expression is derived under the assumption that space has no preferred spatial direction, i.e. for an atomic system in free space, such that an appropriate total transition rate is defined by averaging over all initial degenerate projections $g_{J_j} = 2J_j + 1$ and summing over all final states. In second step we apply the Wigner-Eckart theorem and in the last step we make use of the orthogonality relation between 3j-symbols [57, Eq. (5.15)].

The lifetime of a certain eigenstate j can be expressed in terms of a sum over transition rates for all possible decay channels,

$$\tau_j = \frac{1}{\sum_{i,\Pi k} A_{j\to i}^{\Pi k}(\omega)} . \qquad (3.33)$$

The *branching fraction*,

$$Q(\Pi k)_j = \tau_j A_{j\to i}^{\Pi k}(\omega) , \qquad (3.34)$$

is the fractional contribution of a certain decay channel $j \to i$ to the total decay rate from a certain excited state j. These two properties are often the quantities possible to measure in an experiment, from which individual transition rates $A_{j\to i}^{\Pi k}$ can be deduced.

The *line strength* $S^{\Pi k}$ is a fundamental quantity in non-relativistic theory due to its energy-independent nature, and as such an im-

portant measure in the evaluation of wavefunction qualities for radiative properties. The non-relativistic definition of $\mathcal{S}^{\Pi k}$ is simply the absolute square of the corresponding non-relativistic reduced transition matrix element,

$$\mathcal{S}^{\Pi k}_{ij\,(\text{non-rel})} = \left|\left\langle \Gamma_i J_i^{\pi_i} \middle|\middle| \mathbf{O}^{\Pi(k)} \middle|\middle| \Gamma_j J_j^{\pi_j} \right\rangle\right|^2 \tag{3.35}$$

where $\mathbf{O}^{\Pi(k)}$ is the standard non-relativistic multipole transition operator [35, 57]. The line strength can be used to express the non-relativistic transition rate,

$$A^{\Pi k}_{j\to i\,(\text{non-rel})} = C_k \left(\frac{\omega}{c}\right)^{2k+1} \frac{\mathcal{S}^{\Pi k}_{ij\,(\text{non-rel})}}{g_{J_j}} \tag{3.36}$$

where $\mathcal{S}$ is completely energy-independent, and the k-dependent prefactor is defined by,

$$C_k \equiv \frac{2(2k+1)(k+1)}{k\left[(2k+1)!!\right]^2}. \tag{3.37}$$

A relativistic "line strength" equivalent to its non-relativistic counterpart, can be defined by solving for $\mathcal{S}$ in the non-relativistic expression for the transition rate, and replace the rate with its relativistic counterpart (3.32), giving,

$$\begin{aligned}\mathcal{S}^{\Pi k}_{ij}(\omega) &\equiv \frac{g_{J_j}}{C_k}\left(\frac{1}{\omega/c}\right)^{2k+1} A^{\Pi k}_{j\to i}(\omega) \\ &= \frac{2}{C_k}\left(\frac{1}{\omega/c}\right)^{2k} \frac{\left|\left\langle \Gamma_i J_i^{\pi_i} \middle|\middle| \widetilde{\mathbf{\Omega}}^{\Pi(k)}(\omega) \middle|\middle| \Gamma_j J_j^{\pi_j} \right\rangle\right|^2}{(2k+1)}.\end{aligned} \tag{3.38}$$

The relativistic line-strength is different from the non-relativistic in that it is energy dependent, although very weakly since the lowest order $(\omega/c)^{2k}$-dependence is canceled out.

Another property, preferred in e.g. stellar astronomy, is the positive and symmetric (under interchange of inital and final state) *weighted oscillator strength*, or gf-value, defined by,

$$\begin{aligned}(gf)^{\Pi k}_{j\to i}(\omega) &= g_{J_j}\frac{1}{2}\frac{c}{\omega^2}A^{\Pi k}_{j\to i}(\omega)\\ &= \frac{1}{\omega}\frac{\left|\left\langle \Gamma_i J_i^{\pi_i}\right|\left|\widetilde{\mathbf{\Omega}}^{\Pi(k)}(\omega)\right|\left|\Gamma_j J_j^{\pi_j}\right\rangle\right|^2}{(2k+1)}\,.\end{aligned} \tag{3.39}$$

Note that the representation of transition properties as simple overlap via the matrix element (3.22), does not include any effects of the perturbation due to the radiation field on the wavefunction in itself. For systems involving strong radiation fields, say an atomic system shined upon by an intense laser, such effects have to be considered. On the other end, for weak radiation fields, such as the regular "free" atomic system perturbed by the vacuum field, these effects might still be of importance if the energy separations are small enough for the radiative width of the states to be of the same order as other perturbations from e.g. hyperfine, Zeeman or Stark interactions. This will be further discussed in Ch. 8 concerning unexpected transitions.

3.6 ORBITAL RELAXATION

Computer code implementations for evaluation of radiative transition properties used to require the CSF's representing the initial and final eigenstates states to be constructed from the same orthonormal set of Dirac orbitals. This implied that *orbital relaxation* effects had to be accounted for via CI, which, for RAS calculations, could give rise to inaccuracies in the calculation of transition properties [36, Ch. 8.4].

This limitation can however be relaxed by constructing the ASF's for the inital and final states from separately optimized orbital

bases, and evaluate the radiative matrix elements by first applying a so-called *biorthogonal transormation* so that the two sets of orbitals become mututally orthonormal while losing their internal orthonormallities. This technique, which is now standard procedure in relativistic and non-relativistic multireference calculations, was a major advancement when first introduced by Malmqvist in the 1980's [103] and has since then been adopted for transition calculations in a MCDHF scheme by Olsen et al. and Jönsson et al. [116, 117] and implemented in the most recent versions of GRASP2K [118, 119]. The possibility to perform separate calculations for initial and final wavefunctions of, say, different parity, has an additional divide-and-conquer bonus effect so that much larger expansions are feasible.

3.7 THE LONG-WAVELENGTH APPROXIMATION

The relativistic expressions for the transition amplitude are indeed quite involved, so in order to gain some insight in for example the energy dependence and relation between the amplitudes of different multipoles, we evaluated the amplitudes for interaction with long wavelength photons. In this approximation it is assumed that the value for the wavelength λ of the observed photon is large in comparison to the size of the atom, i.e. that $\omega r/c$ is small.

Considering the scalar (3.6) and the electric (3.12) and longitudinal (3.13) vector potentials, and keeping only the first term of the Bessel function expansion (3.8),

$$j_k(\omega r/c) \approx \frac{(\omega r/c)^k}{(2k+1)!!}\,, \qquad |\omega r/c| \ll 1\,, \tag{3.40}$$

gives, for the Babushkin gauge: $G_k = \sqrt{(k+1)/k}$, the Ek operator [120],

$$\Omega_q^{E,k}(\sqrt{(k+1)/k}) \approx \frac{\imath^k}{(2k-1)!!}\sqrt{\frac{k+1}{2k}}\left(\frac{\omega}{c}\right)^k r^k C_q^k \tag{3.41}$$

in the long-wavelength approximation. The Babushkin gauge is especially simple since the vector potentials components in (3.17) cancels[7] so that the operator is completely described by the scalar potential (3.6). A long-wavelength form for the Ek operator in the Coulomb gauge can be evaluated in a similar fashion.

The gauge-independent Mk operator (3.20) is completely specified by the magnetic vector potential (3.14). Keeping the first term in the Bessel expansion, gives,

$$\Omega_q^{M,k} \approx \frac{\imath^k}{(2k-1)!!}\left(\frac{\omega}{c}\right)^k r^k \boldsymbol{\alpha}\cdot\left[\boldsymbol{e}\otimes\mathbf{C}^k\right]_q^k \tag{3.42}$$

These approximate long-wavelength forms are used in some atomic structure codes, such as FAC [121], while others, such as GRASP2K [119], implement the full expressions for the operators (3.17) and (3.20) up to a certain cut-off in the bessel function expansion of the electromagnetic potentials. The present verison of GRASP2K performs the this expansion up to $(\omega r/c)^8$, after which the potentials are approximated by an asymptotic sinusoidal expression. The number of terms in the expansion and whether or not the subsequent sinusoidal expression is included, is determined by a specified convergence criteria.

3.8 SELECTION RULES

The representation of radiative transitions in terms of a multipole expansion over irreducible spherical tensor operators of definite ranks, allows for a direct prediction of whether or not a certain multipole transition Πk between two ASF's specified by $J_i^{\pi_i}$ and $J_j^{\pi_j}$, is allowed.

7 This is easily seen by noting that only the lowest-order in $\omega r/c$ is kept, so that the first term $\propto j_{k+1}$ in the electric and longitudinal vector potentials, (3.12) and (3.13), is omitted.

Table 3.1: Rigorous selection rules for radiative transitions $j \to i$ of multipole type Πk = E1, M1, E2, etc. between states coupled to a generic total angular momentum, J.

$\lvert\Delta_{ij}J\rvert$	=	$\lvert J_i - J_j\rvert \leqslant k \leqslant J_i + J_j \quad (\Rightarrow J_i = 0 \nrightarrow J_j = 0)$
$\Delta_{ij}M$	=	$M_i - M_j = q = -k, \ldots, k$
$\pi(Ek)$	=	$\pi_i\pi_j = (-1)^k$
$\pi(Mk)$	=	$\pi_i\pi_j = (-1)^{k+1}$

For the matrix element (3.22) to be non-vanishing, the ASF's have to satisfy certain relations depending on the parity of the transition operators discussed in Sec. 3.2. The matrix element vanishes if the parity of the total integrand, involving the left and right ASF's and the operator, is of odd parity since the integration is over all three-dimensional space. Multipole operators of magnetic type (3.20) have parity $(-1)^{k+1}$, while the the electric operators (3.17) have parity $(-1)^k$. This implies that, for the total transition integrand to be of even parity, the ASF's involved in an M1 transitions have to be of same parity, while for E1 transitions they have to differ, and so on.

Additional requirements on the involved total angular momenta can be obtained by investigation of the geometrical dependence of the total transition matrix element via the Wigner-Eckart theorem. For a general irreducible spherical tensor operator, $T^{(k)}_q$, of rank k and components q, we have the standard relation,

$$\begin{aligned}\left\langle \Gamma_i J_i^{\pi_i} M_i \middle| T^{(k)}_q \middle| \Gamma_j J_j^{\pi_j} M_j \right\rangle \\ = (-1)^{J_i - M_i} \begin{pmatrix} J_i & k & J_j \\ -M_i & q & M_j \end{pmatrix} \left\langle \Gamma_i J_i^{\pi_i} \middle|\middle| \mathbf{T}^{(k)} \middle|\middle| \Gamma_j J_j^{\pi_j} \right\rangle, \quad (3.43)\end{aligned}$$

from which it can be seen that the matrix element vanishes unless the 3j-symbol satisfies triangular relations in its upper- and lower-row arguments.

We summarize these results in a set of rigorous selection rules in Tab. 3.1. By rigorous we mean that these rules are valid independently on the underlying coupling mechanisms in the construction of the ASF's. As an example, for pure LSJ-coupled states, additional selection rules such as the well-known spin condition $\Delta S = 0$, applies. This selection rule is violated by the so-called *intercombination* transitions [122]. The long-wavelength form of the transition operators, (3.41) and (3.42), tells us that the total transition rate decreases with $(\omega\langle r\rangle/c)^2$ by increasing the multipole rank one step, say from E1 to E2, so that transitions of lowest possible k generally dominate the total transition rate from one state to another.

3.9 FORBIDDEN-LINE SPECTROSCOPY

The term *forbidden transitions* is often encountered. That a transition is "forbidden" does not mean that it do not occur at all, but simply that it is E1-forbidden. Such transitions occur at much lower rates in general, at least for low-Z systems. The importance of forbidden transitions increase rapidly with Z along an isoelectronic sequence, this is especially true if the transition connects two fine-structure levels belonging to the same term [35, Sec. 9.13].

Papers A_{III}, A_{IV}, A_V and A_{VI} concern the establishment of ground-state structures in highly ionized and heavy systems via a combination of atomic structure calculations and experiments using *only* forbidden transitions - thus termed *forbidden-line spectroscopy*.

As an example we show in Fig. 3.1 the energy structure of the 13 fine-structure states belonging to the ground-state configuration $4d^{10}\,4f^2$ of cadmium-like tungsten (W^{26+}, $Z = 74$) from paper A_V. The levels are denoted by their dominating component in LSJ-coupling from our MCDHF calculations and the solid (red) lines correspond to M1 emission lines observed in this work. Fig. 3.2 presents the spectra as recorded with the Shanghai-PermEBIT, an

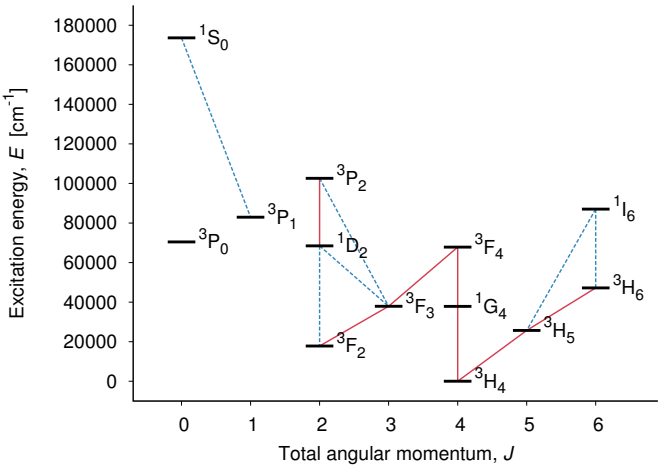

Figure 3.1: Energy-level structure of the 13 strongest M1 transitions within the $4f^2$ ground-state configuration of Cd-like W analyzed in paper AV.

electron-beam ion trap (EBIT), at electron beam energies of 780, 830, 880 and 1100 eV. The lines marked with 1, 2 and 4 are identified as the M1 transitions $^3F_4 \rightarrow {}^3F_3$, $^3F_4 \rightarrow {}^1G_4$ and $^3H_5 \rightarrow {}^3H_4$ respectively. The peak marked with 3 is from the W^{27} M1 transition $4f\,^2F_{7/2} \rightarrow 4f\,^2F_{5/2}$, which was analyzed in detail in the papers AIV and AVI and thus provides an accurate reference point for the present analysis. The line marked with 5 is due to a transition in N^+ from the residual gas in the *electron-beam ion trap* (EBIT). As can be seen from the solid red lines in Fig. 3.1, we manage to identify a total of seven forbidden transitions. See paper AV for further details on the calculations (i.e. correlation model) and the observation.

Whether or not the forbidden transitions within the ground-state configurations of tungsten ions can be used for plasma diagnostics in e.g. the ITER fusion device, remains to be seen. It is very likely that the decay properties of the states will be completely dominated by non-radiative collision processes. Nevertheless, the

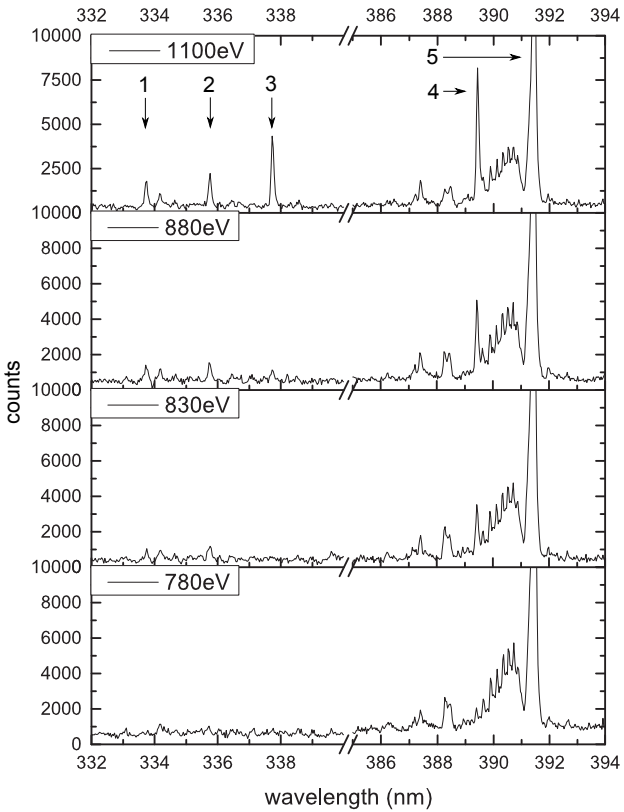

Figure 3.2: Spectra of Cd-like W from paper A_V recorded with the Shanghai-PermEBIT. Details are given in the text.

establishment of the ground term level structures of these complex ions opens up for studies of, e.g. XUV, decays from higher-lying states.

Another more exotic class of transitions are the so-called *unexpected transition*'s (UT's), which occur due to mixing of states induced by some symmetry-breaking perturbation, post the dominating Hamiltonian. These transitions do not have to be *forbidden*; the most important ones are actually of E1 type, but nevertheless unlikely to occur in general. The *unexpected transition* (UT)'s are central to the present work (papers B_{III} to B_{VIII}) and will be discussed further in Ch. 8.

States which only decay through forbidden or unexpected transition channels are often long-lived, or metastable, which makes them interesting and important for several reasons:

1. The fact that they decay through "exotic" radiative processes makes it possible to probe the atomic models more accurately and in new regions; for UT's related to external magnetic fields, hyperfine or parity-violating interactions (see for example Beiersdorfer et al. [123]).

2. They have been proposed to be used as atomic clocks and therefore it is essential to understand their decay properties in great detail (see for example Safronova et al. [45]).

3. They can be used to probe extremely low densities in astrophysical plasma, where even these low-probability, radiative transitions are visible but sensitive to collisional rates (see for example Brage et al. [124]).

The longest lifetime of an atomic state measured in a laboratory environment to date, and to the best knowledge of the author, is arguable of the first excited $1s2s\,^3S_1$ state of ^{4}He I which was determined to 7870 ± 510 sec by Hodgman et al. [125]. Another example is the lifetime of the metastable $3s3p\,^3P_2$ state in ^{24}Mg I which mainly decays through a forbidden M2 channel. The life-

time of this state was measured to 2050^{+140}_{-110} sec by Jensen et al. [126]. The longest lifetime ever measured in a negatively charged ion was recently determined by Bäckström et al. [127]. By using a electrostatic ion storage ring they found the radiative lifetime of the upper level in the $3p^5\,{}^2P_{1/2} \rightarrow 3p^5\,{}^2P_{3/2}$ M1 decay channel of $^{32}S^-$ to be 503 ± 54 sec.

Essentially all papers included in this thesis are in one way or another related to forbidden or unexpected radiative processes.

3.10 CHAPTER SUMMARY

In this chapter we have given an introduction to the rather complex theory of radiaitve multipole transitions, in a relativistic many-body framework. We defined basic radiative quantities such as the transition rate, relativistic line strength, lifetime, oscillator strength. Next we introduced the radiative transition operators as well as the associated transition amplitudes. The chapter was ended with a brief discussion about the long-wavelength form of the transition operators, radiative selection rules and a discussion about *forbidden-line spectroscopy* which is the central topic of papers A_I, A_{II}, A_{III} and A_{IV}.

4

ATOMIC STRUCTURE CALCULATIONS

The first implementation of the non-relativistic HF method into general-purpose codes to treat the bound-state atomic many-body problem were done in the late 1950's [128]. Today, numerous relativistic many-body methods exist, where *relativistic many-body perturbation theory*, *relativistic coupled cluster* (RCC), RCI and MCDHF, and more recently combined methods such as MR-RMBPT, or RCI and MCDHF calculations improved via perturbation theory, are among the most common and successful ones. All these methods have their own advantages and disadvantages, in short often related to the system at hand (e.g. number of valence electrons), what observables that are of interest, and, in relation to this, what sort of electron correlation the methods successfully capture.

Theoretical many-body methods which are exact within the chosen many-body basis, such as RCI and MCDHF, generally treat interactions between the valence electrons, i.e. the VVC defined in Sec. 2.11, efficiently. This is to a large extent related to the built-in treatment of static correlation by including strongly interacting CSF's in the multireference. The rapid scaling in the number of included basis states with respect to the size of the orbital basis of these methods does, however, imply that they often struggle with the inclusion of interactions between the valence and the core electrons, the CVC, and between the core-electrons themselves, the CCC. In contrast, perturbative methods such as RMBPT generally excel at treating systems with up to a few electrons outside a closed shell. The methods can often include dynamic correlation to convergence, but have problems with systems involving close degeneracies, i.e. systems with a large amount of static correlation, since

the perturbative scheme breaks down for these strong interactions.

Many efforts have been made to combine multireference techniques with perturbation theory in order to capture both static and dynamic electron correlation [34]. For our purposes, the MCDHF and RCI methods are conveniently combined with perturbation theory in the Brillouin-Wigner form (see e.g. Kotochigova et al.[129]). More details on this method are given shortly in the description of the GRASP2K program suite.

4.1 PUBLICLY AVAILABLE IMPLEMENTATIONS

Some of the above mentioned methods have been implemented in general atomic structure codes and made available to the scientific community, traditionally through program libraries such as the CPC-IPL [83] established already in 1969 at the Queen's University of Belfast, and today more and more through online open-source development platforms such as *GitHub* [130].

Examples of publicly available relativistic atomic structure codes are the CI-MBPT [131] and the GRASP2K [119] programs, both published and made available at the CPC-IPL [132, 133] and the FAC code [121] which recently has been converted to an open-access GitHub project, in its original form [134] as well as an actively developed C-based version [135] built around the *GNU Scientific Library* (GSL) [136]. Attempts are currently made to move the development of GRASP2K in the same direction. Another widely used implementation of the MCDHF method is the MCDFGME code [137], which is different from GRASP2K in that it is based on uncoupled basis functions (Slater determinants) instead of CSF's. Finally we mention the RATIP code [138] which functions as a set of tools based on GRASP2K wavefunctions to calculate e.g. continuum processes.

4.2 THE GRASP2K PROGRAM SUITE

GRASP2K is a very well established implementation of the MCDHF approach employing finite-difference numerical methods, in its original form developed by I. P. Grant and co-workers [101, 118, 119, 139–141] and currently maintained by *the Computational Atomic Structure group* (COMPAS) - an international collaboration between atomic theorists [142]. The GRASP2K program suite is a set of codes and tools for large-scale calculations of atomic structure and processes in the general case, that is, for in principle any atom or ion in the periodic table. This work is performed with the *development version* of these codes based on the latest published version [119] available from the CPC-IPL.

4.2.1 *Computational Procedure*

In short, the runtime procedure follows the scheme: Start by defining the CSF basis from an AS of Dirac orbitals with the included tools based on the active space approach described in Sec. 2.9. With the basis at hand, all spin-angular coefficients t^{rs}_{ab} and $v^{rs}_{abcd;k}$ in the expression for the interaction matrix, $\mathbf{H}$, (2.54) are calculated and stored on disk. The next step is to invoke the MCDHF procedure which essentially iterates the *CI-* and the *orbital-determination phase*, as described in Sec. 2.8.2. The first phase sets up $\mathbf{H}$ in the predefined CSF basis, by calculating the interaction integrals $I(a,b)$ and $R^k(ab,cd)$ from the radial orbitals, after which the secular equation (2.61) is solved for ASF eigenstates represented by the eigenvectors $\mathbf{c}$ with corresponding energy eigenvalues. The second phase generates radial Dirac spinors by solving the coupled MCDHF integro-differential equations (2.62).

With the variational principle as the backbone, the size of the orbital set, and thus the many-electron CSF basis set, is systematically enlarged until convergence of the atomic observables of in-

terest, such as excitation energies, transition rates or hyperfine parameters, is reached. The accuracy of a MCDHF calculation is essentially determined by whether the necessarily finite set of CSF's is effectively complete for the resulting ASF's to represent these physical observables. The completeness depends on the choice of correlation model, using e.g. the active space approach outlined earlier, but also on the optimization and constraints on the Dirac orbitals.

Finally, with a well-optimized orbital basis at hand, additional effects from the Breit interaction in Sec. 2.5.2 (fully retarded (2.21) or instantaneous (2.22)) and the one-loop radiative QED corrections explained in Sec. 2.5.4, can be included in the wavefunction through a subsequent RCI calculation. Such a last step is often also employed to account for further contributions from electron correlation by relaxing the constraints under which the CSF space is constructed from the set of one-electron orbitals obtained in the MCDHF procedure.

4.2.2 *The MCDHF Brillouin-Wigner Method*

The CSF space can be enlarged even further by using a Brillouin-Wigner perturbation theory approach [129]. The following example illustrates the method. Say you have an interaction matrix divided into three large blocks of different total angular momentum, J, and/or parity, π, between which there is no mixing and that you have reached the limit for the specific computational power or time you have access to. Additional correlation contributions can then be included via perturbation theory of Brillouin-Wigner type, by subdividing each J^π block into a zero-order space, containing the most important correlation contributions, and a first-order space within which no internal interaction is included (only diagonal elements). The CSF's belonging to this space is only allowed to interact with the CSF's in the zero-order space. An interaction matrix divided according to this scheme is illustrated in Fig. 4.1. Both

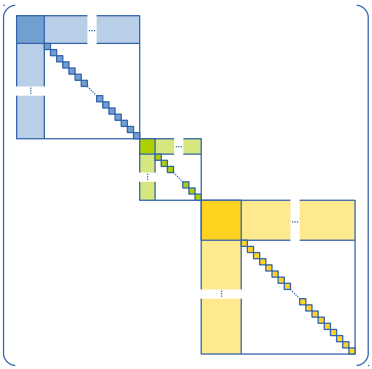

Figure 4.1: Illustration of an interaction matrix containing three independent blocks of different angular momentum and/or parity, each of which is further divided into a zero- and first-order space using a Brillouin-Wigner perturbation theory approach. This method is implemented in GRASP2K and used in many of the papers included in this thesis. See the text for more details.

of these spaces can be divided even further into different groups of CSF's, effectively representing different classes of many-body interaction. For this approach to be successful it is crucial to analyze the zero-order space in great detail - omission of important contributions could have large impact on final converged results.

This approach speeds up the MCDHF/RCI procedure substantially so that, in practice, millions of CSF's can be included for a certain J^{π} symmetry, which allows for an improved convergence of e.g. core-valence and core-core correlation effects, the latter which is of importance in calculations involving two-body operators weighted at small radii, such as the isotope shift [143].

Table 4.1: Theoretical and experimental prediction of the $4d^{10}\,4f\ {}^2F^o$ fine-structure separation in Ag-like W. The theoretical values are given as a function of the size of the active set AS#. The values are from our initial investigation of Ag-like W presented in paper A$_{VI}$.

Correlation Model	**Energy** [cm^{-1}]
DF	30 750
DF + Breit	29 239
DF + Breit + QED	29 239
AS1 ($n = 1,2\ldots,5$ and $l = s,p,\ldots,g$)	29 451
AS2 ($n = 1,2\ldots,6$ and $l = s,p,\ldots,h$)	29 533
AS3 ($n = 1,2\ldots,7$ and $l = s,p,\ldots,i$)	29 574
AS4 ($n = 1,2\ldots,8$ and $l = s,p,\ldots,i$)	29 593
AS5 ($n = 1,2\ldots,9$ and $l = s,p,\ldots,i$)	29 603
Experiment (SH-PermEBIT)	29 599.81 $\pm$ 2.28
Other theoretical work	
Safronova et al. (2010) RMBPT	29 550
Ivanova (2011) RMBPT	31 761
Ding et. al (2012) MCDHF	29 151

4.3 EVALUATION OF UNCERTAINTIES

The determination of reliable uncertainties is crucial for the produced data to be useful for the scientific community. Researchers in, say, stellar astronomy using atomic data (e.g. oscillator strengths) to simulate astrophysical plasmas, would not want to include data with error bars of more than a certain percentage, or even worse, data with no error bars at all. Many scientific journals now demand rigorous evaluation of uncertainties, which can prove quite challenging for theoretical models.

The accuracy of a multireference SCF calculation is judged from an analysis of the convergence trends of the atomic properties of in-

terest in different correlation models. As was described above, the convergence trends are functions of the size of the include orbital-basis and thus the size of the CSF expansion. In GRASP2K the calculations are performed in a *layer-by-layer* scheme, in which the AS of orbitals is enlarged systematically for a specific active space model. The previous layer of orbitals is kept fixed during the optimization procedure, and only the new ones are optimized.

The evaluation of actual uncertainties is a complex task in general and requires much experience with the methods. An clear example on how a convergence analysis can be carried out for energy separations, is taken from Paper A_{IV} and A_{VI} concerning Ag-like ions and the $4d^{10}\,4f\ {}^2F^o$ ground-term energy separation, observable through the forbidden M1 transition connecting the two states, just like Edléns coronal lines [23].

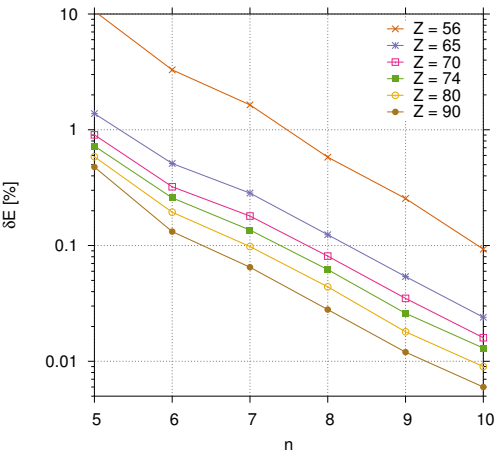

Figure 4.2: The relative convergence of the $4d^{10}\,4f\ {}^2F^o$ energy separation in Ag-like ions as function of the size of the active set of orbitals defined in Tab. 4.1 denoted by the maximum principal quantum number, n. δE is the difference in percentages of energy from the previous correlation layer. The presented values are from paper A_{IV} which included an additional correlation layer ($n_{max} = 10$, $l_{max} = i$).

We first note that one should always expect a smooth behavior of calculated physical properties along the isoelectronic sequence, as can be seen from the correlation energy trend shown in Fig. 2.5. Isoelectronic analyses in general provides a powerful tool in the evaluation of atomic data. The convergence of the ^{2}F energy separation with respect to the size of the active set, is visualized for a subset of Ag-like ions in 4.2. Within the present correlation model, it can be seen that the energy separation for high-Z ions is converged to less than 0.01% while low-Z ions reach 0.1%. Tab. 4.1 presents the convergence of the fine-structure separation as a function of active set size for the case of Ag-like W ion, as presented in paper A$_{VI}$. Including the final result of 29 619 cm^{-1} from the larger correlation model used for the isoelectronic sequence analysis in paper A$_{IV}$, it is clear that a very good agreement is found with experiment (within 0.1%).

A certain representation of uncertainties in theoretical transition data has been suggested by Fischer [144], and further discussed by Ekman et al. [145], to provide standardized measures for quality evaluation of such data sets.

4.4 CHAPTER SUMMARY

In this rather brief chapter, we discussed relativistic atomic structure calculations and advantages and disadvantages with respect to the treatment of electron correlation of various many-body methods. We connected this to publicly available codes, and in particular the GRASP2K implementation of the MCDHF and RCI methods, which has been used extensively in this work. The computational procedure of GRASP2K was summarized and we discussed how to enlarge the correlation models via Brillouin-Wigner perturbation theory. The chapter was ended with a brief discussion on the evaluation of convergence and uncertainties in atomic data sets.

5

HYPERFINE AND ZEEMAN PERTURBATIONS

This chapter deals with further refinements in our understanding of atomic spectra by including the symmetry-breaking effects arising from non-spherical interactions of the atomic electrons with a nuclei having non-zero nuclear spin - the *hyperfine interaction* - and interactions with a uniform external magnetic fields - the *Zeeman interaction*.

5.1 INTRODUCTION

In the previous chapter the atomic nucleus was treated as a spherical charge distribution, given by e.g. the Fermi distribution. It is however not uncommon for the nuclear charge distribution to be non-spherical, such that its charge-current density distribution will contribute non-spherical electromagnetic perturbations to the central Coulomb field. The resulting interactions with the electrons introduce a coupling between the the total electronic angular momentum $\mathbf{J}$ and the nuclear spin $\mathbf{I}$ to a new total angular momentum $\mathbf{F}$ for the *whole* atom, and split the energy spectrum into what is termed *hyperfine structure* (HFS). It was shown already in the late 19:th century that some fine structure levels were in fact split up into several closely spaced states, thus named hyperfine levels. In the 1920's Nagaoka et al. [146–148] studied the spectra of various isotopes and showed that the hyperfine effects were only present in some of them, from which they could that the hyperfine effects had to depend on the nucleus (see also Inamura [149] for a historical review of the work of Nagaoka). It was suggested by Pauli in

1924 that the nucleus has a total angular momentum, called nuclear spin, and that hyperfine effects in atomic spectra could be due to the magnetic interactions between the electrons and the nucleus [150]

Hyperfine interaction can be used to extract nuclear moments from experimentally determined hyperfine splittings, see e.g. the work of Bieroń et al. [151–155]. Or the other way around; available values for the nuclear moments opens up for tests of fundamental atomic structure theory, correlation studies or simulations of hyperfine-dependent atomic data in general to e.g. analyze stellar isotope abundances [156].

The perturbation of an external magnetic field **B** differs from the hyperfine interaction in it has a definite spatial direction. The external field vector couples to the total angular momenta, **J** or **F**, of the atomic system, breaks its rotational symmetry so that the magnetic sublevels, labeled by M_J or M_F, become non-degenerate. This results in the famous splitting of spectral lines, which was first discovered by P. Zeeman already in 1896 [157, 158];

> "*In consequence of my measurements of Kerr's magneto-optical phenomena, the thought occurred to me whether the period of the light emitted by a flame might be altered when the flame was acted upon by magnetic force. It has turned out that such an action really occurs.*"
>
> — P. Zeeman [157, p. 347]

In the same way as for the hyperfine interaction, the *Zeeman effect* can be used to extract information about the source of the perturbation, but with the magnetic field being the crucial parameter. The energy separation between two magnetic sublevels split by the Zeeman interaction is a function of the field strength, B, so that the Zeeman effect becomes a natural spectroscopic probe of magnetic fields in stellar atmospheres or laboratory plasma. An example is the discovery by Hale [28] that sunspots are magnetized which

was done through through observations of Zeeman splittings in the solar spectra, just ten years after the Zeeman effect was first observed.

A non-relativistic treatment of these perturbations is acceptable for the light elements, but for the general case it is better to apply relativistic theory, especially if one is to compare results along an isoelectronic sequence up to highly ionizes systems. This is particularly true for hyperfine interaction, which has strong dependence on the inner part of the wavefunction where the overlap with the nuclear charge distribution is largest. We saw in the previous chapter that the innermost s and $p_{1/2}$ electrons were greatly affected by relativistic contraction effects, which could have a large impact on the results from hyperfine structure calculations.

Contributions to the atomic energy spectrum from hyperfine interaction is in the most simple fashion included via the diagonal hyperfine A and B constants, and for the Zeeman interaction through Landé's g-factor in the familiar energy expression $\Delta E \approx g\mu_B BM$. If, however, the perturbations are of the same order as the involved energy separations in the gross model, then such a first-order treatment will break down and fail to predict the observables of interest. In these cases it becomes important to include off-diagonal hyperfine and/or Zeeman interaction matrix elements given by a total Hamiltonian $H = H_0 + H_{hfs} + H_{mag}$ where H_0 is the DC or DCB Hamiltonian with eigenfunctions given by the ASF's.

Off-diagonal interactions can have interesting effects on the radiative spectrum, such as additional energy shifts and *intensity redistributions* [159, 160] as-well as induction of otherwise strictly forbidden decay channels - termed *unexpected transition*'s (UT's). We will return to these effects in Ch. 7 and 8, and focus for now on the evaluation of the perturbed eigenstates and their radiative properties.

5.2 PERTURBED EIGENSTATES - THE PSF'S

An energy eigenstate including perturbation by either a nuclear field of higher multipole than electric monopole, an external magnetic field, or both, will be referred to as a *perturbed state function* (PSF). For our purposes these states are essentially represented by a linear expansion of ASF's $|\Gamma J^\pi M_J\rangle$ (2.51) of equal parity, π, obtained via the MCDHF method outlined in the previous chapter. For nuclei with non-zero nuclear spin, I, the basis is constructed from ASF's coupled to the nuclear ground state.

The eigenstates of an atomic system with zero nuclear spin under influence of an external magnetic field, are uniquely labeled by π and M_J. Systems with a non-zero nuclear spin are labeled by π, F and M_F in absence of an external magnetic field, and π and F otherwise. In some more detail, depending on the magnetic field strength, B, and the nuclear spin, I, PSF's of three classes should be considered:

$$\begin{array}{lcll} B \neq 0,\ I = 0 & & |\Lambda\pi M_J\rangle & = \sum_i d_i \left|\Gamma_i J_i^\pi M_J\right\rangle \\ B = 0,\ I \neq 0 & \rightarrow & |\Lambda\pi F M_F\rangle & = \sum_i d_i \left|(\Upsilon I, \Gamma_i J_i^\pi) F M_F\right\rangle \\ B \neq 0,\ I \neq 0 & & |\Lambda\pi M_F\rangle & = \sum_i d_i \left|(\Upsilon I, \Gamma_i J_i^\pi) F_i M_F\right\rangle \end{array} , \quad (5.1)$$

where Λ is a label introduced to uniquely specify the state. The M_J-dependent PSF's are simply constructed from an expansion over ASF's with the information about the angular momentum projection M_J kept. For the remaining two cases the PSF's are built from ASF's coupled to a *nuclear state function* (NSF) $|\Upsilon I M_I\rangle$ representing the ground state of a nucleus. The label Υ denotes additional information such as the proton number, Z, and the nuclear magnetic dipole and electric quadrupole moments, μ_I and Q respectively. To construct these coupled states, let

$$|\Upsilon I M_I, \Gamma J^\pi M_J\rangle = |\Upsilon I M_I\rangle \otimes |\Gamma J^\pi M_J\rangle$$

be simultaneous uncoupled eigenkets of the nuclear $\mathbf{I}^2$, I_z and electronic $\mathbf{J}^2$, J_z angular momentum operators, all of which obviously

commute with each other. Angular momentum coupled ASF-NSF basis states with definite total angular momentum quantum numbers, F and M_F, can then be formed through a standard unitary transformation,

$$\begin{aligned}\left|(\gamma I)FM_F\right\rangle &= \sum_{M_I,M_F} \left\langle IJ; M_I M_J \middle| IJ; FM_F\right\rangle \left|\gamma IM_I, \Gamma J^\pi M_J\right\rangle \\ &= \sum_{M_I,M_J} (-1)^{I-J+M_F}\sqrt{2F+1} \\ &\quad \times \begin{pmatrix} I & J & F \\ M_I & M_J & -M_F \end{pmatrix} \left|\gamma IM_I, \Gamma J^\pi M_J\right\rangle, \end{aligned} \tag{5.2}$$

where the Clebsch-Gordan coefficients $\left\langle IJ; M_I M_J \middle| IJ; FM_F\right\rangle$ are expressed in terms of Wigner's 3j-symbols in the second step. These basis states are simultaneous eigenkets of the mutually commuting operators $\mathbf{F}^2, \mathbf{I}^2, \mathbf{J}^2$ and F_z. Note that $[\mathbf{F}^2, J_z] \neq 0$ and $[\mathbf{F}^2, I_z] \neq 0$ even though $[\mathbf{F}^2, Fz] = 0$. Note also that the coupling order is important - in this work we use $(I, J)F$-coupling.

5.3 HYPERFINE STRUCTURE

The non-relativistic treatment of hyperfine effects in multiconfigurational methods is outlined in the book on MCHF theory by Fischer et al. [35, Ch. 8]. For the present relativistic presentation of hyperfine structure theory we rely on the one-electron formulation by Schwartz [161] and the generalization to many-electron systems given by Armstrong [162] and Lindgren and Rosén [163, 164].

The magnetic dipole moment of the nucleus can be related to its spin $\mathbf{I}$ through the nuclear g-factor, g_I,

$$\boldsymbol{\mu}_I = g_I \mu_N \mathbf{I}/\hbar, \quad \text{with } z\text{-projection}, \quad \mu_I = g_I \mu_N I_z/\hbar, \tag{5.3}$$

where g_I is positive if $\boldsymbol{\mu}_N$ lies along $\mathbf{I}$. The nuclear magneton μ_N

can be related to the Bohr magneton μ_B through the electron and proton masses, m_e and m_p,

$$\mu_N = \frac{e\hbar}{2m_p} = \frac{m_e}{m_p}\mu_B \approx 3.2 \times 10^{-8} \text{ eV T}^{-1} = 7.6 \text{ MHz T}^{-1}, \quad (5.4)$$

so that, $\mu_N = \mu_B/1836.15$, which implies that HFS is small compared to electronic fine structure separations in general.

An effective scalar Hamiltonian operator representing the hyperfine interactions can be obtained from a multipole expansion of the nuclear electromagnetic field [162, 163], where each term is formed from a tensor product of an electronic and nuclear tensor operator, which for equal-rank tensors as in this case is conveniently expressed as a scalar product [57, Ch. 11-8]

$$\begin{aligned} H_{hpf} &= \sum_k (-1)^k \sqrt{2k+1}\, \mathbf{V}_0^{(0)}(k) \qquad (5.5) \\ &= \sum_k (-1)^k \sqrt{2k+1} \left[\mathbf{T}^{(k)} \otimes \mathbf{M}^{(k)}\right]_0^{(0)} \\ &= \sum_k \sum_q (-1)^q T_{-q}^{(k)} M_q^{(k)} \equiv \sum_k \mathbf{T}^{(k)} \cdot \mathbf{M}^{(k)}, \end{aligned}$$

where $\mathbf{T}^{(k)}$ and $\mathbf{M}^{(k)}$ are spherical irreducible tensor operators of rank k acting in the spaces spanned by electronic $\left|\Gamma J^\pi M_J\right\rangle$ and nuclear states $\left|\Upsilon I M_I\right\rangle$, respectively. To illustrate why the scalar product of two irreducible tensor operators take this form, consider the $k = 1$ case which reduces to the regular scalar product of two Cartesian vectors [57, (11.42)],

$$\begin{aligned} \mathbf{T}^{(1)} \cdot \mathbf{M}^{(1)} &= -T_1^{(1)} M_{-1}^{(1)} + T_0^{(1)} M_0^{(1)} - T_{-1}^{(1)} M_1^{(1)} \\ &= T_x M_x + T_y M_y + T_z M_z \,. \end{aligned}$$

The absence of parity-violating effects means that the nucleus has no E1 moment, M2 moments, and so on, such that terms with even k represent the electric moments (Ek) while terms with odd k correspond to magnetic moments (Mk). In the present work we limit

the expansion to the M1 and E2 multipoles. Expressions for *electric octupole* (E3) and *magnetic hexadecapole* (M4) can be found in [161–164]. Note that the range of multipoles in the expansion is limited by the nuclear spin through $k \leqslant 2I$, such that the electromagnetic field of a nucleus with $I = 1/2$ only has an M1 component.

To construct the interaction matrix elements in the basis given for FM_F-dependent PSF's in (5.1), we note that hyperfine Hamiltonian (5.5) is a composite tensor operator built from a scalar product of two irreducible tensor operators acting on separate subspaces. This implies that one can decouple the nuclear and electronic parts of the matrix elements using Racah algebra techniques, with the result [57, Eq. (11.47)],

$$\begin{aligned}\left\langle (\Upsilon I, \Gamma_i J_i^\pi) F M_F \middle| \mathbf{T}^{(k)} \cdot \mathbf{M}^{(k)} \middle| (\Upsilon I, \Gamma_j J_j^\pi) F M_F \right\rangle \\ = (-1)^{I+J+F} \begin{Bmatrix} I & J_i & F \\ J_j & I & k \end{Bmatrix} \langle \Gamma_i J_i^\pi || \mathbf{T}^{(k)} || \Gamma_j J_j^\pi \rangle \langle \Upsilon I || \mathbf{M}^{(k)} || \Upsilon I \rangle,\end{aligned} \tag{5.6}$$

where we have used that the matrix element is diagonal in FM_F, that the nuclear space is spanned by the single ground state ket $|\Upsilon I\rangle$ and write the reduced elements in the Fano-Racah definition as usual. Note that the electronic matrix element only couples basis states which differ by at most k units of J.

The relativistic electronic M1 and E2 hyperfine operators can be expressed as sum of one-electron operators,

$$\text{M1)}\quad \mathbf{T}^{(1)} = \sum_l^N \mathbf{t}^{(1)}(l) = -\imath\sqrt{2}\alpha \sum_l^N r_l^{-2} \left(\boldsymbol{\alpha}_l \mathbf{C}^{(1)}(l)\right)^{(1)} \tag{5.7}$$

$$\text{E2)}\quad \mathbf{T}^{(2)} = \sum_l^N \mathbf{t}^{(2)}(l) = -\sum_l^N r_l^{-3} \mathbf{C}^{(2)}(l) \tag{5.8}$$

where the index l runs over all N electrons, α is the fine-structure constant, $\boldsymbol{\alpha}_l$ the Dirac matrix and $\mathbf{C}^{(k)}(l)$ re-normalized spherical harmonic operators acting on the coordinates of the l:th electron. All quantities are in Hartree atomic units as usual.

The reduced nuclear matrix elements in (5.6) are evaluated by association to the conventional nuclear magnetic dipole moment μ_I and electric quadrupole moment, Q,

$$\mu_I \equiv \langle \Upsilon I I | M_0^{(1)} | \Upsilon I I \rangle = \begin{pmatrix} I & 1 & I \\ -I & 0 & I \end{pmatrix} \langle \Upsilon I || \mathbf{M}^{(1)} || \Upsilon I \rangle \tag{5.9}$$

$$Q \equiv 2\langle \Upsilon I I | M_0^{(2)} | \Upsilon I I \rangle = \begin{pmatrix} I & 2 & I \\ -I & 0 & I \end{pmatrix} \langle \Upsilon I || \mathbf{M}^{(2)} || \Upsilon I \rangle \tag{5.10}$$

for maximum projection nuclear states, $|\Upsilon I\, M_I = I\rangle$, by definition. Analytical evaluation of the 3j-symbol [165] gives

$$\langle \Upsilon I || \mathbf{M}^{(1)} || \Upsilon I \rangle = \mu_I \sqrt{\frac{(I+1)(2I+1)}{I}} \tag{5.11}$$

$$\langle \Upsilon I || \mathbf{M}^{(2)} || \Upsilon I \rangle = Q \frac{1}{2} \sqrt{\frac{(I+1)(2I+1)(2I+3)}{I(2I-1)}}\,. \tag{5.12}$$

Tables with recommended values for μ_I and Q have been prepared and made available by the Nuclear Data Section of the IAEA, Vienna [166].

The fact that the hyperfine interaction correpsonds to a single-particle operator implies that it will only have a non-vanishing direct overlap between CSF's that differ by, at most, *single* substitutions. Particularly important important *single* substitutions for hyperfine interaction calculations, are those from the inner core shells, which represents what is called *spin* and *orbital polarization* [34, 35], which corresponds to deviations from the spherical symmetry of a core of closed subshells which normally would have no contribution to the hyperfine structure.

Even a very tiny fraction of CSF's describing spin and orbital polarization in the ASF wavefunction, can have a large impact on the hyperfine interaction matrix elements and thus the F-dependent energy spectrum. See Godefroid et al. [167, Sec. 3.1.1.] for an illustrative analysis in Chipmans' single-excitation picture [168] with just a few CSF's in the basis set .

5.4 EXTERNAL MAGNETIC FIELDS: FINE-STRUCTURE

The relativistic Zeeman interaction for an atomic system of zero nuclear spin in a homogeneous magnetic field, is given by a scalar product between the first M1 term of a multipole expansion of the electronic electromagnetic field[1], and the external magnetic field on tensor form $\mathbf{B}^{(1)} \equiv (0, B_z, 0)^\dagger$ [162, Ch. 6, Sec. 1] [171, Sec. B],

$$H_{mag} = \left(\mathbf{N}^{(1)} + \Delta\mathbf{N}^{(1)}\right) \cdot \mathbf{B}^{(1)} = \mathcal{N}^{(1)} \cdot \mathbf{B}^{(1)} = \mathcal{N}_0^{(1)} B_z \,, \quad (5.13)$$

where the many-electron operator can be decomposed into a sum over N one-electron terms,

$$\mathbf{N}^{(1)} = \sum_i^N \mathbf{n}^{(1)}(i) = -i\frac{1}{\sqrt{2}\,\alpha} \sum_i^N r_i \left(\boldsymbol{\alpha}_i \mathbf{C}^{(1)}(i)\right)^{(1)} \quad (5.14)$$

$$\Delta\mathbf{N}^{(1)} = \sum_i^N \mathbf{n}^{(1)}(i) = \mu_B \frac{g_s - 2}{2} \sum_i^N \beta_i \boldsymbol{\Sigma}_i \,, \quad (5.15)$$

where the second term $\Delta\mathbf{N}^{(1)}$ represents the QED correction due to the deviation of the electron g_s-factor from 2 [171, Eq. 18]. The index i runs over all N electrons, α is the fine-structure constant, $\boldsymbol{\alpha}_i$ the Dirac matrix (2.8), $\mathbf{C}^{(k)}(i)$ re-normalized spherical harmonic operators acting on the coordinates of the i:th electron, β is the the Dirac-β matrix (2.10) and $\boldsymbol{\Sigma}_i$ is the spin matrix

$$\boldsymbol{\Sigma}_i = \begin{pmatrix} \boldsymbol{\sigma} & 0_4 \\ 0_4 & \boldsymbol{\sigma} \end{pmatrix} \quad (5.16)$$

where $\boldsymbol{\sigma}$ is the Pauli matrix (2.9). Note the similarity between $\mathbf{N}^{(1)}$ and the electronic hyperfine M1 operator, $\mathbf{T}^{(1)}$ (5.7).

1 The $k = 2$ term in the multipole expansion, which is ignored here, is the so-called *diamagnetic term* [169, 170]

Eigenstates of the total Hamiltonian $H = H_0 + H_{mag}$ are represented in terms of PSF's of the form (5.1),

$$\left|\Lambda\pi M_J\right\rangle = \sum_i d_i \left|\Gamma_i J_i^\pi M_J\right\rangle , \tag{5.17}$$

which are definitely labeled by π and M_J. Interaction matrix elements between basis states in this representation can be determined from reduced matrix elements between ASF's,

$$\begin{aligned}\left\langle \Gamma_i J_i^\pi M_J \right| & \mathcal{N}_0^{(1)} B_z \left| \Gamma_j J_j^\pi M_J \right\rangle \\ &= B_z (-1)^{J_i - M_J} \begin{pmatrix} J_i & 1 & J_j \\ -M_J & 0 & M_J \end{pmatrix} \left\langle \Gamma_i J_i^\pi \right|\left| \mathcal{N}^{(1)} \right|\left| \Gamma_j J_j^\pi \right\rangle , \end{aligned} \tag{5.18}$$

where we have used that only the elements which are diagonal in π and M_J are non-zero.

5.5 EXTERNAL MAGNETIC FIELDS: HYPERFINE STRUCTURE

Atomic systems with non-zero nuclear spin under influence of an external magnetic field can represented by the total Hamiltonian,

$$H = H_0 + H_{hpf} + H_{mag} , \tag{5.19}$$

where H_{hpf} and H_{mag} are given by (5.13) and (5.5) respectively. The corresponding PSF eigensolutions (5.1) are of the type,

$$\left|\Lambda\pi M_F\right\rangle = \sum_i d_i \left|\left(\Upsilon I, \Gamma_i J_i^\pi\right) F_i M_F\right\rangle , \tag{5.20}$$

where M_F and π are the only two good quantum numbers. The matrix elements of the hyperfine operator, H_{hpf}, are diagonal in F and treated in the previous section. In the following we evaluate contributions from H_{mag} on isolated atomic systems with hyperfine structure.

In addition to the electronic interaction, the external magnetic field also couples to nuclear momenta such that the Zeeman interaction splits up into two parts,

$$H_{mag} = H^{J}_{mag} + H^{I}_{mag} \tag{5.21}$$

where the latter is the interaction between an external homogeneous magnetic field and the nuclear magnetic dipole moment $\boldsymbol{\mu}_I$ (5.3), which can be represented by,

$$H^{I}_{mag} = -\boldsymbol{\mu}_I^{(1)} \cdot \mathbf{B}^{(1)} = -\mu_0^{(1)} B_0^{(1)} = -g_I \mu_N I_0^{(1)} B_z \,. \tag{5.22}$$

The nuclear interaction is smaller than the electronic by a factor of $\mu_B/\mu_N = m_p/m_e \approx 1836$ which means that it should be negligible in most cases. This is however the only effect that separates two neighboring magnetic sub-levels belonging to states with a total electronic angular momentum J equal to zero, in which case it becomes important for interpretational reasons since it removes the degeneracy. The same is true for any case when the electronic Zeeman effect is zero, i.e. when the g_J factor is zero. It can also be of importance in situations requiring very high accuracy, such as in the level-crossing studies of ^{3}He (I = 1/2) by Wu and Drake [172].

5.5.1 *The Electronic Zeeman Effect*

The dominating electronic part of the Zeeman interaction on hyperfine states can be simplified considerably by decoupling the nuclear degrees of freedom, such that the interaction given by (5.13) can be written in terms of purely electronic reduced matrix elements according to [57, Eq. (11.39)],

$$\begin{aligned} &\left\langle (\Upsilon I, \Gamma_i J_i^{\pi}) F_i M_F \middle| H^{J}_{mag} \middle| (\Upsilon I, \Gamma_j J_j^{\pi}) F_j M_F \right\rangle \\ &\quad = (-1)^{I+J_j+2F_i-M_F+1} \sqrt{(2F_i+1)(2F_j+1)} \\ &\qquad \times \begin{pmatrix} F_i & 1 & F_j \\ -M_F & 0 & M_F \end{pmatrix} \begin{Bmatrix} I & J_i & F_i \\ 1 & F_j & J_j \end{Bmatrix} \left\langle \Gamma_i J_i^{\pi} \middle\| \mathfrak{N}^{(1)} \middle\| \Gamma_j J_j^{\pi} \right\rangle B_z \,, \end{aligned} \tag{5.23}$$

which is diagonal in π and M_F. Formally these matrix elements are diagonal also in I since the operator only acts at on electronic part of the wavefunction. This delta function is however left out since the current model is limited to a single nuclear ket representing the nuclear ground state, ΥI.

5.5.2 *The Nuclear Zeeman Effect*

The nuclear Zeeman effect can be evaluated in a similar manner as the electronic interaction[2] [57, Eq. (11.38)],

$$\begin{aligned}\left\langle (\Upsilon I,\Gamma_i J_i^\pi) F_i M_F \middle| H^I_{mag} \middle| (\Upsilon I,\Gamma_j J_j^\pi) F_j M_F \right\rangle \qquad (5.24)\\ = -\delta_{J_i J_j} (-1)^{I+J_i+F_i+F_j-M_F+1} \sqrt{(2F_i+1)(2F_j+1)}\\ \times \begin{pmatrix} F_i & 1 & F_j \\ -M_F & 0 & M_F \end{pmatrix} \begin{Bmatrix} I & J_i & F_i \\ F_j & 1 & I \end{Bmatrix} \left\langle \Upsilon I \middle|\middle| \mathbf{I}^{(1)} \middle|\middle| \Upsilon I \right\rangle g_I \mu_N B_z\,,\end{aligned}$$

where $g_I = \mu_I/I$ with μ_I in units of nuclear magnetons, μ_N. The reduced matrix element of the nuclear spin operator can be evaluated analytically according to, [57, Eq. (11.20)],

$$\left\langle \Upsilon I_i \middle|\middle| \mathbf{I}^{(1)} \middle|\middle| \Upsilon I_j \right\rangle = \delta_{I_i,I_j} \sqrt{(2I_i+1)(I_i+1)I_i}\,. \qquad (5.25)$$

5.6 MATRIX ELEMENTS

The evaluation of the hyperfine (5.6) and Zeeman matrix elements, (5.18) and (5.23), is essentially reduced to the determination of the electronic reduced matrix elements in the ASF representation (2.51). These are expressed as a linear combination of matrix ele-

2 Note that there is a distinct difference in that it now is the first angular momentum which is acted upon in the representation $(IJ)F$ which gives a slightly different expression for the decoupling compared to the electronic operator.

ments between CSF's which in turn can be decoupled into a sum over one-particle matrix elements,

$$\begin{aligned}\left\langle \Gamma_i J_i^\pi \middle|\middle| \mathbf{F}^{(k)} \middle|\middle| \Gamma_j J_j^\pi \right\rangle &= \sum_s^{n_{CSF}} \sum_r^{n_{CSF}} c_{ri} c_{sj} \left\langle \gamma_r J_r \middle|\middle| \mathbf{F}^{(k)} \middle|\middle| \gamma_s J_s \right\rangle \\ &= \sum_s^{n_{CSF}} \sum_r^{n_{CSF}} c_{ri} c_{sj} \sum_{ab} d_{ab;k} \left\langle n_a \kappa_a \middle|\middle| \mathbf{f}^{(k)} \middle|\middle| n_b \kappa_b \right\rangle , \quad (5.26)\end{aligned}$$

where the spin-angular coefficients $d_{ab;k}$ (which also include subshell occupation) are determined in the same fashion as in the MCDHF procedure described in Sec. 2.8.2, $\mathbf{f}^{(k)} = \mathbf{t}^{(k)}$ for hyperfine interaction and $\mathbf{f}^{(k)} = \mathbf{n}^{(k)}$ for interaction with external magnetic fields.

5.7 EVALUATION OF PSF EIGENSTATES

To simplify the present discussion, let $\Lambda_\alpha \Omega_\alpha$ and $\Gamma_i \Omega_\alpha$ act generic labels for any of the three possible PSF eigen- and basis states (5.1) respectively, where Ω denotes the appropriate "good" quantum number (M_J, F or M_F).

With the matrix elements in ASF representation at hand, it is possible to determine PSF eigenstates by setting up the interaction matrices in a representation of the basis (5.1) and solve the regular energy eigenvalue problem[3],

$$\left[(\mathbf{H}_0 + \mathbf{H}_1) - \mathcal{E}_\alpha \mathbf{1} \right] \mathbf{d}^\alpha = 0 , \quad (5.27)$$

where $\mathbf{H}_0 = \mathbf{H}^{DC}$ (2.12) (or $\mathbf{H}^{DCB}$) is diagonal, and the interaction matrices $\mathbf{H}_1 = \mathbf{H}_{hpf}$, $\mathbf{H}_{mag}$ or $\mathbf{H}_{hpf} + \mathbf{H}_{mag}$ depending on B and I. Or, alternatively, if the perturbations are weak enough in

3 It is clear from the indexes that the mixing coefficients d_i^α are different from the spin-angular coefficients $d_{ab;k}$, appearing in e.g. (5.26)

relation to the fine-structure separations, approximate PSF's can be determined to first order in the symmetry-breaking interaction,

$$\left|\Lambda_\alpha \Omega_\alpha\right\rangle^{(1)} = \left|\Gamma_0 \Omega_\alpha\right\rangle + \sum_i d_i^\alpha \left|\Gamma_i \Omega_\alpha\right\rangle, \tag{5.28}$$

where the sum runs over all basis states in the appropriate PSF expansion (5.1). The first-order coefficients are given by,

$$d_i^\alpha = \frac{\left\langle \Gamma_i \Omega_\alpha \middle| H_1 \middle| \Gamma_0 \Omega_\alpha \right\rangle}{E_0 - E_i}, \tag{5.29}$$

where E_0 and E_i are energies of the reference basis state and perturbing basis states (corresponding to the ASF eigenenergies) respectively.

Care has to be taken when deciding for an appropriate expansion such that no important contributions are left out. Depending on the physical quantity to be determined, a rough estimate can often be found by limiting the expansion to the perturbing states belonging to the same configuration as the reference state, or even just the same multiplet.

5.8 RADIATIVE TRANSITIONS BETWEEN PSF'S

When the symmetry-breaking perturbations due to an external magnetic field and/or hyperfine interaction, is applied, the ASF's mix and form new eigenstates, in our approach represented by the PSF's (5.1). The transition amplitude between two PSF's can be expressed as weighted linear combination of the transition matrix elements determined in the unperturbed regime. Using the generic

labels for the perturbed states introduced in the previous section, we can write the total radiative interaction matrix element as,

$$\begin{aligned}\left\langle \Lambda_\alpha \pi_\alpha \Omega_\alpha \right|\left| \widetilde{\mathbf{\Omega}}^{\Pi(k)}(\omega) \right|\left| \Lambda_\beta \pi_\beta \Omega_\beta \right\rangle \\ = \sum_{ij} d_i^\alpha d_j^\beta \left\langle \Gamma_i \pi_\alpha \Omega_\alpha \right|\left| \widetilde{\mathbf{\Omega}}^{\Pi(k)}(\omega) \right|\left| \Gamma_j \pi_\beta \Omega_\beta \right\rangle , \quad (5.30)\end{aligned}$$

for a transition of multipole Πk, where the mixing coefficients are determined through e.g. perturbation theory (5.29) or by solving the full eigenvalue problem (5.27). Note that additional decoupling of the nuclear degrees of freedom is necessary for atomic systems with non-zero nuclear spin.

This works well in the non-relativistic formalism[4] where the energy dependence ω/c can be factorized out and where the matrix element (5.30) can be expressed in terms of "unperturbed" matrix elements of the energy-independent operator, $\mathbf{O}^{\Pi(k)}$, used in e.g. the definition of the non-relativistic line strength (3.35).

In relativistic theory, however, we saw in Ch. 3 that the radiative transition rate (3.32) is constructed from matrix elements with complex dependencies on the photon energy through Bessel function expansions of the free-radiation fields. Formally we therefore have to evaluate all of the involved transition matrix elements on the right-hand side of (5.30) with the energy, ω, of the observed photon; and this has to be done for each of the transitions under investigation, which quickly becomes unpractical in general code implementations.

A convenient approach is to use the standard *non-relativistic* definition for the transition rate (3.36), but with the line strength (3.38) replaced by the weakly energy dependent *relativistic line strength* defined in (3.38). Equalizing the relativistic and non-relativistic ex-

4 Assuming that the effect of the free-radiation field on the wavefunction itself is small - if this does not apply, then one should include the radiation field on equal footing with the other perturbations via e.g. *radiation damping* methods.

pressions for the line strength, provides a definition of the appropriate transition operator,

$$O_q^{\Pi(k)}(\omega) \equiv \sqrt{\frac{2}{C_k}} \frac{1}{\sqrt{2k+1}} \left(\frac{\omega}{c}\right)^{-k} \widetilde{\Omega}_q^{\Pi(k)}(\omega)\,, \tag{5.31}$$

where the $(\omega/c)^{-k}$ factor cancels the lowest order energy dependence of the regular relativistic transition operator $\widetilde{\Omega}^{\Pi(k)}(\omega)$, given by (3.17) or (3.20) for Ek and Mk multipoles respectively. The k-dependent factor, C_k, is defined by (3.37).

For atomic systems with hyperfine structure in absence of an external magnetic field, the total transition rate is derived by noting that the radiative transition operators only act on the electronic coordinates so that the nuclear spin can be decoupled [57, Eq. (11.39)], leading to,

$$\begin{aligned} A^{\Pi k}&(\Lambda_\alpha \pi_\alpha F_\alpha, \Lambda_\beta \pi_\beta F_\beta) \qquad (5.32)\\ &= \frac{C_k}{g_{F_\beta}} \left(\frac{\omega}{c}\right)^{2k+1} \left| \langle \Lambda_\alpha \pi_\alpha F_\alpha || \mathbf{O}^{\Pi(k)}(\omega) || \Lambda_\beta \pi_\beta F_\beta \rangle \right|^2 \\ &= \frac{C_k}{g_{F_\beta}} \left(\frac{\omega}{c}\right)^{2k+1} \\ &\quad \times \left| \sum_{ij} d_i^\alpha d_j^\beta \langle \Gamma_i \pi_\alpha I J_i F_\alpha || \mathbf{O}^{\Pi(k)}(\omega) || \Gamma_j \pi_\beta I J_j F_\beta \rangle \right|^2 \\ &= \frac{C_k}{g_{F_\beta}} \left(\frac{\omega}{c}\right)^{2k+1} \left| \sum_{ij} d_i^\alpha d_j^\beta (-1)^{I+J_j+F_\alpha+k} \begin{Bmatrix} I & J_i & F_\alpha \\ k & F_\beta & J_j \end{Bmatrix} \right. \\ &\quad \left. \times \sqrt{(2F_\alpha+1)(2F_\beta+1)} \langle \Gamma_i \pi_\alpha J_i || \mathbf{O}^{\Pi(k)}(\omega) || \Gamma_j \pi_\beta J_j \rangle \right|^2 \end{aligned}$$

where $g_{F_\beta} = 2F_\beta + 1$ and where $\mathbf{O}^{\Pi(k)}(\omega)$ is defined by (5.31). Note how the dependence on ω/c is factored out. In the first step we insert the basis expansion (5.30), and in the second step we decouple the nuclear degrees of freedom to obtain matrix element in ASF representation.

When the atomic system is perturbed by an external magnetic field, one should remove the summation and averaging over magnetic sublevels used to construct the total transition rate. The expression for photon transitions between two magnetic sublevels is given by the *component transition rate*, $a^{\Pi(k)}_{\alpha\beta}$. For atomic systems with zero nuclear spin the component rate can be related to the reduced matrix elements in ASF representation through the Wigner-Eckart theorem,

$$
\begin{aligned}
&a^{\Pi k}(\Lambda_\alpha \pi_\alpha M_J^\alpha, \Lambda_\beta \pi_\beta M_J^\beta) \qquad (5.33)\\
&\quad = C_k \left(\frac{\omega}{c}\right)^{2k+1} \sum_{q=-k}^{k} \left| \sum_{ij} d_i^\alpha d_j^\beta \right.\\
&\qquad\qquad \left. \times \left\langle \Gamma_i \pi_\alpha J_i M_J^\alpha \middle| \mathbf{O}^{\Pi(k)}(\omega) \middle| \Gamma_j \pi_\beta J_j M_J^\beta \right\rangle \right|^2\\
&\quad = C_k \left(\frac{\omega}{c}\right)^{2k+1} \sum_{q=-k}^{k} \left| \sum_{ij} d_i^\alpha d_j^\beta (-1)^{J_i - M_i} \right.\\
&\qquad\qquad \left. \times \begin{pmatrix} J_i & k & J_j \\ -M_J^\alpha & q & M_J^\beta \end{pmatrix} \left\langle \Gamma_i \pi_\alpha J_i \middle\| \mathbf{O}^{\Pi(k)}(\omega) \middle\| \Gamma_j \pi_\beta J_j \right\rangle \right|^2 .
\end{aligned}
$$

If the atomic system has non-zero nuclear spin *and* is perturbed by an external magnetic field, additional decoupling of the nuclear angular momentum has to be employed in a similar fashion as in the evaluation of the hyperfine interaction matrix elements (5.6), so that

$$
\begin{aligned}
&a^{\Pi k}(\Lambda_\alpha \pi_\alpha M_F^\alpha, \Lambda_\beta \pi_\beta M_F^\beta)\\
&\quad = C_k \left(\frac{\omega}{c}\right)^{2k+1} \sum_{q=-k}^{k} \left| \sum_{ij} d_i^\alpha d_j^\beta \right.\\
&\qquad\qquad \left. \times \left\langle \Gamma_i \pi_\alpha I J_i F_i M_F^\alpha \middle| \mathbf{O}^{\Pi(k)}(\omega) \middle| \Gamma_j \pi_\beta I J_j F_j M_F^\beta \right\rangle \right|^2
\end{aligned}
$$

$$= C_k \left(\frac{\omega}{c}\right)^{2k+1} \sum_{q=-k}^{k} \left| \sum_{ij} d_i^{\alpha} d_j^{\beta} (-1)^{I+J_j+2F_i-M_F^{\alpha}+k} \right.$$
$$\times \sqrt{(2F_i+1)(2F_j+1)} \begin{pmatrix} F_i & k & F_j \\ -M_F^{\alpha} & q & M_F^{\beta} \end{pmatrix} \begin{Bmatrix} I & J_i & F_i \\ k & F_j & J_j \end{Bmatrix}$$
$$\left. \times \left\langle \Gamma_i \pi_{\alpha} J_i \middle|\middle| \mathbf{O}^{\Pi(k)}(\omega) \middle|\middle| \Gamma_j \pi_{\beta} J_j \right\rangle \right|^2 . \tag{5.34}$$

In all these three expressions, the indexes α and β describes preserved quantities forming "good" labels of the perturbed eigenstates, while i and j represents the basis states. For example, in the case when there is just hyperfine interaction (5.32), the F quantum number is indexed by α or β, while in the last expression (5.34) the additional perturbation from the external magnetic field introduces off-diagonal contributions in F so that it is denoted by the summation indexes i or j.

6 CODE DEVELOPMENT

Computer software is of fundamental importance to modern scientific research. A major part of the thesis work has been related to the improvement and development of scientific codes. As a member of the CompAS team [142] I have been taking part in the continuous development of the Grasp2k program suite which in its present form makes up about 335,000 rows of code. In addition, much of the theory and the new codes which have been developed over the years have materialized into a single code named Rhyze [173], used to calculate eigenstates and radiative transitions of any atom or ion in the periodic table perturbed by external magnetic fields and/or non-spherical nuclei in a basis constructed from relativistic MCDHF wavefunctions.

6.1 BASIC PROGRAMMING GUIDELINES

During the development of the scientific codes, and the Rhyze code in particular, it has been useful to adopt certain programming guidelines (see e.g. [174] for a review on good practices in scientific computing):

- Programs should be written *for people*, not computers. Make naming of variables, methods and modules consistent, distinctive, and meaningful. The code formatting should be consistent through out the project.
- *Let the computer do the work*. I.e. use available tools such as GNU Make [175] for compilation of the codes, or Gdb [176] for debug-

ging. Choose and comfortable with an advanced editor such as VIM[1] [177] or GNU EMACS [178].

- *Develop the code incrementally*. Try to work in as small steps as possible. Make use of a version control system, such as GIT [179], for everything that has been manually created by you (e.g. do not track files automatically generated during compilation).

- *Use unit tests*. Make it a habit to test features or results of a piece of code. Programs rely on such tests to prevent that a change to one part of the code does not break other parts. Unit tests are essential in large libraries and programs, but are usually not utilized for smaller projects. In the case of RHYZE, error messages should be handled by the intrinsic Fortran routine `error stop`, and follow a certain specified format:

```
error stop "main module name|procedure name: message"
```

- *Restric global datastructures to constants/parameters*. All variable datastructures should be sent as arguments to subroutines or functions to prevent e.g. accidental re-definitions.

- *Write the code in an object-oriented, or at least modularized, fashion*. Put related methods (subroutines and functions) into modules. In addition, it can be useful to define classes containing custom datastructures with member methods in a logical manner. As an example, the class in RHYZE which contains information about the eigenstates (the PSF's) and relevant methods, is declared as follows:

```
type eigenstates
   integer(ik)                  :: n      ! no of eigenstates
   character(len=1), allocatable :: p(:)   ! parity
   real(rk),         allocatable :: GQN(:) ! good quantum number
   integer(ik),      allocatable :: iE(:)  ! energy ordered index
   real(rk),         allocatable :: E(:)   ! eigenenergies
   real(rk),         allocatable :: w(:)   ! rad. decay width
   real(rk),         allocatable :: c(:,:) ! eigenvectors
```

1 If you are planning to work with the COMPAS team, you better learn VIM.

```
contains
   procedure, public  :: init_eigenstates
   procedure, public  :: kill_eigenstates
   procedure, public  :: calc_eigenstates
   procedure, private :: sort_eigenstates
   procedure, private :: define_eigenstates
end type eigenstates
```

The procedures (or methods) are subroutines or functions corresponding to operations one would like to perform on the set of PSF's. Fundamentally one would like to allocate all dynamic arrays, which is done by the `init_eigenstates` procedure, the `calc_eigenstates` procedure is a large routine for calculation of the eigenvectors and eigenenergies and the `sort_eigenstates` procedure sorts the states according to some specified parameters. In addition to these one could add procedures for printing information about quantum numbers and energies or for adding/removing a subsection of the set, and so on.

These are just a few general guidelines, in particular targeting scientific coding with modern Fortran, and many more could be added.

6.2 THE RHYZE CODE

The development of RHYZE [173] started from the Matlab® tools provided with the original HFSZEEMAN package developed by Andersson and Jönsson [180]. RHYZE is a general code written in modern object-oriented Fortran [181, 182] used to determine M_J-, For M_F-dependent eigenstates and corresponding radiative transitions of any multipole. The interaction matrices (hyperfine, Zeeman and radiative) are represented in terms of basis states built from J-dependent wavefunctions, obtained with GRASP2K, coupled to a nuclear wavefunction representing the nuclear ground state for atomic systems with non-zero nuclear spin. RHYZE essentially implements all of the theory presented in Ch. 5.

Comparatively little work as been done on hyperfine- and magnetic-field-induced spectral effects, and M_F-dependent effects in particular, which could be attributed to a lack of general-purpose tools. To resolve this, RHYZE was been developed with the general case in mind as a module to be used together with GRASP2K and HFSZEEMAN.

```
   ___      ___      ___      ___      ___
  /\  \    /\__\    /\__\    /\  \    /\  \
 /::\  \  /:/__/_  |::L__L  _\:\  \  /::\  \   A Relativistic HYperfine ZEeman
/::\:\__\/::\/\__\ |:::\__\/::::\__\/::\:\__\  code for calculation of F, MJ or
\;:::/  /\/\::/  / /:;;/__/\:::;/__/\:\:\/  /  MF dependent quantum mechanical
 |:\/__/   /:/  /  \/__/    \:\__\   \:\/  /   states and transition properites
  \|__|    \/__/             \/__/    \/__/    of atoms and ions.

RHYZE (c) 2016 Jon Grumer & the CompAS team     jon.grumer@teorfys.lu.se   v1.0
```

Basic Program Info: The code is written in modern Fortran (Fortran 2008) and consists of 4352 number of lines. The size of all integer, real and complex variables are defined by kind parameters from the intrinsic Fortran routine `iso_fortran_env`, and thus easily adopted to any required precision. By default most of the code makes use of 64-bit words as defined by the kind parameters `int64` and `real64`.

External Dependencies: GRASP2K [119], HFSZEEMAN [180] (an updated version is provided with RHYZE), LAPACK [183].

Availablilty: Currently via a GitHub [130] repository[2] together with an updated version of the original HFSZEEMAN code, or directly from the author. The code is planned to be submitted for publication in Computer Physics Communications.

Nature of Problem: Rigorous theoretical calculations of atomic

2 This repository is currently restricted to the members of the COMPAS collaboration [142] , ask the author for permissions if you need access. The plan is to eventually make this repository open.

properties for atoms or ions with or without nuclear spin under the influence of external magnetic fields, are of general interest in science and technology. RHYZE [173] has been developed with the aim of fully generalize the procedure of evaluation of hyperfine and/or magnetic-field perturbed eigenstates and associated transition rates and lifetimes in atoms or ions. Exotic spectral features such as intensity redistributions and unexpected transitions due to the perturbations, are of particular interest.

Solution Method: The starting point for the method is to represent the perturbed eigenstates in terms of the *perturbed state function*'s (PSF's) defined by (5.1). These are obtained through a CI model in which the eigenvalue problem (5.27) is solved in a basis of J-dependent ASF's, coupled to NSF's for cases with nonzero nuclear spin. The input set of ASF's are determined by the MCDHF+RCI approach with the GRASP2K program package, and the M1 and E2 hyperfine and M1 magnetic-field interaction matrix elements are calculated from the same set of ASF's with the HFSZEEMAN code [180]. The perturbed eigenstates can then be used to evaluate M_J-, F- or M_F-dependent transition rates of any multipole (E/Mk) according to (5.33), (5.32) or (5.34). The rates are determined from weakly energy dependent transition matrix elements, defined by the operator (5.31), calculated with the transition routines of GRASP2K, preferably using the same set of ASF's as for the calculation of the interaction matrices.

The perturbed eigenstates and transitions properties are evaluated using three different methods of increasing sophistication:

1. *Diagonal treatment* of the states in which there is no inclusion of mixing due to the magnetic-field or hyperfine perturbations - equivalent to A and B constants in the hyperfine case - and the transition rates are determined to first order as matrix elements between the eigenstates.

2. *Full diagonalization* of the magnetic-field and/or hyperfine interaction matrix to determine the perturbed eigenstates (mix-

ing between unperturbed states is included to all orders) and the transition rates are determined from matrix elements between the new eigenstates.

3. *Radiation damping* (under development) effects are included in the energy eigenvalue problem (5.27) through a complex non-local optical potential, as suggested by Robicheaux et al. [184]. In this method the perturbations and the interaction with the radiation field are treated on an equal footing, which is important for systems involving levels which have fine-structure separations and natural radiative widths of similar orders of magnitudes. The inclusion of effects due to the radiation field in the total interaction Hamiltonian results in a complex non-hermitian eigenvalue problem. Much of the basic structure have been implemented in RHYZE while the high-level routines remains to be written. A diagonal version of this method was employed by Indelicato et al. [185] and Marques et al. [186] to treat pure hyperfine interactions in He- and Be-like systems respectively. Later Johnson et al. [187] adopted Robicheaux' optical potential to treat also off-diagonal effects in He-like systems.

The diagonal method is useful to investigate the impact of off-diagonal matrix elements, and in comparisons with previous diagonal calculations.

Restrictions: The complexity of the cases that can be handled by RHYZE is essentially determined by the limitations of the GRASP2K package. In addition, for cases when the fine-structure separations are of the same order as the natural level widths the perturbative treatment of the radiation field breaks down and techniques such as the above mentioned radiation damping method should be adopted. The implementation of this method in RHYZE is ongoing. It should be made clear that there are no methods implemented in RHYZE to treat perturbations from external electric fields.

Installation: The compilation of the code is done through a Makefile by typing `make` in the command prompt while standing in the root directory of RHYZE. If successful, exectuables will be put in the created bin directory. A few things should be noted before proceeding with the actual installation:

1. Check the external library dependences. The code is dependent on LAPACK [183] for diagonalization, so make sure you have this libary installed. LAPACK is usually bundled with modern distributions of GNU/Linux [188], such as Ubuntu [189], CentOS [190] or OpenSuse [191], so this should not pose a problem for most users. It might be that the LAPACK libraries can not be located during the compilation even though you have them installed. In that case, either set up the correct linking manually, or it might help to install the LAPACK development package. E.g. for Debian-type distributions, such as Ubuntu, you just type `sudo apt-get install liblapack-dev` in the command prompt.

2. The compilation is performed with gcc/gfortran [192] per default. If you would like to use another compiler, please modify the Makefiles in the src sub-directories. Further instructions are found in this file.

3. The installation of HFSZEEMAN is dependent on some GRASP2K library routines, so make sure you have compiled these beforehand,

4. The installation may be cleaned up, i.e. remove redundant files, in a standard fashion by running `make clean`.

5. To completely clean up the installation, i.e. remove also the binaries and the bin folder, run instead `make cleanall`.

Input files: The following files are required to initiate a RHYZE calculation:

- `isodata` - Contains fundamental information about the nucleus

(I, μ, Q). Identical to the GRASP2K isodata file.

- `<name>.hzm` - One or more output files from HFSZEEMAN containing reduced Hyperfine and Zeeman interaction matrix elements as-well as information about the unperturbed basis states (the ASF's). If more than one file is included, then make sure that no state is duplicated. The ASF basis set and corresponding fine-structure energies provided in the top of the `.hzm` files are used by RHYZE to construct the perturbed basis set. The fine-structure energies given in these files can have a large impact on the final results and it is often a good idea to replace the ab-inito energies from the GRASP2K calculation with experimental energies when available.

  It is preferable to use the version of HFSZEEMAN included in this package since this version among other things provides higher accuracy for the matrix elements. If however the original version [180] from CPC-IPL is used, then make sure you run RHYZE with non-default options and select the Brink and Satchler definition for the reduced matrix elements. Additional non-default settings such as energy units used in the `.hzm` files can also be selected, which can be useful in the re-scaling from ab-initio to experimental fine-structure energies.

- `<case-id>.grasptransdata.rhyze.inp` - A file with concatenated GRASP2K transition files containing information about the unperturbed transitions - e.g. say that `file1` contains E1 and M2 transitions while `file2` contains M1 and E2 transitions, then create the input file to RHYZE by running the terminal command

  ```
  cat file1.ct file2.ct > <case-id>.grasptransdata.rhyze.inp
  ```

  The states involved in the transitions should match the states in the `.hzm` files. These have to be calculated using a modified version of the GRASP2K transition code which, in addition to the oscillator strength (gf), transition rate (A) and line strength (S), also prints the reduced transition matrix elements of the weakly

energy dependent operator (5.31), including the necessary phase information.

- `<case-id>.caseinfo.rhyze.inp` (optional) - input parameters which will be read automatically during the execution (see output files for additional info).

Note that `<name>` should be replaced by the label given to the files during the GRASP2K calculation, and `<case-id>` is a identifier defined while running RHYZE.

Output files: The following files are produced after a successful run of RHYZE:

- `<case-id>.asfdata.rhyze.out` - collected information about the unperturbed states (ASF's) to be used in the construction of the perturbed basis set, as well as hyperfine, zeeman and radiative transition interaction matrices in this representation.

- `<case-id>.caseinfo.rhyze.out` - input parameters given by the user, rename to `<case-id>.caseinfo.rhyze.inp` for the code to read this information automatically during the next execution.

- `<case-id>.eigenstates.rhyze.out` - information about the perturbed basis states and resulting eigenstates, including complete eigenvectors.

- `<case-id>.transitions.rhyze.out` (optional) - radiative transition data (transition energies, rates, lifetimes, widths).

- `<case-id>.fieldscan.rhyze.out` (optional) - scan of eigenenergy structure from the field-free limit up to the given magnetic field (to produce level-crossing diagrams and provide identification level crossings/anti-crossings).

6.3 RHYZE IN PRACTICE

RHYZE calculations including hyperfine interaction and/or an external magnetic field can result in hundreds or even thousands of eigenstates. To provide some insight in the complete calculational procedure, we start by considering the energy structure of the relatively simple example of the hyperfine structure of the $1s\,2p\,{}^3P$ excited states of ^{3}He, perturbed by an external magnetic field. After this we turn to the evaluation of radiative transition properties using the example of F-dependent states in He-like ^{19}F and M_J-dependent states in Ne-like Fe.

6.3.1 *Eigenstates and Structure*

^{3}He has a nuclear spin $I = 1/2$, a nuclear magnetic dipole moment $\mu_I = -2.127624\ \mu_N$, and thus no electric quadrupole moment ($Q = 0$ b) [166]. This results in 5 hyperfine states which will split up into a total of 18 magnetic sublevels in the presence of an external magnetic field.

For the purpose of this test calculation, relatively accurate ASF's are obtained from a three-block ($J = 0, 1$ and 2) single-reference ($1s\,2p$) CAS calculation, starting from a DHF model after which five subsequent layers of correlation orbitals are added in succeeding MCDHF calculations. For each layer only the new orbitals are varied. Note that both the $^3P_1$ and $^1P_1$ states are optimized in an EOL scheme. Details on the MCDHF procedure can be found in Sec. 2.8.2. The largest active set of orbitals is defined by,

$$\mathrm{AS} = \{1s\ldots7s,\ 2p\ldots7p,\ 3d\ldots7d,\ 4f\ldots8f,\ 5g\ldots9g,\ 6h\ldots10h\}$$

using a simplified non-relativistic nl notation (i.e. 2p denotes both $2p^+$ and $2p^-$). In LSJ-coupling, provided by a basis transformation

Table 6.1: Comparison of our energies of the ^{3}P hyperfine states in ^{3}He with the results of Johnson et al. [187]. The energies are given relative to the unperturbed $^3P_2$ level and we use the dominating LSJ-term to label the states.

Term	F	E_{RHYZE} [MHz]	E_{Johnson} [MHz]	Diff
"$^3P_2$"	5/2	-2137	-2152	15
"$^3P_1$"	3/2	-358	-372	14
"$^3P_2$"	1/2	4128	4138	-10
"$^3P_1$"	3/2	4778	4806	-28
"$^3P_0$"	1/2	32228	32232	-4

from jj-coupling with the `jj2lsj` program by Gaigalas et al. [193], the ASF's are given by the CSF expansions,

$$
\begin{aligned}
\left|\text{"1s 2p }^3\text{P" J}=0\right\rangle &= -0.998335\left|1s\,2p\,^3P_0\right\rangle \\
&\quad - 0.040643\left|1s\,3p\,^3P_0\right\rangle + 0.029508\left|1s\,4p\,^3P_0\right\rangle \ldots \\
\left|\text{"1s 2p }^3\text{P" J}=1\right\rangle &= +0.998334\left|1s\,2p\,^3P_1\right\rangle \\
&\quad + 0.040670\left|1s\,3p\,^3P_1\right\rangle - 0.029529\left|1s\,4p\,^3P_1\right\rangle \ldots \\
\left|\text{"1s 2p }^1\text{P" J}=1\right\rangle &= +0.997550\left|1s\,2p\,^1P_1\right\rangle \\
&\quad - 0.055064\left|1s\,3p\,^1P_1\right\rangle + 0.036304\left|1s\,4p\,^1P_1\right\rangle \ldots \\
\left|\text{"1s 2p }^3\text{P" J}=2\right\rangle &= +0.998334\left|1s\,2p\,^3P_2\right\rangle \\
&\quad + 0.040661\left|1s\,3p\,^3P_2\right\rangle - 0.029519\left|1s\,4p\,^3P_2\right\rangle \ldots
\end{aligned}
$$

where the quotation marks are used to clarify that e.g. "1s 2p ^{3}P" is just a label, here given by the dominating CSF component.

This set of ASF's is then used to determine the hyperfine and Zeeman interaction matrices through an updated version of HFSZEEMAN [180]. To provide a better comparison of the calculated perturbed energy structure with the accurate Hylleraas-type calculations of Wu and Drake [172], we use their fine-structure energies as input. This is easily done in a RHYZE calculation by replacing the ab-inito energies in the top of the `<name>-hzm` file(s). By default

```
 Number of ASFs
 3
iEJ  J   p    E [MHz]
 1  2.0  -    0.000000000E+00
 1  1.0  -    2.292163590E+03
 1  0.0  -    3.190883978E+04
Zeeman M1 reduced interaction matrix [a.u]
4.11098172112262E+00 -7.92349196336495E-01  0.00000000000000E+00
7.92349196336495E-01  1.83848487044697E+00  7.08700341369519E-01
0.00000000000000E+00 -7.08700341369519E-01  0.00000000000000E+00
Hyperfine M1 reduced interaction matrix [a.u]
2.11934007968182E-01 -1.21198605331839E-01  0.00000000000000E+00
1.21198605331839E-01  9.56088032198982E-02  1.07815420391209E-01
0.00000000000000E+00 -1.07815420391209E-01  0.00000000000000E+00
Hyperfine E2 reduced interaction matrix [a.u]
5.88012270121575E-02  6.66743404918974E-02 -4.44456762824776E-02
-6.66743404918973E-02 -3.84941911761749E-02  0.00000000000000E+00
-4.44456762824776E-02 -0.00000000000000E+00  0.00000000000000E+00
```

Figure 6.1: The `<name>.hzm` RHYZE input file for the ^{3}P states of ^{3}He with information about the included ASF basis set including energies, followed by the reduced Zeeman and hyperfine interaction matrices.

RHYZE assumes Hartree atomic units, but you can also provide the energies in cm^{-1} or MHz and choose the appropriate unit via the non-default options at runtime. In general, for accurate predictions of perturbed eigenstates and associated radiative properties, it can be advantageous to replace the ab-initio MCDHF energies from a GRASP2K calculation with experimental values. The `<name>.hzm` file for the $1s\,2p\ ^3P$ states of ^{3}He is shown in Fig. 6.1. In this file `iEJ` is an energy ordered index within the set of states with same J quantum number (here it is always equal to one since we limit the present calculation to $^3P_{0,1,2}$)

A M_J-, F or, as in this case, M_F-dependent set of basis states are constructed from the provided set of ASF's in the `<name>.hzm` file, the information about the nucleus given in the `isodata` file and the fact whether or not an external magnetic field is present, the strength of which is given at run time of RHYZE. Before moving

```
Basis states of the perturbed system
------------------------------------------------------------------------------
 id  iJ iEJ p   J    F   MF  Total ASF-energy [a.u]         Level [cm-1]
------------------------------------------------------------------------------
  1   1   1 -  2.0  2.5  2.5  0.00000000000000E+00               0.0000
  2   1   1 -  2.0  2.5  1.5  0.00000000000000E+00               0.0000
  3   1   1 -  2.0  1.5  1.5  0.00000000000000E+00               0.0000
  4   2   1 -  1.0  1.5  1.5  3.48369863601714E-07               0.0765
  5   1   1 -  2.0  2.5  0.5  0.00000000000000E+00               0.0000
  6   1   1 -  2.0  1.5  0.5  0.00000000000000E+00               0.0000
  7   2   1 -  1.0  1.5  0.5  3.48369863601714E-07               0.0765
  8   2   1 -  1.0  0.5  0.5  3.48369863601714E-07               0.0765
  9   3   1 -  0.0  0.5  0.5  4.84960070491632E-06               1.0644
 10   1   1 -  2.0  2.5 -0.5  0.00000000000000E+00               0.0000
 11   1   1 -  2.0  1.5 -0.5  0.00000000000000E+00               0.0000
 12   2   1 -  1.0  1.5 -0.5  3.48369863601714E-07               0.0765
 13   2   1 -  1.0  0.5 -0.5  3.48369863601714E-07               0.0765
 14   3   1 -  0.0  0.5 -0.5  4.84960070491632E-06               1.0644
 15   1   1 -  2.0  2.5 -1.5  0.00000000000000E+00               0.0000
 16   1   1 -  2.0  1.5 -1.5  0.00000000000000E+00               0.0000
 17   2   1 -  1.0  1.5 -1.5  3.48369863601714E-07               0.0765
 18   1   1 -  2.0  2.5 -2.5  0.00000000000000E+00               0.0000
```

Figure 6.2: The perturbed basis states for the $^3P_{0,1,2}$ states of ^{3}He set up by RHYZE, extracted from the `<case-id>.eigenstates.rhyze.out` file.

on to the inclusion of an external magnetic field, we compare the resulting hyperfine eigenenergies in the field-free limit with the accurate results of Johnson et al. [187]. It is clear from Tab. 6.1 that, even with this limited correlation model, the hyperfine structure is predicted to within 28 MHz (~ 0.00093 cm^{-1}).

Fig. 6.2 shows a list the M_F-dependent basis states as extracted from the `<case-id>.eigenstates.rhyze.out` file. The `id` index enumerates the basis states and are later used to identify the components in the eigenvectors, `iJ` is an index which connects the basis state to the corresponding ASF in the `<name>.hzm` file(s). The `Level` energies are relative to the lowest unperturbed energy ($^3P_2$ in this case) and the states are sorted into blocks with equal M_F quantum number.

From this set of basis states, RHYZE sets up the total interaction matrix including both hyperfine and Zeeman interactions (we use a magnetic field strength of $B = 1$ T). Diagonalization results in the eigenstates listed in Fig. 6.3, which is also provided in the `<case-id>.eigenstates.rhyze.out` file. Similar to the `iEJ` index of the basis states, `iE` is an energy ordered index within a block of states with equal M_F quantum number. The `Level` energies are given relative to the lowest unperturbed level just like before and `Diff` is the energy separation to the adjacent lower state. Note that the output has been slightly modified to fit in the present format. This output file also list the top three eigenvector components (only two are included in this extraction), where the `c`'s are mixing coefficients and the `id` index provides identification of the basis states in the list shown in Fig. 6.2. Complete eigenvectors are given in the end of the `<case-id>.eigenstates.rhyze.out` file.

6.3.2 *Level-Crossing Information*

In addition, RHYZE also has the optional feature of giving information about the variation of the energy levels with increasing magnetic field strength, starting from the field-free limit up to the strength given at runtime. The plots in Fig. 6.4 shows a *level crossing diagram*, which illustrates how the 2+2+1 hyperfine states of ^3P split up into 18 M_F-dependent sublevels and their dependence of the magnetic field strength. The upper plot shows a scan up to 10000 gauss while the lower plot is limited to the structure of $^3P_{1,2}$ in the region up to 2000 gauss. The level information between the parentheses is defined by the dominating eigenvector component at the maximum field strength (use the `c(1)` coefficient in Fig. 6.3 with the basis index, `id`, from Fig 6.2).

The points in B where the various sublevels cross provide an important test of atomic structure models in magnetic field environments. Tab. 6.2 presents a comparison between the level crossings from our calculation and the result of Wu and Drake [172]. Their

```
Eigenstates
-------------------------------------------------------------------------------
 Label       Eigenenergies          Level    Diff    Top eigenvector components
 iE   MF  p  Total [a.u]            [cm-1]   [MHz]   c(1)      id   c(2)      id
-------------------------------------------------------------------------------
  1  -2.5 - -6.71361429810649E-06 -1.4735           1.000E+00 18
  1  -1.5 - -6.10965449401825E-06 -1.3409  3973.86 -8.502E-01 16  -5.219E-01 15
  2  -1.5 - -4.42294280978807E-06 -0.9707 11098.03 -6.640E-01 15  -6.583E-01 17
  1  -0.5 - -3.82277398650742E-06 -0.8390  3948.92  5.697E-01 10   5.257E-01 11
  2  -0.5 - -1.97879315262595E-06 -0.4343 12132.81  5.795E-01 12  -5.200E-01 11
  3  -1.5 - -1.89557361275730E-06 -0.4160   547.56  7.495E-01 17  -5.353E-01 15
  3  -0.5 - -1.53795679851898E-06 -0.3375  2353.01 -5.505E-01 13   5.269E-01 10
  1   0.5 - -1.11079527386941E-06 -0.2438  2810.59  6.021E-01  5   6.002E-01  7
  2   0.5 -  9.0641354063764 2E-07  0.1989 13272.60 -5.894E-01  7   5.556E-01  5
  4  -0.5 -  1.14346063181049E-06  0.2510  1559.69 -5.533E-01 11   5.140E-01 10
  1   1.5 -  2.23870361223110E-06  0.4913  7206.35  7.299E-01  2   6.355E-01  4
  3   0.5 -  2.34233285105821E-06  0.5141   681.85 -6.183E-01  8  -5.907E-01  6
  2   1.5 -  4.12766201210881E-06  0.9059 11746.90  7.682E-01  4  -5.655E-01  2
  4   0.5 -  4.71217267500296E-06  1.0342  3845.90 -6.406E-01  8   5.497E-01  6
  5   0.5 -  5.41124797510566E-06  1.1876  4599.69  8.934E-01  9   3.882E-01  7
  5  -0.5 -  5.67985357742587E-06  1.2466  1767.34  9.212E-01 14   2.752E-01 12
  1   2.5 -  6.06397430572534E-06  1.3309  2527.39  1.000E+00  1
  3   1.5 -  6.75570383652871E-06  1.4827  4551.36  9.202E-01  3  -3.838E-01  2
```

Figure 6.3: Resulting eigenstates from a RHYZE calculation on the $^3P_{0,1,2}$ states of ^{3}He including hyperfine interaction and an external field strength of 1 T = 10000 gauss, extracted from the `<case-id>.eigenstates.rhyze.out` output file.

results differ from available experimental level crossings to within 0.15 gauss, and should therefore provide a very good benchmark. It is clear that there is a very good agreement between the results, and we also find one level-crossing which is not reported by Wu and Drake, that is crossing # 16 at 1244 gauss.

The differences between the results are attributed to their accurate representation of both correlation and the interaction matrix elements via the Hylleraas method, which is possible to use for few-electron atoms such as He. The present approach is designed for the general many-electron case, and as such one can not expect the results to compete with e.g. Hylleraas-type methods for few-electron systems. It should be noted that we use (J, F) labels

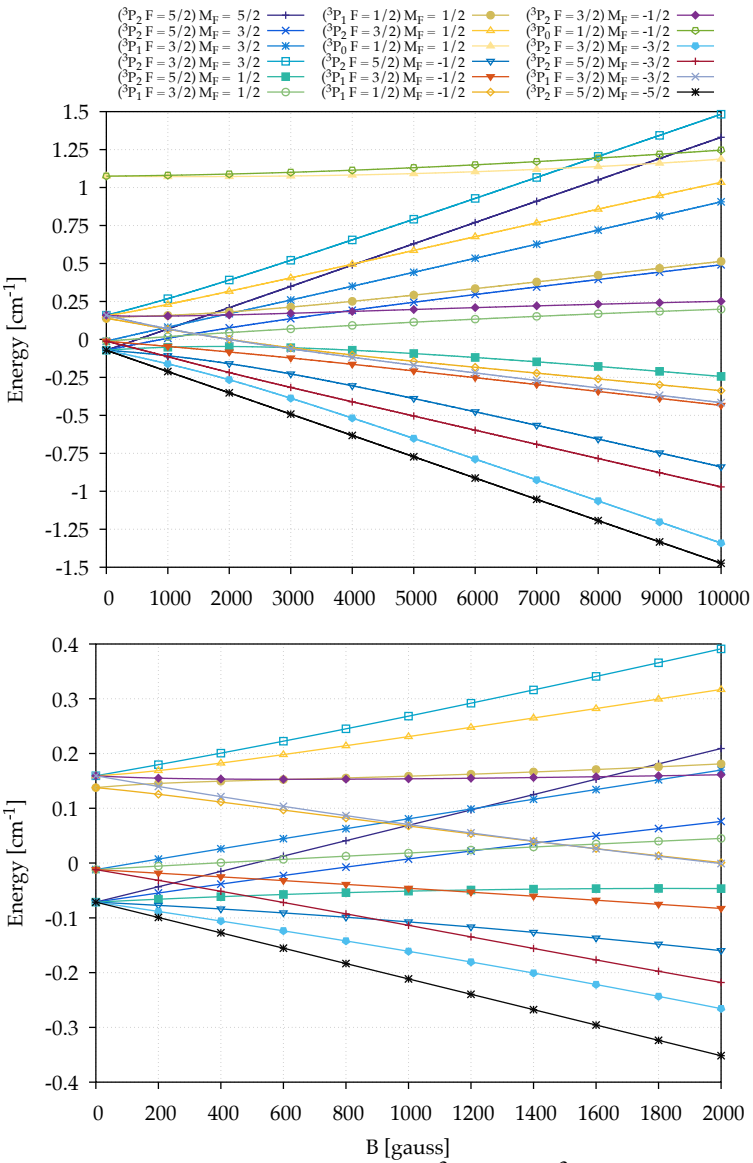

Figure 6.4: The hyperfine structure of $^3P_{0,1,2}$ in ^{3}He scanned from the field-free limit up to 10000 gauss in the upper plot. The lower plot is limited to the levels belonging to $^3P_{1,2}$ up to 2000 gauss.

defined by the dominating eigenvector components at maximum field strength, while Wu and Drake use the low-field limit labels. In addition, approaching levels with equal "good" quantum number will interact and push each other away; the point where the states would have coincided if they were non-interacting, are referred to as *anti-crossings*. We leave these results out for the present discussion.

6.3.3 *Transition Properties*

Finally we turn to the evaluation of transition properties between perturbed eigenstates. As a test example we use ^{19}F and compare the hyperfine-dependent transition properties of the $^3P_0$ state with the results of Johnson et al. [187]. A correlation model equal to the one for ^{3}He ise utilized to obtain the necessary ASF's. The ^{19}F isotope has a nuclear spin $I = 1/2$ and a nuclear magnetic dipole moment $\mu_I = 2.6289\ \mu_N$ [166]. For an easier comparison and to test the code we use the values for the hyperfine interaction matrix elements and fine-structure separations of the ^1P and ^3P states reported by Johnson. Starting with the energy structure, Tab. 6.3 shows the resulting hyperfine energies and it is clear that a good agreement is found.

To determine an accurate value for the transition rate of normally strictly forbidden E1 transition from $1s\,2p\ ^3P_0\ F = 1/2$ to the ground state $1s^2\ ^1S_0\ F = 1/2$, we note that is crucial to include interactions with the $^1P_1$ state. This state has a resonant E1 decay channel to the ground state, so that even a small admixture of this state in the total wavefunction can have a large impact on the resulting transition rate. GRASP2K transition calculations provides radiaitve interaction matrix elements (or line strengths if you like) for required set of multipoles (limited to E1 for now). The `<case-id>.grasptransdata.rhyze.inp` file is created acording to the description of the input files above. An extraction from the output file `<case-id>.transitions.rhyze.out` is presented in Fig. 6.5

Table 6.2: Comparison between the M_F-dependent level-crossings in ^{3}He obtained with RHYZE and the results of Wu and Drake [172]. The magnetic field strengths are given in units of gauss and we scan from the field-free limit up to up to 10000 gauss with a step size of 0.05 gauss. The level-crossings are obtained from linear interpolations. The # enumerates the crossings and the (J, F) labels are defined by the dominating eigenvector component at 10000 gauss as given in Fig. 6.3.

#	(J, F)	M_F		(J, F)	M_F	B_{RHYZE}	$B_{Wu\&Drake}$
1	(1, 1/2)	1/2	–	(1, 3/2)	-3/2	156	160.84
2	(2, 5/2)	5/2	–	(2, 5/2)	-3/2	249	249.26
3	(2, 5/2)	3/2	–	(2, 5/2)	-3/2	328	328.37
4	(2, 5/2)	5/2	–	(1, 3/2)	-1/2	343	343.10
5	(2, 5/2)	1/2	–	(2, 5/2)	-3/2	480	480.96
6	(2, 5/2)	3/2	–	(1, 3/2)	-1/2	518	518.28
7	(2, 5/2)	5/2	–	(1, 3/2)	1/2	544	544.79
8	(1, 1/2)	1/2	–	(2, 3/2)	-1/2	633	647.71
9	(2, 5/2)	-1/2	–	(2, 5/2)	-3/2	899	900.72
10	(1, 3/2)	3/2	–	(1, 1/2)	-1/2	919	925.31
11	(1, 3/2)	3/2	–	(1, 3/2)	-3/2	939	947.44
12	(2, 5/2)	5/2	–	(1, 1/2)	-1/2	994	998.99
13	(2, 5/2)	5/2	–	(1, 3/2)	-3/2	1007	1013.50
14	(2, 5/2)	1/2	–	(1, 3/2)	-1/2	1111	1111.98
15	(2, 5/2)	5/2	–	(1, 3/2)	3/2	1233	1233.58
16	(2, 5/2)	3/2	–	(1, 3/2)	1/2	1244	- - - - -
17	(2, 5/2)	3/2	–	(1, 1/2)	-1/2	1427	1434.06
18	(2, 5/2)	3/2	–	(1, 3/2)	-3/2	1430	1438.82
19	(1, 3/2)	1/2	–	(1, 1/2)	-1/2	1510	1520.68
20	(1, 3/2)	1/2	–	(1, 3/2)	-3/2	1511	1523.77
21	(1, 1/2)	-1/2	–	(1, 3/2)	-3/2	1524	1595.70
22	(2, 5/2)	5/2	–	(2, 3/2)	-1/2	1634	1644.20
23	(2, 5/2)	5/2	–	(1, 1/2)	1/2	1754	1763.79
24	(1, 3/2)	3/2	–	(2, 3/2)	-1/2	1892	1907.10
25	(1, 3/2)	3/2	–	(1, 1/2)	1/2	2187	2205.30
26	(2, 5/2)	1/2	–	(1, 3/2)	-3/2	2842	2859.49
27	(2, 5/2)	1/2	–	(1, 1/2)	-1/2	2988	3001.28
28	(2, 5/2)	3/2	–	(2, 3/2)	-1/2	3821	3841.22
29	(2, 5/2)	5/2	–	(2, 3/2)	1/2	4115	4137.72
30	(2, 3/2)	3/2	–	(0, 1/2)	1/2	7442	7436.79
31	(2, 3/2)	3/2	–	(0, 1/2)	-1/2	7906	7903.91
32	(2, 5/2)	5/2	–	(0, 1/2)	1/2	8742	8747.23
33	(2, 5/2)	5/2	–	(0, 1/2)	-1/2	9253	9262.14

```
Transition Rates
================

Multipole Type: E1
-------------------------------------------------------------------------------
  i  iE p    F     j  iE p    F      Energy[cm-]    <Fi||T||Fj>    A(i,j)
-------------------------------------------------------------------------------
  1   1 +   0.5    3   1 -   1.5     5.900756E+06   4.171642E-03   1.811105E+09
  1   1 +   0.5    4   2 -   1.5     5.901697E+06  -9.797182E-05   9.994008E+05
  1   1 +   0.5    5   3 -   1.5     5.951171E+06   2.285411E-01   5.576256E+12
  1   1 +   0.5    6   1 -   0.5     5.900599E+06   2.566778E-04   1.371203E+07
  1   1 +   0.5    7   2 -   0.5     5.900743E+06  -2.994333E-03   1.866194E+09
  1   1 +   0.5    8   3 -   0.5     5.951171E+06  -1.616020E-01   5.576186E+12
```

Figure 6.5: Extraction from the `<case-id>.transitions.rhyze.out` RHYZE output file, listing resulting E1 transition rates between the $1s\,2p\ ^{1,3}P$ and $1s^2\ ^1S$ hyperfine states in He-like $^{19}F^{+9}$. Note that a column giving the transition wavelengths has been removed from this extraction.

```
Multipole contribution printed for branching ratios (BR) > 1.0E-03
-------------------------------------------------------------------------------
  i  iE p    MJ   Level [cm-1]   Lifetime [s]   BR [Ek/Mk]-i(BR)
-------------------------------------------------------------------------------
  1   1 +   0.0   0.000000E+00
  2   1 -   2.0   5.849493E+06   5.385133E-06   M2-1(1.000)
  3   1 -   1.0   5.849492E+06   5.373705E-06   M2-1(0.998) E1-1(0.002)
  4   2 -   1.0   5.864761E+06   1.276162E-12   E1-1(1.000)
  5   3 -   1.0   5.961023E+06   1.542055E-12   E1-1(1.000)
  6   1 -   0.0   5.849490E+06   5.369913E-06   M2-1(0.997) E1-1(0.003)
  7   2 -   0.0   5.864760E+06   1.276170E-12   E1-1(1.000)
  8   3 -   0.0   5.951478E+06   4.899211E-05   M1-4(0.262) M1-7(0.262) ...
                                                   ... M1-11(0.262) E1-1(0.214)
  9   4 -   0.0   5.961022E+06   1.542045E-12   E1-1(1.000)
 10   1 -  -1.0   5.849488E+06   5.373723E-06   M2-1(0.998) E1-1(0.002)
 11   2 -  -1.0   5.864759E+06   1.276177E-12   E1-1(1.000)
 12   3 -  -1.0   5.961021E+06   1.542036E-12   E1-1(1.000)
 13   1 -  -2.0   5.849487E+06   5.385166E-06   M2-1(1.000)
```

Figure 6.6: Extraction from the `<case-id>.transitions.rhyze.out` RHYZE output file, listing eigenvalues, lifetimes and branching ratios for the $2s^2\,2p^6\ ^1S$ and $2s^2\,2p^5\,3s\ ^{1,3}P$ states of Ne-like Fe under the perturbation of an external magnetic field at 2.5 T. The extraction has been slightly modified to fit the present format.

Table 6.3: Comparison of our energies of the ^3P hyperfine states in $^{19}F^{+9}$ with the results of Johnson et al. [187]. The energies are given relative to the unperturbed $^3P_0$ level and we use the dominating LSJ-term to label the states.

Term	F	E_{RHYZE} [cm^{-1}]	$E_{Johnson}$ [cm^{-1}]	Diff
"$^3P_0$"	1/2	-0.86	-0.87	0.01
"$^3P_1$"	1/2	143.28	143.22	0.06
"$^3P_1$"	3/2	155.64	155.66	-0.02
"$^3P_2$"	3/2	1096.94	1096.82	0.12
"$^3P_2$"	5/2	1117.39	1117.42	-0.03

which shows the resulting transition properties as determined by RHYZE. The $^3P_0$ $F = 1/2$ state is the lowest lying state with $F = 1/2$ so that its identifier is given by `"iE p F" = "1 - 0.5"` and the resulting transition rate is 1.37×10^7 s^{-1}, which agrees well with the value of 1.39×10^7 s^{-1} reported by Johnson et al. [187]. We clarify again that these are smaller test calculations, and that a closer agreement would be expected for large-scale calculations.

The `<case-id>.transitions.rhyze.out` file from a RHYZE calculation also gives the total lifetime of the perturbed eigenstates and branching ratios, including all possible transition channels; limited only by the content in the `<case-id>.grasptransdata.rhyze.out` file and the included ASF's in the `<name>.hzm` files. Fig. 6.6 shows an example from a test calculation on the $2s^2\ 2p^6\ ^1S$ and $2s^2\ 2p^5\ 3s\ ^{1,3}P$ states of Ne-like Fe under the perturbation of an external magnetic field at 2.5 T. The radiative decay of the $^3P_0$ state is normally dominated by an M1 transition to the $^3P_1$ state, but the introduction of the external magnetic field causes the $^3P_0$ state to mix with the $^{1,3}P_1$ states which opens up an additional E1 channel. This is clear from the branching ratios of the $^3P_0$ $M_J = 0$ state (`i = 8`) in Fig. 6.6, which shows a ratio of 21% for the E1 decay to the ground state (`i = 1`).

7

SPECTRAL INTENSITY REDISTRIBUTIONS

In this chapter we discuss effects on radiative spectra due to perturbations from the symmetry-breaking interactions outlined in Ch. 5, with a focus on pure hyperfine interaction. The diagonal part of the perturbation gives the well known hyperfine spectral features. The effect of the off-diagonal part of the perturbation is often small, but can in some cases shift line positions and introduce intensity redistributions among the hyperfine components in what is termed *hyperfine-induced intensity redistributions*. Although the present work only consider such effects for the case of pure hyperfine perturbations, an external magnetic field could just as well induce similar effects.

Two papers included in this work directly address hyperfine-induced intensity redistributions in atomic spectra. In paper B_I we analyze the hyperfine structure and resulting spectra of In II in detail and compare with high-resolution laboratory spectra [194]. During this work, codes and methods were developed which ultimately lead to the RHYZE program presented in Ch. 6. Paper B_{II} concerns the more complex system of Mn I and the impact of an accurate treatment of hyperfine interaction on abundance analyses in stars, which is illustrated by stellar atmosphere modeling with and without off-diagonal effects. Results from these papers will be briefly discussed in the following after a general introduction.

7.1 INTRODUCTION

The determination of chemical abundances and many other quantities in astrophysics, rely upon laboratory measurements and theoretical calculations of atomic properties, mainly wavelengths and oscillator strengths. Precise knowledge of the wavelengths is of fundamental importance for the identification of features in stellar spectra in general, and of faint lines in particular.

It is often satisfactory to consider unperturbed atomic systems described by fine-structure states, i.e. excluding broadening effects (or splittings depending on the spectral resolution) and energy shifts due to perturbations from e.g. hyperfine interaction and external magnetic fields. Paper A_{II}, which concerns calculations of spectroscopic data for the astrophysically important Te V ion, represents such an example.

However, it has been shown, for example in 1952 by Abt [195] in a study of the solar spectrum, that *hyperfine interaction* can have a significant impact on the measured linewidths and wavelengths, leading to erroneous spectral identifications as-well as inaccurate derivations of abundances and turbulent velocities. The resolution of solar, stellar, and interstellar observations is now in general high enough for isotope and hyperfine effects to be important to consider [156, 196].

The impact of hyperfine interaction on atomic spectra can be described by the hyperfine A and B parameters, corresponding to diagonal M1 and E2 hyperfine interaction matrix elements (5.6) respectively. This representation is a good approximation if the splitting of the fine structure levels is much larger than the hyperfine separations. The parameters can be determined from ab-inito calculations, but also from a fit of the line profiles, assuming a Doppler lineshape and theoretical relative intensities, to an observed high-resolution spectrum [194, 197].

If however the perturbation from the hyperfine interaction is of the same order as the fine-structure separations, it could introduce interference effects among hyperfine states "belonging" to different fine-structure states which then will share their decay properties. The resulting intensity redistrubutions in the radiative spectrum can be large, which was illustrated by e.g. Aboussaïd et al. for the $3d^2 4s - 3d4s4p$ transitions in Sc I [198]. In addition, completely *new* decay channels, called *unexpected transition*'s, could be opened [199]. We will return to the topic of UT's in Ch. 8 (see also paper B_{VI} for an overview). Off-diagonal contributions typically affect transitions involving eigenstates with orbitals of high n and l, which gives small fine-structure separations, as well as open s subshells, which has shown to give large contributions from hyperfine interaction due spin-polarization effects [167].

Hyperfine-induced intensity redistributions in atomic spectra has been studied earlier by Andersson and Jönsson who carried out a theoretical MCDHF-based investigation of the radiative transitions between the hyperfine levels of $4s4f\,^3F_{2,3}$ and $4s4d\,^3D_2$ in Ga II [159]. The obtained theoretical spectra were compared to experimental Fourier transform spectra showing good agreements, which showed the importance of hyperfine-induced interference effects for the $4s4d\,^3D_2 - 4s4f\,^3F_2$ transitions. A similar study was performed for Al II [160], where it was shown that a description of the hyperfine structure with only the diagonal A and B constants is not sufficient for a large number of transitions.

7.2 HYPERFINE-INDUCED REDISTRIBUTIONS IN INDIUM

In 2001 Karlsson and Litzén [194] investigated the hyperfine structure of singly ionized indium (In II) by using a Fourier transform spectrometer in an attempt to experimentally determine A and B hyperfine constants, which failed for the $5s5d\,^3D_2 - 5s4f\,^3F_{2,3}$ transitions. The open s shell together with the high nl of the other valence electron, indicate that this could be attributed to off-diagon-

al effects. In II might not be the most interesting ion in terms of applications, but, together with the detailed experimental spectra of Karlsson and Litzén, it makes up an excellent model system for investigating off-diagonal hyperfine interaction and provides a excellent laboratory for the development of general methods. This work was the starting point for the methodology which eventually was implemented in the RHYZE code outline in Ch. 6. Paper B_I presents a detailed analysis of this system.

It turns out that it is hard to determine accurate values of the diagonal matrix elements of the magnetic dipole hyperfine interaction from ab-initio wavefunctions, represented by the hyperfine constants $A(\text{"}^3\text{F"}_3)$ and $A(\text{"}^1\text{F"}_3)$ (where the LS term is used as a label for the fine-structure states). The latter constant is important

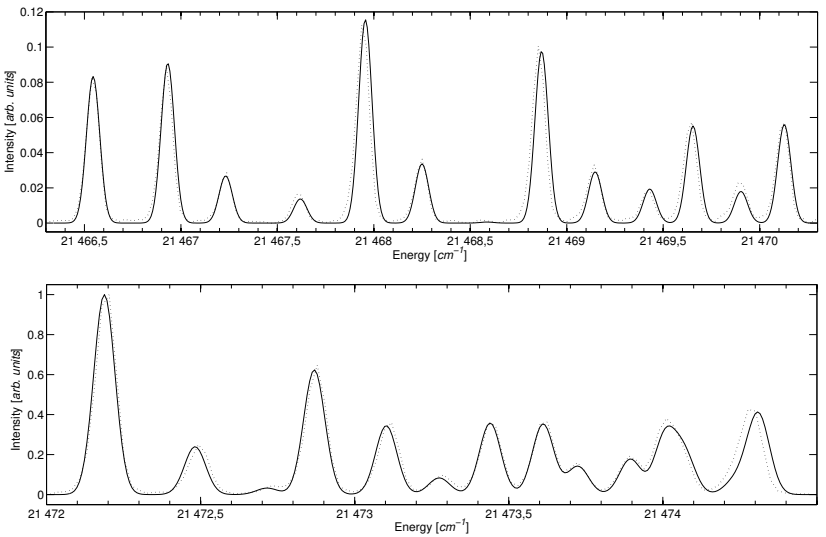

Figure 7.1: Comparison of our *adjusted* synthetic spectrum (solid lines) with the observed spectrum of In II by Karlsson and Litzén [194] (dotted lines). The upper panel shows $5s5d\,^3D_2 - 5s4f\,^3F_2$ and the lower the $5s4f\,^3F_3$ transitions. See the text and paper B_I for details.

since the interaction with $"^1F"_3$ comes in as an off-diagonal effect when evaluating the hyperfine eigenstates and decay properties of the ^3F states. A comparison with available experimental values [194] shows that our ab-inito value for $A("^1F"_3)$ is significantly too low. The sum of $A("^3F"_3)$ and $A("^1F"_3)$ does however converge just as nicely as the other two constants, $A("^3F"_2)$ and $A("^3F"_4)$. The underlying reason to all this is that the values of $A("^3F"_3)$ and $A("^1F"_3)$ are sensitive to the mixing coefficients of the $5s4f\,^1F_3$ and $5s4f\,^1F_3$ CSF's in the ASF's describing the $"5s4f\,^3F"_3$ and $"5s4f\,^1F"_3$ eigenstates, i.e. it is very hard to determine the fine-structure separations accurate enough to predict the hyperfine structure. If possible, one should use experimental values for the J-dependent energies.

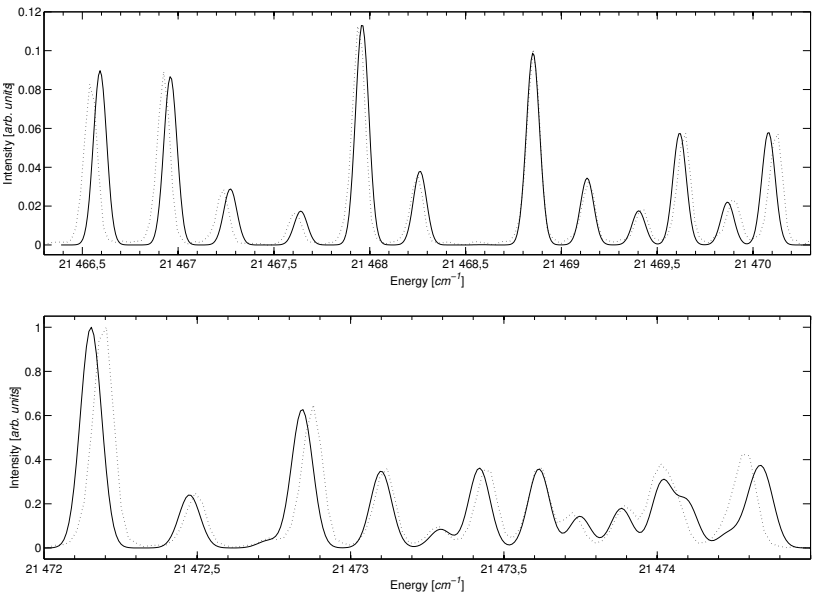

Figure 7.2: Comparison of our *ab-initio* synthetic spectrum (solid lines) with the observed spectrum of In II by Karlsson and Litzén [194] (dotted lines). The upper panel shows $5s5d\,^3D_2 - 5s4f\,^3F_2$ and the lower the $5s4f\,^3F_3$ transitions. See the text and paper B_1 for details.

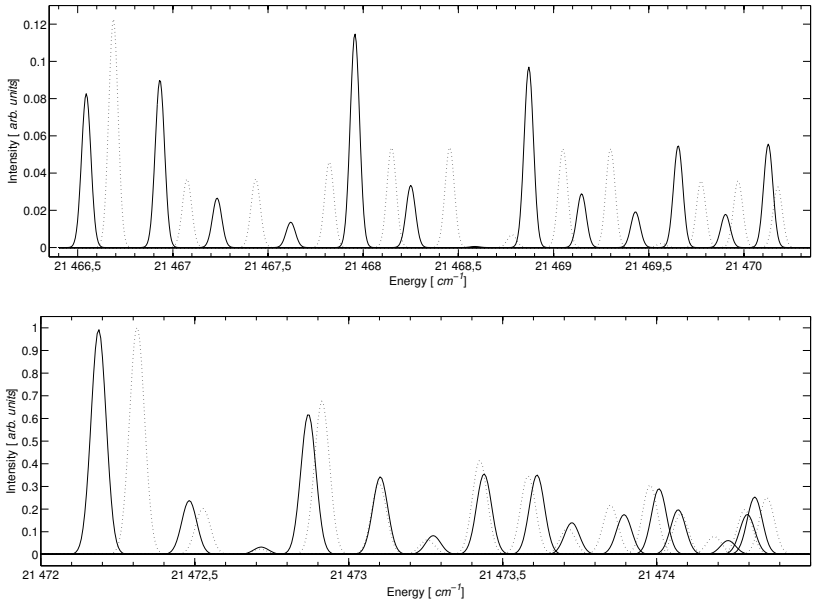

Figure 7.3: The synthetic spectral components due to the $5s5d\,^3D_2 - 5s4f\,^3F_2$ (upper panel) and $5s4f\,^3F_3$ transitions (lower panel) of In II, generated via a *diagonal* (dotted lines) and a complete matrix approach (solid lines). See the text and paper B_I for details.

To obtain better expansion coefficients for the CSF's of the two $J = 3$ ASF's, we employ a semi-empirical fitting of some of the M1 hyperfine interaction matrix elements. We start with a re-scaling of all the diagonal elements of the $J = 3$ states by using the experimental value for $A("^1F"_3)$. This changes the wave functions of the states of interest which makes it possible to also shift the off-diagonal elements. In a third and final step we re-scale the matrix elements of the lower $5s5d\,^3D_2$ state as well, even though this has much less impact on the spectrum. See Sec. 5.1 of paper B_I for details on the adjustment procedure.

The final synthetic and semi-empirically *adjusted* spectrum is shown in Fig. 7.1 where it is compared with the observed spectrum of

Karlsson and Litzén. Based on this investigation it was realized that an enlarged correlation model had to be used to determine the ASF's. A completely *ab-initio* spectrum (except for minor scaling of the transition energy to align the experimental and synthetic lines) is presented in Fig. 7.2. Both the adjusted and fully ab-initio results show an excellent agreement with the experiment.

The importance of including off-diagonal effects in the treatment of this system is further illustrated in Fig. 7.3. These plots show a comparison between spectral distributions generated from a simple diagonal approach (corresponding to using the hyperfine A and B parameters) and complete diagonalization; it is clear that the impact from the off-diagonal elements is significant. The calculated transition properties, which are tabulated in the paper, reveal that an inclusion of off-diagonal hyperfine interaction reduces some of the oscillator strengths by two orders of magnitude, while others are increased by up to more than a factor of 6.

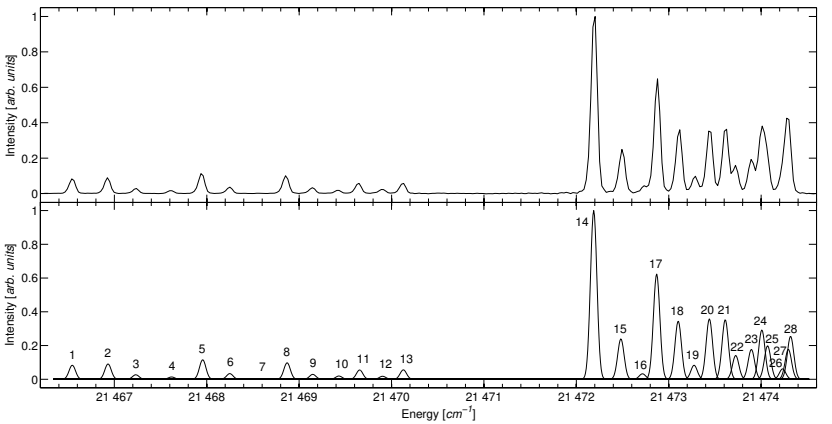

Figure 7.4: The observed spectrum due to the $5s5d\,{}^3D_2 - 5s4f\,{}^3F_{2,3}$ hyperfine transitions of In II by Karlsson and Litzén [194] (upper plot), compared to our synthetic spectrum (lower plot) for line-identification purposes. Note that each of the synthetic lines are plotted separately. See paper B_I for a table with labels of the enumerated lines.

Finally, we mentioned in the introduction to this chapter the problem of inaccurate spectral identifications if hyperfine interactions are not correctly accounted for in atomic spectra. In Fig. 7.4 we illustrate how a synthetically generated spectrum can be used to identify hyperfine components; particularly in the case of overlapping lines, as can be seen from the spectral features in the right part of the plot.

7.3 MANGANESE IN STELLAR ATMOSPHERES

Chemically peculiar stars are stars which have distinctly unusual metal abundances. Jomaron et al. [200] estimated that the abundance of manganese in HgMn peculiar stars, which have unusually high abundances of mercury and manganese, can be overestimated by several orders of magnitude if hyperfine interaction is not taken into account. Even if a crude estimate of the hyperfine structure through the diagonal hyperfine A and B parameters is performed, the resulting abundance could be overestimated by up to a factor of four.

Neutral manganese (Mn I) is responsible for three near infrared lines at 17325, 17339 and 17349 Å which are among the 25 strongest lines in the H band (1.5 to 1.8 μm). These are all significantly broadened by hyperfine interaction, which most importantly decrease the peak intensities. Omission of such effects will introduce errors in the measurements of wavelengths and derived abundances. Prochaska and McWilliam analyzed the impact of hyperfine interaction on stellar abundance analyses of Mn and Sc and illustrated how incorrect hyperfine splittings can lead to spurious abundances [201].

In paper B_{II} we analyze the hyperfine structure and radiative decay of the transitions $3d^5 4s(^7S)4d\ e\,^6D - 3d^5 4s(^7S)4f\ w\,^6F$ in detail through a comparison with laboratory spectra in a similar fashion as in the project on In II. In contrast to Mn II, which seems

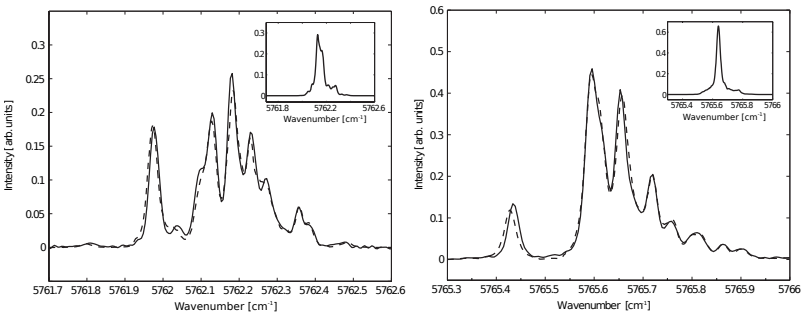

Figure 7.5: Comparison between observed (solid lines) and synthetic spectra of Mn I from a full matrix approach including off-diagonal effects (dashed lines). The left and right panels show the spectral hyperfine features at 17349 and 17339 Å, respectively, and the inset plots show spectra generated by a diagonal calculation. See the text and paper B$_{II}$ for details.

to be well-described by diagonal hyperfine A and B parameters [202, 203], Mn I shows strong effects from off-diagonal hyperfine interaction. Fig. 7.5 presents the hyperfine features due to transitions from $w\,^6\mathrm{F}$ to $e\,^6\mathrm{D}_{5/2}$ and $e\,^6\mathrm{D}_{7/2}$ (the lines at 17349 and 17339 Å respectively), as predicted with a synthetic spectrum obtained using a similar method as for In II including semi-empirical adjustments, and a laboratory spectra recorded with the NIST 2m Fourier transform spectrometer [204]. The reason for why a treatment with the hyperfine A and B parameters fails in these cases, as suggested by Jomaron et al. [200], becomes obvious by comparing the full matrix approach with the corresponding spectra generated by a diagonal calculation shown in the inset plots. A diagonal treatment clearly fails to predict the separation of the single fine-structure line into hyperfine components.

As a test of our results, we use the newly calculated hyperfine-dependent energies and oscillator strengths to model the spectra of the Sun and of the red giant star Arcturus in the relevant spectral region of 1.73-1.74 μm with the MARCS code[1] [206] using atomic

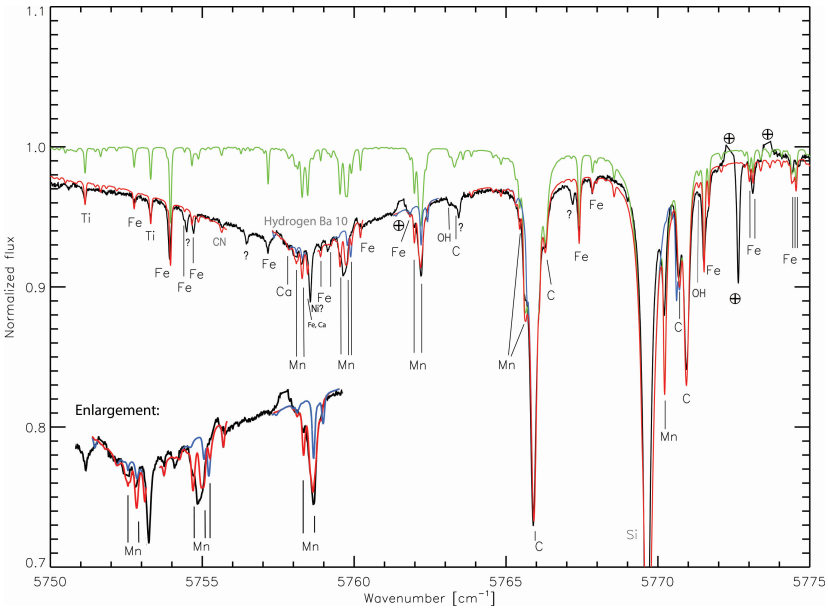

Figure 7.6: The wavelength region of the solar spectrum relevant to our new MnI hyperfine data. The observed spectrum [205] is shown in black, synthetic spectra with and without our new Mn I hyperfine data are shown in red and blue respectively. The green line shows a spectrum generated with the new data but excluding contributions from the Hydrogen Bracket 10 line. The enlargement in the lower left corner highlights a spectral region with interesting Mn I features. See text and paper B II for further details.

data from the VALD database [207]. Fig. 7.6 shows a comparison of synthetic spectra, with and without our new Mn I data, for the Sun with the spectra from the solar atlas [205]. The plot demonstrates that a few of the Mn I lines are almost absent in the spectrum generated from the old atomic data, and for some other lines the

1 We are in dept to P. Barklem and K. Eriksson for valuable help and discussions concerning the modeling of the Hydrogen Bracket 10 line and the running of the MARCS code.

residuals between the observed and synthetic spectra are reduced by half when using the new hyperfine data. These redistributions will have a significant impact on a calculation of the abundances. Vinicius et al. [208] performed an elemental-abundance analysis based on data acquired with the Space Telescope Imaging Spectrograph on the Hubble Space Telescope. In their comparison between observations and simulations, they used our new hyperfine data to update existing line lists of Mn I.

In conclusion, it is clear that the spectral features at 17325, 17339 and 17349 Å in Mn I are not suitable to represent by hyperfine A and B parameters, but should instead be treated in terms of individual hyperfine components due to the large impact from off-diagonal interactions. The new hyperfine data presented in this work should be of use in the analysis of stellar spectra, in particular of HgMn peculiar stars, in the near infrared H band region.

8

UNEXPECTED TRANSITIONS

In addition to the *spectral intensity redistributions* discussed in the previous chapter, the symmetry-breaking perturbations on an atomic system due to hyperfine and/or Zeeman interactions can spawn other interesting effects in atomic spectra. The mixing of states due to the perturbations cause the regular selection rules (see Tab. 3.1) to break down, which could give rise to new lines in the spectrum. This "exotic" class of radiation, termed *unexpected transition*'s (UT's), is defined as transitions which are induced by weak perturbations not included in the gross structure model of the atomic system under investigation [199]. The appearance of an UT is a drastic effect in a spectrum, but these transitions also introduce some more indirect effects. For example, the introduction of new decay channels from a set of states will affect their lifetimes which might show up as deviations from expected trends along an isoelectronic sequence. The discussions presented in this chapter is to a large extent based on the proceeding B_{VI}.

In B_{III} we analyze UT's induced by hyperfine interactions - so-called *hyperfine-induced transition*'s (HIT's) - in Ne-like ions and compare the results with competing forbidden transitions. In B_{IV} and B_{V} we investigate the impact of transitions induced by external magnetic fields - termed *magnetic-field-induced transition*'s (MIT's) - in Ne- as well as Be-like ions. The rate of a MIT in Ne-like Ar was measured by Beiersdorfer et al. [209]. Their determined value did however not agree with the theoretical analysis. In paper B_{IV} we present a careful analysis and resolve the discrepancy. In the work on Be-like ions we investigate the impact of MIT's on storage-ring measurements of E1M1 two-photon transition rates.

Finally, in papers B_{VI} and B_{VII} we outline a novel approach to the challenging measurements of magnetic fields in the solar corona by using a certain MIT in Fe X which has a rate with an enhanced response to the magnetic-field strength. Some of the results presented in these papers will be discussed briefly after a short introduction to UT's in general through a simplistic model for the rate.

8.1 INTRODUCTION - A SIMPLE MODEL

Effects due to UT's are generally significant for atomic systems with metastable excited states which only have slow and/or forbidden decay channels, and which in turn are accidentally near-degenerate with other states having fast decay channels (e.g. E1 transitions). A symmetry-breaking perturbation introduced by hyperfine interactions and/or interactions with an external magnetic field, could then mix the states so that the *slow-decaying state* would obtain properties of the *fast-decaying* state, hence opening up a faster, seemingly unexpected, E1 transition channel from the former.

The theory presented in Ch. 5 which is implemented in RHYZE, can be used to determine properties of radiative transitions in a perturbed atomic system of any class, including HIT's, MIT's as well as those induced by both an external magnetic field and hyperfine interactions (M_F-dependent transitions). Before continuing with some examples from the publications included in this work, we first present a simple model for unexpected transitions induced by a general perturbation.

Assume that a system is well described by a Hamiltonian, H_0, with eigenfunctions $|\Phi_i^0\rangle$ and energies E_i^0 . We represent the symmetry-

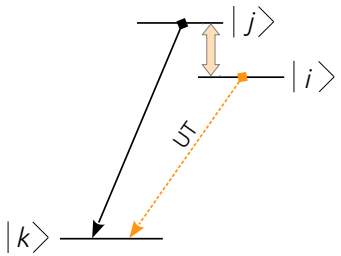

Figure 8.1: A schematic level diagram of a simple three-level system, illustrating the induction of a general *unexpected transition*. The solid line represents a fast transition and the dashed line an unexpected transition. The thick double-headed arrow depicts the symmetry-breaking interaction of the $|i\rangle$ and $|j\rangle$ states inducing the *unexpected transition*.

breaking perturbation by a Hamiltonian, H_1, which will cause a "mixing" of zero-order states and form new eigenstates

$$\Psi_i = \sum_n d_n^i \Phi_n^0 \,. \tag{8.1}$$

The admixture of a certain state j is, to first order, given by

$$d_j^i \approx \frac{\langle \Phi_j^0 | H_1 | \Phi_i^0 \rangle}{E_i - E_j} \,. \tag{8.2}$$

where Φ_i^0 is the reference state for the new eigenstate Ψ_i. Considering the decay of the first excited state shown in Fig. 8.1, and assuming that state $|i\rangle$ is not expected to decay to a lower state $|k\rangle$, we can predict an induced transition rate according to first-order perturbation theory by,

$$A_u\,(i \to k) \approx \left| d_j^i \right|^2 A\,(j \to k) \approx \left| \frac{\langle \Phi_j^0 | H_1 | \Phi_i^0 \rangle}{E_i^0 - E_j^0} \right|^2 A\,(j \to k)\,, \tag{8.3}$$

where it is assumed that the difference in transition energies for $i \to k$ and $j \to k$ is neglected. Note that the notation assumes the

perturbation to be weak enough for us to use the labeling of the unperturbed eigenstates (i and j) also for the perturbed eigenstates giving $A_u\,(i \to k)$. The UT will therefore typically occur (i.e. that $A_u(i \to k)$ is significantly non-zero) in cases where the metastable state $|i\rangle$ is close in energy to an interacting state $|j\rangle$ relative to the interaction strength, and where $|j\rangle$ has a fast decay to the lower state $|k\rangle$ (i.e. that $A(j \to k)$ is comparatively large).

In cases where the state $|i\rangle$ has an *expected* but slow rate, $A_e\,(i \to k)$ (such as a forbidden transition or multi-photon channel) we can express the total rate as,

$$\begin{aligned} A\,(i \to k) &= A_e\,(i \to k) + A_u\,(i \to k) \\ &= A_e\,(i \to k) + \left| \frac{\left\langle \Phi_j^0 \left| H_1 \right| \Phi_i^0 \right\rangle}{E_i^0 - E_j^0} \right|^2 A\,(j \to k) \\ &= A\,(j \to k) \left[\frac{A_e\,(i \to k)}{A\,(j \to k)} + \left| \frac{\left\langle \Phi_j^0 \left| H_1 \right| \Phi_i^0 \right\rangle}{E_i^0 - E_j^0} \right|^2 \right]. \end{aligned} \tag{8.4}$$

From this we can predict that an extra *unexpected* channel has a significant contribution to the decay of $|i\rangle$, induced through the perturbation H_1, if the ratios,

$$\frac{A_e\,(i \to k)}{A\,(j \to k)} \quad \text{and} \quad \left| \frac{\langle \Phi_j^0 \left| H_1 \right| \Phi_i^0 \rangle}{E_i^0 - E_j^0} \right|^2, \tag{8.5}$$

are of comparable size, or if the right ratio is larger than the left.

Classic examples of UT's are the spin-forbidden *intercombination* (IC) transitions in atomic systems well described by non-relativistic models, which are E1 transitions violating the $\Delta S = 0$ spin condition in LSJ-coupling. These transitions occur due to mixing of states with same total angular momentum J, but different total spin, S, due to perturbations from relativistic effects.

Of more importance to the present work, are UT's violating the ΔJ selection rules (see Tab. 3.1), such as $J' = 0 \nrightarrow J = 0$. In ab-

sence of any symmetry-breaking perturbations, such one-photon transitions are strictly forbidden. Mixing of states with different J quantum numbers will also mix their decay properties, and E1 UT's such as "$^3P_0^o$" $\rightarrow$ "$^1S_0^e$" or "$^3P_2^o$" $\rightarrow$ "$^1S_0^e$" could then occur.

8.2 REDUCED TRANSITION RATES

Assume, as is often the case, that the lower state involved in an UT can be represented by a single basis state in the expression for the PSF's (5.1), and that an upper state α is well-described by first-order mixing coefficients d_i^α (8.2). These approximations provide so-called *reduced* transition rates, which are useful since they are approximately independent of the parameters which scale the perturbations.

For MIT's, the d_i^α's then depend linearly on B so that we can define *reduced* coefficients $d_i^{\alpha,R}$ from $d_i^\alpha = B d_i^{\alpha,R}$ and hence also a reduced transition rate, A_{MIT}^R,

$$A_{MIT} \approx B^2 A_{MIT}^R \tag{8.6}$$

which is independent of the magnetic field strength to first order. These rates can then conveniently be tabulated and scaled to the desired magnetic-field strength.

Of more importance are the reduced rates for HIT's. In isoelecotronic analysis we strive for smooth trends to evaluate the accuracy of theoretical models or experiments, see e.g. the discussion on the correlation energy of Ag-like ions in Fig 2.5. Factoring out the dependence on the nuclear parameters I, μ_I and Q provides reduced hyperfine-induced transition rates with a smooth behavior along an isoelectronic sequence. The nuclear part of the hyperfine-dependent transition rate (5.32) can be extracted for specific transitions and under some appropriate approximations with regards to the evaluation of the mixing coefficients. In the case of Be-like ions

and the hyperfine-induced $2s\,2p\ ^3P_0 \rightarrow 2s^2\ ^1S_0$ transition, we can define a reduced rate $A^R_{HIT}(^3P_0 \rightarrow^1 S_0)$ by [210, 211],

$$A_{HIT}(^3P_0 \rightarrow^1 S_0) \approx \mu_I^2(1 - 1/I)A^R_{HIT}(^3P_0 \rightarrow^1 S_0)\,, \qquad (8.7)$$

where we have limited the hyperfine interaction to the nuclear magnetic dipole moment. See the appendix of Brage et al. [210] for how to derive this expression.

In a similar fashion, reduced rates for MIT's in atomic systems with hyperfine transitions could be derived from a careful analysis of the M_F dependent transition rate (5.34).

8.3 MIT'S IN BERYLLIUM-LIKE IONS

Be-like ions are interesting since, in absence of any external perturbations, the lowest-order decay channel from the first excited state is the $2s2p\ ^3P_0 \rightarrow 2s^2\ ^1S_0$ E1M1 two-photon transition. The construction of theoretical models to determine two-photon rates in atomic systems with more than two electrons is an active area of research; see for example the recent work by Amaro et al. [212]. In order to extract the rate of this transition from experiments, Schippers et al. recently proposed to measure the lifetime of the $2s2p\ ^3P_0$ level through storage-ring experiments [213–215]. Such measurements however involve external magnetic fields due to the dipole bending-magnets in the ring, which will open up a MIT decay channel from the same state. To support this type of experiments, we have carried out a careful theoretical analysis of the competition between the MIT and the E1M1 decay channels along the Be-like isoelectronic sequence for ions without nuclear spin. See paper B_V.

Since the ground state $2s^2\ ^1S_0$ is well-separated in energy from other even states, it is well represented as a pure, unmixed state. The $|2s2p\ ^3P_0\ M_J = 0\rangle$ state will however be mixed with other $M_J = 0$ states of similar energies; foremost the $|2s\,2p\ ^3P_1\ M_J = 0\rangle$ state which is closest in energy. The $^3P_1$ level decays through a

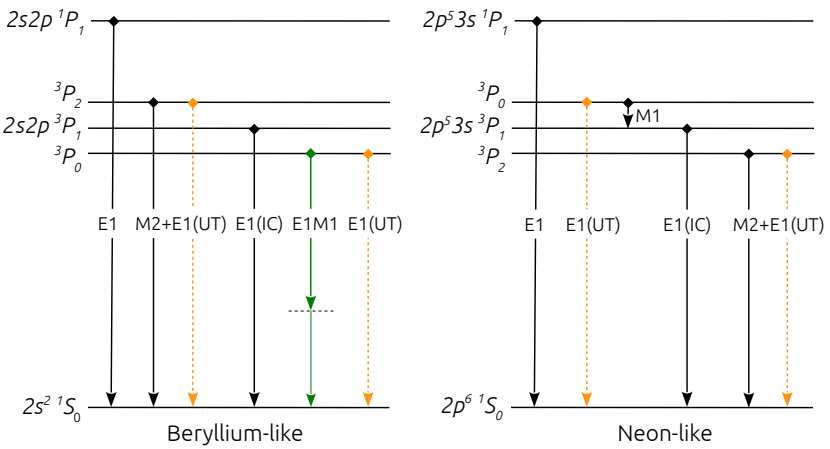

Figure 8.2: Schematic energy structures of Be- and Ne-like ions in the LS-coupled low-Z region of the two isoelectronic sequences. The unexpected transitions (dashed orange lines labeled by UT) may be a MIT (induced by an external magnetic field) or a HIT (induced by hyperfine interaction).

spin-induced (IC) E1 transition to the ground state, a property which will be partly shared with the $^3P_0$ state under the perturbation from the external magnetic field. This will give rise to a magnetic-field induced $|"2s\,2p\,^3P"_0\rangle \rightarrow |"2s^2\,^1S"_0\rangle$ transition, which will have dramatic effects on the total lifetime of the upper state. We show in this work that this MIT will be sensitive to, not only the mixing of $|^3P_0\,M_J = 0\rangle$ with $|^3P_1\,M_J = 0\rangle$, but also with $|^1P_1\,M_J = 0\rangle$. The left panel of Fig. 8.2 shows a schematic energy level diagram of Be-like ions at the neutral end of the isoelectronic sequence, including also relevant decay processes.

We show that the MIT rate, with a typical storage-ring field strength, is at least of the same order of magnitude as the E1M1 rate for intermediately charged ions and completely dominating for ions at the neutral end. Measurements of two-photon rates should therefore be carefully aided by an analysis of the perturbation due to the magnetic field for higher nuclear charges.

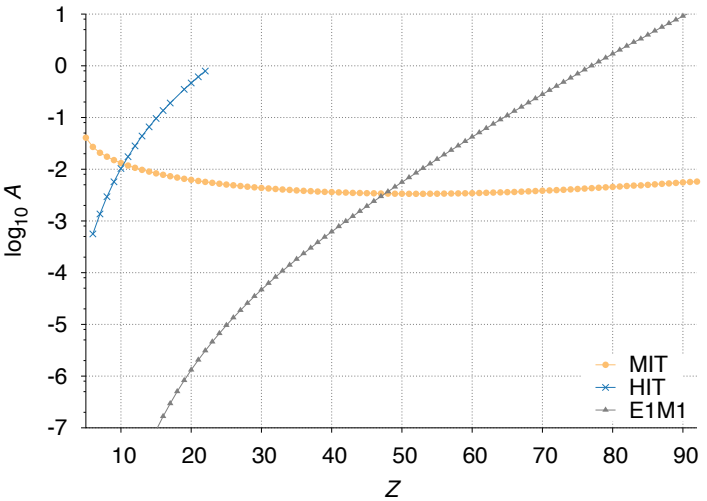

Figure 8.3: Rates associated with different transition channels from the excited $|2s\,2p\ ^3P_0\rangle$ state to the $|2s^2\ ^1S_0\rangle$ ground state in Be-like ions. The E1M1 transition rates by Laughlin [216] are given in units of s^{-1} while the reduced MIT (8.6) and HIT (8.7) rates are given in $s^{-1}T^{-2}$ and $s^{-1}\mu_N^{-2}$ respectively, where μ_N is the nuclear magneton. The HIT rates are from Andersson et al. [211]. See the text and paper B_V for details.

In some more detail, in Fig. 8.3 we compare the reduced MIT rates (8.6) (corresponding to $B = 1$ T) obtained in this work, with the corresponding reduced *hyperfine induced transition* (HIT) rates, to be discussed in Sec. 8.5, as well as the E1M1 rates calculated using the analytical expression by [216]. The uncertainty in Laughlin's prediction of the E1M1 rates is expected to be large for highly charged ions. The recent theoretical work by Amaro et al. [212] suggests that Be-like Xe^{50+} and U^{88+} have E1M1 rates of 5×10^{-3} and 8×10^{-2} s^{-1}, respectively. These values are orders of magnitude smaller than the rates predicted by Laughlin, which should further complicate the storage-ring measurements.

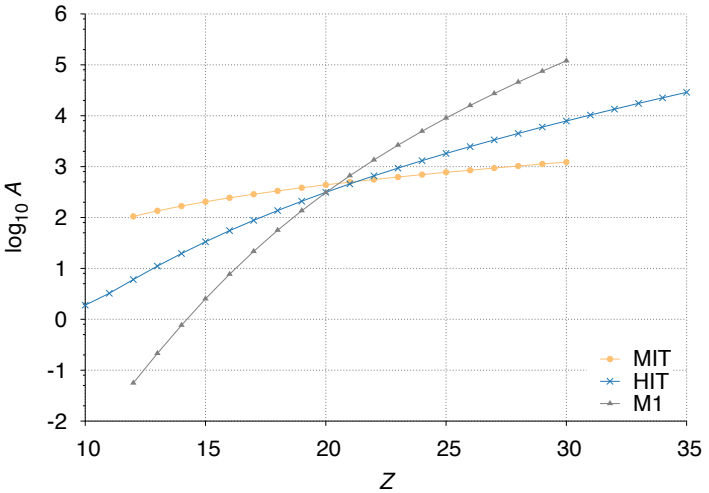

Figure 8.4: Rates associated with different transition channels from the excited $|2p^5\ 3s\ ^3P_0\rangle$ state to the $|2p^6\ ^1S_0\rangle$ ground state in Ne-like ions. The M1 transition rate is given in units of s^{-1}, while the reduced MIT (8.6) and HIT (8.7) rates are given in $s^{-1}T^{-2}$ and $s^{-1}\mu_N^{-2}$ respectively, where μ_N is the nuclear magneton. See the text and papers B_{III} and B_{IV} for details.

8.4 MIT'S IN NEON-LIKE IONS

Paper B_{IV} concerns what is arguably the first, experimental measurement of a MIT: the EBIT observation of the unexpected transition $2p^5 3s\ ^3P_0 \rightarrow 2p^6\ ^1S_0$ in Ne-like Ar by Beiersdorfer [209]. The right panel of Fig. 8.2 shows a schematic energy level diagram of Ne-like ions, which highlights the similarities to Be-like ions, but also the importance of the reversed fine structure of the ^3P-term. Some theoretical predictions for the MIT were also presented by Beiersdorfer et al., but the deduced transition rates did not seem to agree with the experiment. The authors also discussed how the MIT's can be used as a diagnostic tool of magnetic field strength for high temperature plasmas, in e.g. fusion devices.

Motivated by the discrepancy between theory and experiment, we carried out large-scale calculations to predict the MIT's for all isotopes without nuclear spin in the isoelectronic sequence between Ne I and Zn XXI. In analogy to the Be-like case, we find that it is crucial to include both perturber states, $|^3P_1\rangle$ and $|^1P_1\rangle$, which was not the case in the original prediction by Beiersdorfer et al., in order to accurately represent the MIT rates.

The MIT decay channel competes with the M1 transition $^3P_0 \rightarrow {}^3P_1$, as shown in Fig. 8.2. A comparison along the isoelectronic sequence of the M1 and reduced MIT rates (8.6) (corresponding to $B = 1$ T) rates is shown in Fig. 8.4. From this plot it is clear that the MIT channel, at this field strength, dominates over the M1 channel for $Z \leqslant 20$. The influence of the magnetic field on the $^3P_0$ level has a direct visible impact on the spectrum. The M1 transition will become weaker with increasing field strength, while a new line will appear in a different part of the spectrum, between the resonant and IC E1 transitions. The corresponding branching ratio is therefore an especially interesting parameter to investigate along the isoelectronic sequence. See paper B$_{IV}$ for further details.

Finally, it is encouraging to see that a recent EBIT measurement by the same group confirms our theoretical prediction of the MIT rate in Ne-like Fe [123]. Our ab-inito prediction of the M1 rate is 1.588×10^4 s^{-1}, which gives a zero-field limit value of $\tau = 63.0$ μs for the lifetime of the $^3P_0$ state. We determine the reduced MIT rate to 850 s^{-1}T^{-2}, which together with our theoretical value for the M1 decay, gives a total lifetime of the $^3P_0$ state to 42.4 μs at $B = 3$ T, which agrees to within 3.5% with the new experimental value of 44.00 ± 0.42 μs[1]. The authors suggest that the remaining difference could be partly explained by unmeasured drifts of the magnetic field away from its nominal value in the EBIT.

1 The uncertainty given here is from the fit of their measured decay curve.

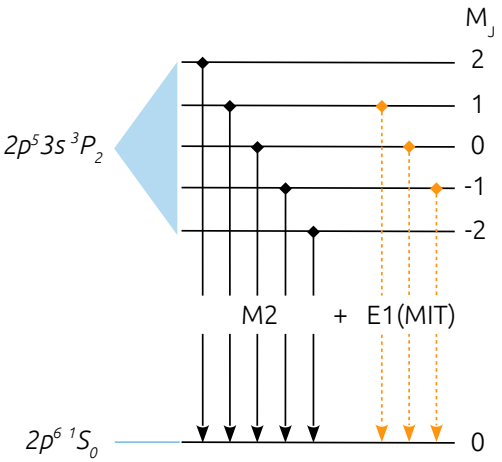

Figure 8.5: Schematic energy structure of the splitting of the $2p^5 3s\,{}^3P_2$ level in Ne-like ions into five magnetic sublevels under influence of an external magnetic field. The emitted radiation of the MIT and the competing M2 decay channel have different angular distributions and an interference effect will therefore be observable.

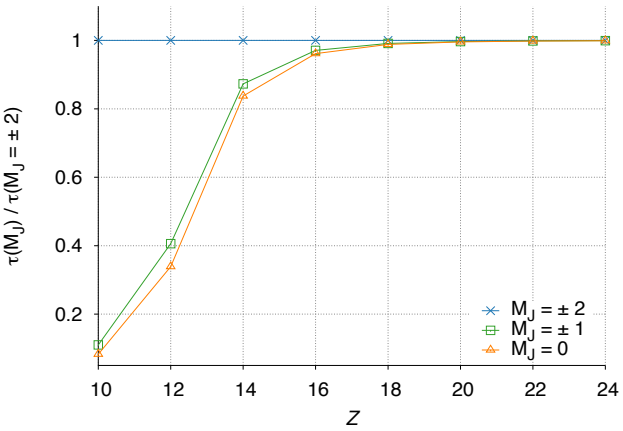

Figure 8.6: Lifetimes of the different magnetic sublevels of $2p^5 3s\,{}^3P_2$ in Ne-like ions, relative to the $M_J = \pm 2$ levels, for an external magnetic field of 1 T.

8.4.1 M_J-dependent Lifetimes

From Fig. 8.2 it is clear that Ne-like ions also have other MIT candidates - the $2p^5\,3s\ {}^3P_2 - 2p^6\ {}^1S_0$ transitions. A closer look at these transitions, see Fig. 8.5, reveals that the ${}^3P_2$ M_J-sublevels have different decay modes. The $M_J = \pm 2$ sublevels decay by M2 transitions, while the others have an additional MIT channel. This extra branch will affect the lifetimes and introduce an M_J-dependence due to the external magnetic field. This is illustrated in Fig. 8.6, where the lifetimes of the different sublevels are plotted relative to the lifetime of the $M_J = \pm 2$ levels, for a magnetic field $B = 1$ T (i.e. the reduced rate defined in (8.6)). It is clear that the lifetimes of the $M_J = 0, \pm 1$ levels are substantially decreased for low Z. However, the M2 rate increases faster than the MIT rate with Z and dominates already for $Z = 20$. This will make the lifetimes for higher Z independent of M_J.

8.4.2 M_F-dependent Radiative Properties

As a rare example on the theory side, Li et al. [217] analyzed the hyperfine-induced $2s2p\ {}^3P_0 \rightarrow 2s^2\ {}^1S_0$ transition rates of Be-like ^{47}Ti in an external magnetic field, by using an approach similar to the one described in the present work, to investigate the effect of the external magnetic field on the extraction of the hyperfine-induced transition rate in a storage-ring experiment [218]. Note that the authors chose to neglect mixing of states with different F due to a comparatively weak magnetic field. A more recent experiment was carried out to extract the rate of the same *hyperfine-induced transition* in Be-like S [219] which remains to be verified by theory. The development of general-purpose tools such as the RHYZE code outlined in Ch. 6, should open up for future systematic studies of M_F-dependent effects.

8.4.3 *Radiative Angular Distributions*

An external magnetic field introduces a preferred direction in space which opens up for measurements of the angular distribution of the emitted radiation. The $2p^5\,3s\ {}^3P_2 \rightarrow 2p^6\ {}^1S_0$ decay in Ne-like ions reveals measurable properties depending on the magnetic quantum numbers, M_J. The fact that the competing M2 channels are between the same levels and do have different angular distribution with respect to the magnetic field direction, results in possible M_J-dependent *interference effects*. This particular case was investigated by Li et al. [220] who illustrated that the interference term has a major impact on the distribution of the radiation. Systematic studies of angular distributions of radiation and associated interference effects requires implementation of the methods in general-purpose codes, such as RHYZE.

8.5 HIT'S IN NEON-LIKE IONS

In Sec. 8.4 we investigated the magnetic-field induced decay from $|2p^5\,3s\ {}^3P_0\rangle$ in Ne-like ions, we now turn to hyperfine-induced effects of the same system.

It is clear from the level diagram in Fig. 8.2 that, in absence of a nuclear spin (or a magnetic field), the decay from $|{}^3P_0\rangle$ is dominated by a forbidden M1 transition to $|{}^3P_1\rangle$. If however the ion under investigation has a non-zero nuclear spin, the hyperfine interaction will open up a *hyperfine-induced* E1 channel down to the ground state $|2p^6\ {}^1S_0\rangle$. We show in paper B_{IV} that this does not only significantly lower the lifetime of the state, but also change the spectra of the ion dramatically by decreasing the intensity of the ${}^3P_0 \rightarrow {}^3P_1$ line and introducing a $2p^5\,3s\ {}^3P_0 \rightarrow 2p^6\ {}^1S_0$ line.

Fig. 8.4 illustrates how the reduced HIT rate varies along the Ne-

like isoelectronic sequence in relation to the M1 and reduced MIT rates. If we disregard the MIT, it is clear that the HIT is likely to be the dominating transition channel for low Z ions, whereas the M1 channel dominates in the higher end of the sequence. The HIT and M1 rates are likely to be of the same order of magnitude in the intermediate region around $Z = 20$.

For the special case of ^{21}Ne I ($I = 3/2$) the HIT rate is predicted to be 1.388 s^{-1}, that is three orders of magnitude faster than the M1 rate at 2.4016×10^{-3} s^{-1}. This value for the HIT rate confirms the elaborate theoretical investigation of hyperfine induced effects in Ne I by Li et al. [221] in which they predicted the rate to 1.484 s^{-1}, which is within 5% from our result.

8.6 MIT's TO PROBE CORONAL MAGNETIC FIELDS

As a final topic of this thesis, lets return to the subject of measuring magnetic fields in the solar corona introduced in Sec. 1.2.2 of the introductory chapter. We discussed that in order to do space-weather forecasts it is necessary to follow the evolution of the solar activity, in particular active regions which might spawn flares or CME's. This requires continuous observations of the magnetic field which dictates much of the solar structure and dynamics through e.g. magnetic reconnection processes [26, 27].

Measurement of the coronal magnetic fields is however very complicated and so far no direct space-based methods to probe the corona magnetic fields exist. The reason is that the coronal plasma is both hot and dilute. The extremely high temperatures (millions of °C) gives highly-charged ions with strong internal magnetic fields, while the low particle densities results in weak external fields (current estimates range from 0 to 2000 gauss). This combination means that it is very hard to find observable quantities in atomic spectra which are affected by the external fields. So far one has only been able to estimate the fields through extrapolations

of the stronger photospheric fields. These are easier to determine since the plasma here is much colder (~ 6000 °C) - giving lower charge-state ions with relatively weak internal fields - and denser - giving stronger external fields. Schrijver et al. carried out a non-linear force-free field modeling using vector-magnetographic data observed by the Hinode satellite [222]. On the ground-based side there are infrared or radio measurements; the former is limited by optical thickness while the latter only refer to specific portions of the corona. It is clear that the demand for alternative approaches is great.

In paper B_{VII} we outline a novel approach to directly measure the coronal fields, based on our previous works on MIT's outlined in papers B_{IV}, B_V and B_{VI}. The suggested method is based on an exotic type of radiative transition in Fe X (Fe^{9+}), in the XUV spectral region at 257.26Å, which has a transition rate that is sensitive to the surrounding magnetic field - namely a MIT. This MIT makes up a truly unique case since it is emitted by an ion with high abundance at the temperatures in the solar corona[2], and that also happens to fulfill the rather extreme requirements necessary for production of an MIT with a pronounced magnetic field response. Fig. 1.4 in Ch. 1 shows an example XUV spectrum of the Solar corona recorded by the Hinode mission [37]. The Fe X MIT belongs to the blended structure at 257.26 Å.

The Fe X system can be represented by the schematic energy level-diagram system shown in Fig. 8.7, from where it is clear that the $^4D_{7/2}$ and $^4D_{5/2}$ states have very different decay modes. The former can only decay via forbidden M2 transitions, while the latter has a fast E1 channel. Similar to the previous analyzed Be- and Ne-like systems, the perturbation from the external magnetic field causes the two excited states to mix such that the metastable $^4D_{7/2}$ state gains properties of the resonant $^4D_{5/2}$ state and thereby

2 The M1 transition connecting the two states in the ground configuration of Fe X is Edléns' famous coronal red line at 6374 Å used for temperature determinations [23–25].

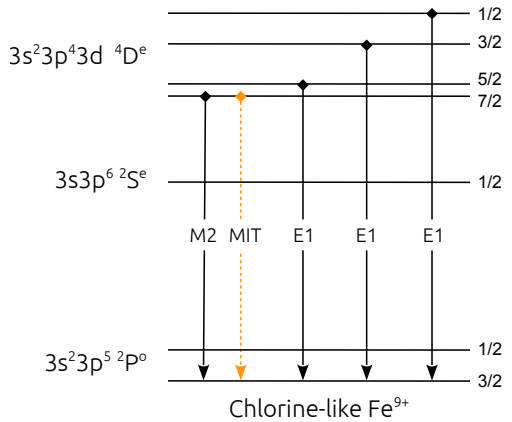

Figure 8.7: Schematic energy level diagram for the ground and first excited states in Cl-like Fe (Fe X) with some relevant decay channels indicated, most importantly the MIT from $^4D_{7/2}$.

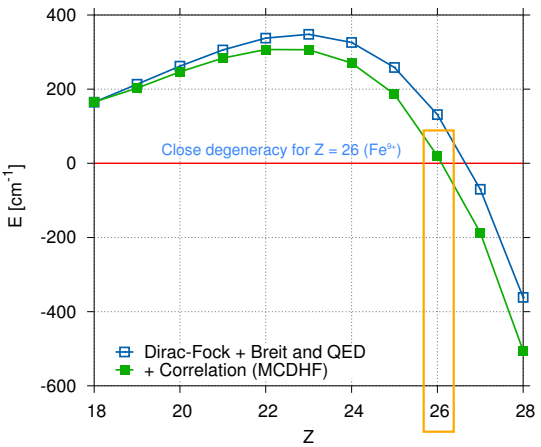

Figure 8.8: A plot of the ΔE energy separation between the $^4D_{7/2}$ and $^4D_{5/2}$ states in Fe X along the Cl-like isoelectronic sequence. The blue curve with unfilled squares represents energies from an (uncorrelated) DHF calculation including the Breit interaction and leading QED effects. The green curve with filled squares corresponds to inclusion of electron correlation from a MCDHF calculation. See the text and paper B_{VII} for details.

speeding up its decay in proportion to the field strength via an magnetic-field induced E1 transition. By knowing its dependence on the field strength one can use the intensity of this magnetic-field induced transition to determine properties about the surrounding field.

To predict the sensitivity of this line on the magnetic field we outline in this work a theoretical model based on MCDHF wavefunctions in combination with the theory for MIT rates discussed in this chapter, but also in more detail in Ch. 5 and 6, see in particular expression (5.33). The theoretical investigation of the Cl-like isoelectronic sequence shows that two of the ^{4}D levels undergo a fine-structure inversion around Fe X, resulting in an accidental quasi-degeneracy between the resonant $^4D_{5/2}$ and metastable $^4D_{7/2}$ states. Fig. 8.8 shows the trend of the energy separation between these two states along the sequence.

A simple first order treatment of the MIT rate in Fe X gives an approximate dependence on some important parameters,

$$A_{MIT} \propto \frac{B^2}{\lambda^3 \Delta E^2} \tag{8.8}$$

where B is the magnitude of the external magnetic field, λ is the transition wavelength and ΔE is the energy separation between the metastable and the resonant state. This implies that an accurate value for ΔE is crucial to the prediction of the MIT rate. It is believed that the level of degeneracy lies within 20 cm^{-1}. Our latest investigations, presented in paper B$_{VIII}$, suggests a separation of ~ 3.5 cm^{-1} with an upper limit of 8.4 cm^{-1}. An very recent analysis, based on SkyLab data, points towards an even smaller value of 3.6 ± 2.7 cm^{-1} [223].

In Fig. 8.9 we present the MIT rate along the Cl-like isoelectronic sequence for $\Delta E = 5$ and 20 cm^{-1} respectively, showing the resonant behavior of the rate at Fe X ($Z = 26$) as well as its strong dependence on the magnetic field strength[3]. Using the new value

3 I am grateful to Wenxian Li for providing the plots shown in Fig. 8.9, 8.11 and 8.12.

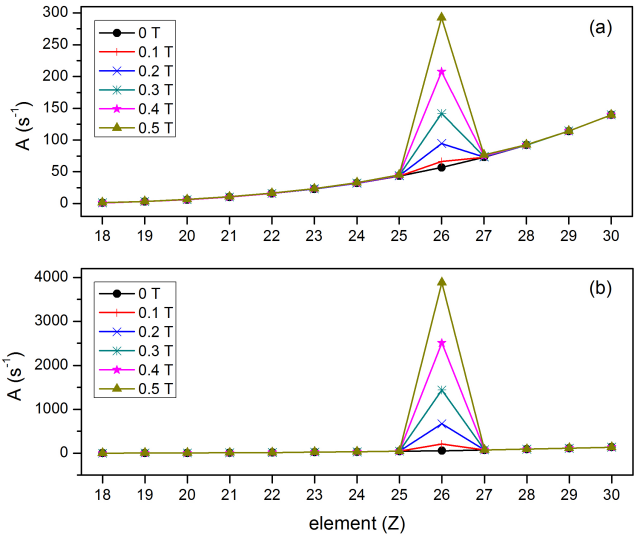

Figure 8.9: Theoretical prediction of the $^4D_{7/2} \rightarrow {}^2P_{3/2}$ MIT rate along the Cl-like isoelectronic sequence for $\Delta E = 20$ (a) and 5 cm^{-1} (b). See the text and paper B_{VII} for details.

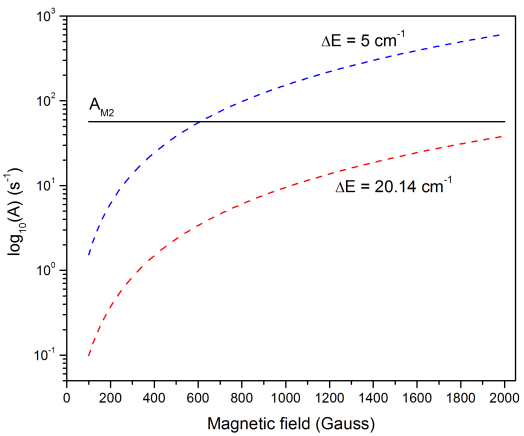

Figure 8.10: Comparison of the $^4D_{7/2} \rightarrow {}^2P_{3/2}$ MIT rate with the rate of the competing M2 decay channel as a function of B for $\Delta E = 20$ and 5 cm^{-1}. See the text and paper B_{VII} for details.

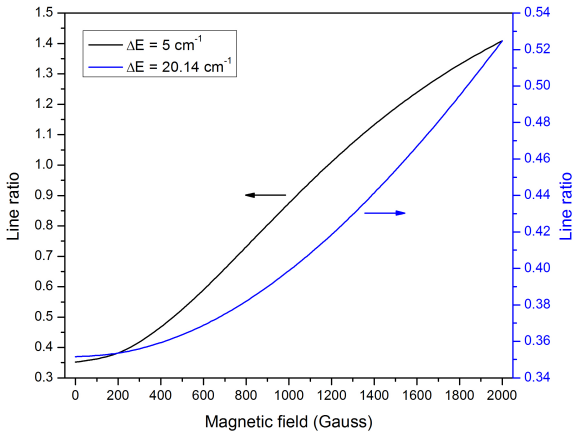

Figure 8.11: A CR model of the line ratio between the *blended* MIT+M2 transition and the allowed E1 channel from $^4D_{5/2}$ for $\Delta E = 20$ and 5 cm^{-1}, as a function of B, for a typical EBIT plasma environment. See the text and paper B_{VII} for details.

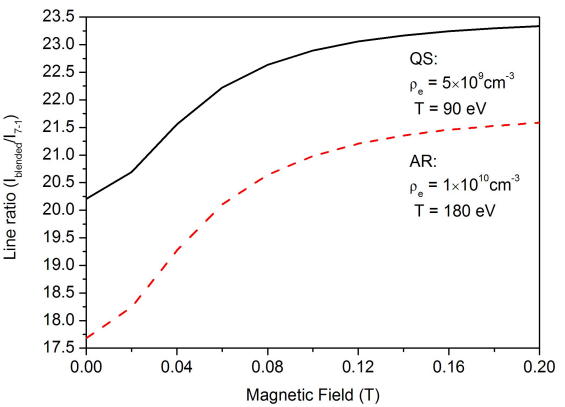

Figure 8.12: A CR model of line ratio between the *blended* MIT+M2 line and the E1 line from $^4D_{1/2}$ (labeled "7-1") for $\Delta E = 3.5$ cm^{-1}, as a function of B, for QS and AS coronal plasma environments. See the text and paper B_{VIII} for details.

of $\Delta E = 3.6\ cm^{-1}$ for the quasi-degeneracy would further enhance this behavior. A comparison between the rate of the MIT and the rate of the competing forbidden M2 decay channel is shown in Fig. 8.10 for B up to 2000 gauss, which is the maximum field expected in the solar corona.

Finally, Fig. 8.11 shows results from a collisional-radiative (CR) modeling [224] of the line ratio between the *blended* MIT+M2 transition and the allowed E1 transition from $^4D_{5/2}$, as a function of the magnetic field strength, B. This simulation was performed with the CR model implemented in the FAC code [121] for a fixed electron density of $10^{11}\ cm^{-1}$, which is typical for an EBIT plasma environment. It is clear that the line ratio shows a strong dependence on the magnetic field strength. While this electron density is typical for EBIT's, it also happens to be in the range for the densities expected in the solar corona. However, due to the high resolution power required to resolve the lines from $^4D_{7/2}$ and $^4D_{5/2}$ respectively, it is more realistic to make use of line-ratios of the MIT+M2 line with one of the E1 transition from $^4D_{3/2}$ or $^4D_{1/2}$. The line from $^4D_{3/2}$ is however blended by a He II line at 256.317 Å in the corona. In Fig. 8.12 we present a CR model of the line ratio between the MIT+M2 and the E1 transition from $^4D_{1/2}$, for typical quiet sun (QS) [225] and active region (AR) [226] coronal plasma environments. A spectroscopic measurement of this line ratio is less sensitive to the magnetic-field strength than the direct measurement of the ratio between the lines from $^4D_{7/2}$ and $^4D_{5/2}$, but on the other hand it would require less spectral resolution.

In conclusion, the origin of the extreme temperatures in the corona as well as violent events such as flares or CME's remains unexplained. These processes are believed to be related to energy contained in the solar magnetic fields. Space-based direct measurements of the coronal magnetic fields are currently inaccessible and have so far only been estimated by numerical simulations/extrapolations. In this work, outlined in papers B_{VII} and B_{VIII}, we propose an alternative method based on line ratios involving an en-

hanced MIT in Fe X at 257Å and discuss how it can be applied in measurements of fields in the solar corona. The MIT was found from systematic theoretical investigations of various isoelectronic sequences, and the Cl-like sequence in particular. MIT's are extremely rare so it is almost a "God-given" coincidence that Fe X also happens to be abundant in the Solar corona.

9

SOME CONCLUDING WORDS

Motivated by spectroscopic analysis of astrophysical and laboratory plasma (Ch. 1), this thesis has been concerned with the fundamental structure (Ch. 2) and spectral properties (Ch. 3) of atoms and their ions, possibly including also the effects of non-spherical interactions with nuclei of non-zero spin, as well as interactions with external magnetic fields (Ch. 5). A theoretical framework has been outlined and used in scientific computer codes (Ch. 4) to predict the emission or absorption of radiation, of atomic systems in general, and of heavy and highly charged ions in particular. In ab-inito theoretical models, such as the *multiconfiguration Dirac-Hartree-Fock* method employed in the present work, one obtain, not only energy levels, but also wavefunctions representing the corresponding quantum states. These wavefunctions can then be used to determine any desired physical observable, at least in principle. The most important of these observables, for our purposes, are the strengths of spectral lines.

The first set of publications, paper A$_{\mathrm{I}}$ to A$_{\mathrm{VII}}$, concerns ab-initio predictions of atomic structure and radiative transition rates, with a particular focus on *relativistic* and *electron-correlation effects*. Detailed understanding of atomic properties are of fundamental importance to analyze astrophysical spectra for determination of e.g. element abundances in stars, but also in the diagnostics of laboratory plasma such as in the fusion reactors. Systematic and large-scale *multiconfiguration Dirac-Hartree-Fock* calculations has been carried out, often in combination with *electron-beam ion trap* experiments.

The second set of publications, B_{I} to B_{VIII}, presents a rigorous treatment of effects from non-spherical nuclear charge distributions - *hyperfine interaction* - and external magnetic fields - *Zeeman interaction* - on atomic spectra. In relation to this, a general methodology has been developed and implemented in a general-purpose computer code (Ch. 6) to include these symmetry-breaking perturbations in the wavefunctions and to determine their impact on the resulting spectra. In particular, these publications concern *intensity redistributions* (Ch. 7) and *unexpected transitions* (Ch. 8) in atomic spectra, and their applications to abundance analyses in stellar atmospheres, to the impact of magnetic fields in storage ring experiments, as well as to coronal magnetic field measurements and, ultimately, space-weather meteorology.

BIBLIOGRAPHY

[1] T. S. Kuhn, *The structure of scientific revolutions (50th Anniversary Edition: 2012)*, University of Chicago press, **1962** (cit. on p. 3).

[2] NASA/WMAP 9-year results, **2016**, http://wmap.gsfc.nasa.gov/news/index.html (cit. on p. 4).

[3] A. K. Pradhan, S. N. Nahar, *Atomic Astrophysics and Spectroscopy*, Cambridge University Press, **2011** (cit. on p. 4).

[4] D. A. Gurnett, A. Bhattacharjee, *Introduction to plasma physics: with space and laboratory applications*, Cambridge University Press, **2005** (cit. on p. 4).

[5] B. P. Abbott et al., *Astrophy. J. Lett.* **2016**, *818*, L22 (cit. on p. 4).

[6] R. L. Kurucz, I. Furenlid, J. Brault, L. Testerman, *National Solar Observatory Atlas Sunspot New Mexico: National Solar Observatory 1984* **1984**, *1* (cit. on p. 5).

[7] C. A. Hampel, *Recent Advances in Physical and Inorganic Chemistry*, Van Nostrand Reinhold, **1968** (cit. on p. 5).

[8] A. W. Stewart, *Recent Advances in Physical and Inorganic Chemistry*, Biblio-Life, **2008** (cit. on p. 6).

[9] The British Association, *Nature* **1871**, *4*, 261–278 (cit. on p. 6).

[10] ITER: The International Thermonuclear Experimental Reactor, **2016**, http://www.iter.org (cit. on p. 7).

[11] B. Bigot, *Nature* **2015**, *522*, 149–151 (cit. on p. 7).

[12] MEGAPROJECT: The Effective Design and Delivery of Megaprojects in the EU. European Cooperation in Science and Technology. (TUD COST Action TU1003), **2016**, http://www.cost.eu/COST_Actions/tud/TU1003 (cit. on p. 7).

[13] ITER: The International Thermonuclear Experimental Reactor - External Heating System, **2016**, https://www.iter.org/mach/Heating (cit. on p. 7).

[14] EUROfusion - the European Consortium for the Development of Fusion Energy, **2016**, https://www.euro-fusion.org (cit. on p. 8).

[15] N. J. Peacock et al. *Diagnostics for Experimental Thermonuclear Fusion Reactors*, (Eds.: P. E. Stott, G. Gorini, E. Sindoni), Springer US, Boston, MA, **1996**, pp. 291–305 (cit. on p. 8).

[16] M. L. Qiu et al., *J. Phys. B: At. Mol. Opt. Phys.* **2015**, *48*, 144029 (cit. on p. 9).

[17] R. Hutton, Fudan University (private communication), **2016** (cit. on p. 9).

[18] T. Nakano et al., *J. Phys. B: At. Mol. Opt. Phys.* **2015**, *48*, 144023 (cit. on p. 9).

[19] A. Kramida, Yu. Ralchenko, J. Reader, NIST ASD Team, NIST Atomic Spectra Database (ver. 5.2), [Online] [2015, October 29] National Institute of Standards and Technology, Gaithersburg, MD, **2015**, http://physics.nist.gov/asd (cit. on pp. 9, 43).

[20] The Solar Dynamics Observatory (SDO), **2016**, http://sdo.gsfc.nasa.gov (cit. on p. 10).

[21] V. A. Slemzin, F. F. Goryaev, S. V. Kuzin, *Plasma Phys. Rep.* **2014**, *40*, 855–892 (cit. on pp. 10, 13).

[22] G. Del Zanna, H. Mason *Planets, Stars and Stellar Systems: Volume 4: Stellar Structure and Evolution*, (Eds.: T. D. Oswalt, M. A. Barstow), Springer Netherlands, Dordrecht, **2013**, pp. 87–205 (cit. on pp. 10, 13).

[23] B. Edlén, *MNRAS* **1945**, *105*, 323–333 (cit. on pp. 10, 95, 161).

[24] B. Edlén, *Z. Astrophys.* **1943**, *22*, 30 (cit. on pp. 10, 161).

[25] P. Swings, *Astrophys. J.* **1943**, *98*, 116–128 (cit. on pp. 10, 161).

[26] M. Aschwanden, *Physics of the solar corona: an introduction with problems and solutions*, Springer Science & Business Media, **2006** (cit. on pp. 11, 160).

[27] E. Priest, *Magnetohydrodynamics of the Sun*, Cambridge University Press, **2014** (cit. on pp. 11, 160).

[28] G. E. Hale, *Astrophys. J.* **1908**, *28*, 315 (cit. on pp. 11, 98).

[29] Swedish Space Weather Center (SRC) at the Swedish Institute of Space Physics (IRF), **2016**, http://src.irf.se (cit. on p. 11).

[30] SWPC: Space Weather Prediction Center (Boulder, USA), **2016**, http://www.swpc.noaa.gov (cit. on p. 11).

[31] P. Judge et al., *NASA STI/Recon Technical Report N* **2001**, *2* (cit. on p. 12).

[32] P. J. Mohr, D. B. Newell, B. N. Taylor, *arXiv:1507.07956 [physics.atom-ph]* **2015**, http://arxiv.org/abs/1507.07956 (cit. on p. 12).

[33] R. Machleidt, D. Entem, *Phys. Rep.* **2011**, *503*, 1–75 (cit. on p. 12).

[34] I. Lindgren, J. Morrison, *Atomic Many-Body Theory*, Springer-Verlag, Berlin Heidelberg New York, **1982** (cit. on pp. 12, 15, 90, 104).

[35] C. Froese Fischer, T. Brage, P. Jönsson, *Computational atomic structure: an MCHF approach*, Inst. of Physics Publishing, Bristol, **1997** (cit. on pp. 12, 44, 58, 63, 64, 79, 84, 101, 104).

[36] I. P. Grant, *Relativistic Quantum Theory of Atoms and Molecules: Theory and Computation (Springer Series on Atomic, Optical, and Plasma Physics)*, Springer-Verlag New York, Inc., Secaucus, NJ, USA, **2007** (cit. on pp. 12, 15, 32–34, 46, 51, 53, 55, 70–72, 75, 77, 80).

[37] T. Watanabe, National Astronomical Observatory of Japan (NAOJ), XUV Hinode data (private communication), **2016** (cit. on pp. 13, 161).

[38] J. M. Dahlström, A. L'Huillier, A. Maquet, *J. Phys. B: At. Mol. Opt. Phys.* **2012**, *45*, 183001 (cit. on p. 12).

[39] T. Carette, L. Argenti, E. Lindroth, *J. Phys.: Conf. Ser.* **2012**, *388*, 022020 (cit. on p. 12).

[40] B. M. Roberts, V. A. Dzuba, V. V. Flambaum, *Phys. Rev. A* **2014**, *89*, 042509 (cit. on p. 13).

[41] J. K. Webb et al., *Phys. Rev. Lett.* **2011**, *107*, 191101 (cit. on p. 13).

[42] J. A. King et al., *MNRAS* **2012**, *422*, 3370–3414 (cit. on p. 13).

[43] Y. V. Stadnik, V. V. Flambaum, *Phys. Rev. Lett.* **2015**, *114*, 161301 (cit. on p. 13).

[44] N. Leefer et al., *Phys. Rev. Lett.* **2013**, *111*, 060801 (cit. on p. 13).

[45] M. S. Safronova et al., *Phys. Rev. Lett.* **2014**, *113*, 030801 (cit. on pp. 13, 87).

[46] V. A. Dzuba, V. V. Flambaum, *Phys. Rev. A* **2016**, *93*, 052517 (cit. on p. 13).

[47] G. W. Drake, *Springer Handbook of Atomic, Molecular, and Optical Physics (2nd ed.)* Springer, **2006**, p. 1504 (cit. on p. 13).

[48] A.-M. Mårtensson-Pendrill, *Can. J. Phys.* **2008**, *86*, 99–109 (cit. on p. 13).

[49] P. Strange, *Relativistic Quantum Mechanics*, Cambridge University Press, **1998**, p. 610 (cit. on pp. 15, 32).

[50] W. R. Johnson, *Atomic structure theory*, Springer, **2007** (cit. on pp. 15, 39, 40, 69).

[51] I. Lindgren, *Relativistic many-body theory*, Springer, **2011** (cit. on pp. 15, 27, 32).

[52] C. F. Fischer et al., *J. Phys. B: At. Mol. Opt. Phys.* **2016**, *49*, 182004 (cit. on pp. 15, 46, 53).

[53] C. F. Fischer, *The Hartree-Fock Method for Atoms: A Numerical Approach*, John Wiley and Sons, Inc., New York, **1977** (cit. on pp. 17, 52).

[54] G. Racah, *Phys. Rev.* **1942**, *62*, 438–462 (cit. on pp. 18, 44).

[55] G. Racah, *Phys. Rev.* **1943**, *63*, 367–382 (cit. on pp. 18, 44, 46).

[56] G. Racah, *Phys. Rev.* **1949**, *76*, 1352–1365 (cit. on pp. 18, 44, 46).

[57] R. D. Cowan, *The Theory of Atomic Structure and Spectra*, University of California Press, **1981**, 731 pp. (cit. on pp. 19, 45–48, 78, 79, 102, 103, 107, 108, 112).

[58] D. A. Varshalovich, A. N. Moskalev, V. K. Khersonskii, *Quantum theory of angular momentum*, World Scientific, **1988** (cit. on p. 19).

[59] W. Kutzelnigg *Theoretical Chemistry Accounts: New Century Issue*, (Eds.: C. J. Cramer, D. G. Truhlar), Springer Berlin Heidelberg, Berlin, Heidelberg, **2001**, pp. 182–186 (cit. on p. 21).

[60] P. A. M. Dirac Proceedings of the Royal Society of London A: Mathematical, Physical and Engineering Sciences, *Vol. 123*, The Royal Society, **1929**, pp. 714–733 (cit. on p. 21).

[61] The World Cultural Council (WCC) - Albert Einstein World Award of Science, **2016**, http://www.consejoculturalmundial.org/awards/world-award-of-science (cit. on p. 22).

[62] D. J. Gorin, F. D. Toste, *Nature* **2007**, *446*, 395–403 (cit. on p. 22).

[63] P. Pyykkö, *Angewandte Chemie International Edition* **2004**, *43*, 4412–4456 (cit. on p. 22).

[64] P. Pyykkö, *Inorganica Chimica Acta* **2005**, *358*, Protagonists in chemistry - Hubert Schmidbaur, 4113–4130 (cit. on p. 22).

[65] P. Pyykkö, *Chem. Soc. Rev.* **2008**, *37*, 1967–1997 (cit. on p. 22).

[66] P. Pyykkö, *Annu. Rev. Phys. Chem.* **2012**, *63*, PMID: 22404585, 45–64 (cit. on pp. 22, 26).

[67] P. Pyykkö, *Phys. Chem. Chem. Phys.* **2011**, *13*, 161–168 (cit. on p. 22).

[68] P. Schwerdtfeger, *Heteroatom Chemistry* **2002**, *13*, 578–584 (cit. on p. 22).

[69] J. Autschbach, *J. Chem. Phys.* **2012**, *136*, 150902 (cit. on p. 22).

[70] S. F. Dyubko, V. A. Efremov, V. G. Gerasimov, K. B. MacAdam, *J. Phys. B: At. Mol. Opt. Phys.* **2005**, *38*, 1107 (cit. on p. 24).

[71] E. E. Salpeter, H. A. Bethe, *Phys. Rev.* **1951**, *84*, 1232–1242 (cit. on p. 27).

[72] H. Bethe, E. Salpeter, *An Introduction to Relativistic Quantum fField Theory. Quantum Mechanics of Two-Electron Atoms*, Springer, Berlin, **1957** (cit. on p. 27).

[73] M. Gell-Mann, F. Low, *Phys. Rev.* **1951**, *84*, 350–354 (cit. on p. 27).

[74] P. Knowles, M. Schütz, H.-J. Werner, *Modern methods and algorithms of quantum chemistry* **2000**, *3*, 97–179, http://www.fz-juelich.de/nic-series (cit. on pp. 29, 30).

[75] E. A. Hylleraas, (Ed.: P.-O. Löwdin), Advances in Quantum Chemistry, Academic Press, **1964**, pp. 1–33 (cit. on p. 31).

[76] G. Breit, *Phys. Rev.* **1932**, *39*, 616–624 (cit. on p. 32).

[77] G. E. Brown, D. G. Ravenhall, *Proceedings of the Royal Society of London A: Mathematical Physical and Engineering Sciences* **1951**, *208*, 552–559 (cit. on p. 34).

[78] J. Sucher, *Phys. Rev. A* **1980**, *22*, 348–362 (cit. on p. 34).

[79] J.-L. Heully, I. Lindgren, E. Lindroth, A.-M. Mårtensson-Pendrill, *Phys. Rev. A* **1986**, *33*, 4426–4429 (cit. on p. 34).

[80] P. J. Mohr, *At. Data Nucl. Data Tables* **1983**, *29*, 453–466 (cit. on p. 34).

[81] L. W. Fullerton, G. A. Rinker, *Phys. Rev. A* **1976**, *13*, 1283–1287 (cit. on p. 35).

[82] V. M. Shabaev, I. I. Tupitsyn, V. A. Yerokhin, *Phys. Rev. A* **2013**, *88*, 012513 (cit. on p. 35).

[83] CPC International Program Library, **2016**, http://www.cpc.cs.qub.ac.uk/ (cit. on pp. 35, 90).

[84] V. Shabaev, I. Tupitsyn, V. Yerokhin, *Comput. Phys. Comm.* **2015**, *189*, 175–181 (cit. on p. 35).

[85] F. A. Parpia, M. Tong, C. F. Fischer, *Phys. Rev. A* **1992**, *46*, 3717–3724 (cit. on p. 35).

[86] V. Shabaev, *Soviet Journal of Nuclear Physics* **1988**, *47*, 69–72 (cit. on p. 35).

[87] V. M. Shabaev, *Phys. Rev. A* **1998**, *57*, 59–67 (cit. on p. 35).

[88] C. W. P. Palmer, *J. Phys. B: At. Mol. Phys.* **1987**, *20*, 5987, http://stacks.iop.org/0022-3700/20/i=22/a=011 (cit. on p. 35).

[89] A. Papoulia, B. G. Carlsson, J. Ekman, *(accepted for publication in Phys. Rev. A) arXiv:1604.03740 [physics.atom-ph]* **2016**, http://arxiv.org/abs/1604.03740 (cit. on p. 35).

[90] A. Salam et al., *From a life of Physics*, World Scientific, **1989** (cit. on p. 40).

[91] J. C. Slater, *Phys. Rev.* **1929**, *34*, 1293–1322 (cit. on p. 42).

[92] E. U. Condon, *Phys. Rev.* **1930**, *36*, 1121–1133 (cit. on p. 42).

[93] P.-O. Löwdin, *Phys. Rev.* **1955**, *97*, 1474–1489 (cit. on p. 42).

[94] U. Fano, *Phys. Rev.* **1965**, *140*, A67–A75 (cit. on p. 46).

[95] W. Robb, *Comput. Phys. Comm.* **1973**, *6*, 132–148 (cit. on p. 46).

[96] G. Gaigalas, Z. Rudzikas, C. F. Fischer, *J. Phys. B: At. Mol. Opt. Phys.* **1997**, *30*, 3747 (cit. on p. 51).

[97] G. Gaigalas, S. Fritzsche, Z. Rudzikas, *At. Data Nucl. Data Tables* **2000**, *76*, 235–269 (cit. on p. 51).

[98] G. Gaigalas, S. Fritzsche, I. P. Grant, *Comput. Phys. Comm.* **2001**, *139*, 263–278 (cit. on p. 51).

[99] E. R. Davidson, *J. Comp. Phys.* **1975**, *17*, 87–94 (cit. on p. 53).

[100] I. P. Grant, H. M. Quiney, (Eds.: D. Bates, B. Bederson), Advances in Atomic and Molecular Physics, Academic Press, **1988**, pp. 37–86 (cit. on p. 54).

[101] K. G. Dyall et al., *Comput. Phys. Comm.* **1, 1989**, *55*, 425–456 (cit. on pp. 54, 55, 75, 77, 91).

[102] J. Olsen, B. O. Roos, P. Jørgensen, H. J. A. Jensen, *J. Chem. Phys.* **1988**, *89*, 2185–2192 (cit. on p. 60).

[103] P. Å. Malmqvist, *Int. J. Quantum Chem.* **1986**, *30*, 479–494 (cit. on pp. 61, 81).

[104] P.-O. Löwdin, *Phys. Rev.* **1955**, *97*, 1509–1520 (cit. on p. 61).

[105] U. I. Safronova, I. M. Savukov, M. S. Safronova, W. R. Johnson, *Phys. Rev. A* **2003**, *68*, 062505 (cit. on p. 62).

[106] E. P. Ivanova, *At. Data Nucl. Data Tables* **2011**, *97*, 1–22 (cit. on p. 62).

[107] X.-B. Ding et al., *J. Phys. B: At. Mol. Opt. Phys.* **2012**, *45*, 035003 (cit. on p. 62).

[108] E. P. Ivanova, *At. Data Nucl. Data Tables* **2009**, *95*, 786–804 (cit. on p. 62).

[109] D. Layzer, *Annals of Physics* **1959**, *8*, 271–296 (cit. on p. 63).

[110] D. Layzer, J. Bahcall, *Annals of Physics* **1962**, *17*, 177–204 (cit. on p. 63).

[111] H. T. Doyle, (Eds.: D. Bates, I. Estermann), Advances in Atomic and Molecular Physics, Academic Press, **1969**, pp. 337–413 (cit. on p. 63).

[112] T. Carette et al., *Phys. Rev. A* **2010**, *81*, 042522 (cit. on p. 65).

[113] T. Carette, M. R. Godefroid, *J. Phys. B: At. Mol. Opt. Phys.* **2013**, *46*, 095003 (cit. on p. 65).

[114] T. Carette, M. R. Godefroid, *Phys. Rev. A* **2014**, *89*, 052513 (cit. on p. 65).

[115] I. P. Grant, *J. Phys. B: At. Mol. Phys.* **1974**, *7*, 1458 (cit. on pp. 70, 72–74, 77).

[116] J. Olsen et al., *Phys. Rev. E* **1995**, *52*, 4499–4508 (cit. on p. 81).

[117] P. Jönsson, C. Froese Fischer, *Phys. Rev. A* **1998**, *57*, 4967–4970 (cit. on p. 81).

[118] P. Jönsson, X. He, C. Froese Fischer, I. P. Grant, *Comput. Phys. Comm.* **1, 2007**, *177*, 597–622 (cit. on pp. 81, 91).

[119] P. Jönsson et al., *Comput. Phys. Comm.* **2013**, *184*, 2197–2203 (cit. on pp. 81, 82, 90, 91, 118).

[120] I. Grant, University of Oxford, Unpublished updated version of the book "Relativistic Quantum Theory of Atoms and Molecules" (2007) (private communication), **2016** (cit. on p. 81).

[121] M. F. Gu, *Can. J. Phys.* **2008**, *86*, 675–689 (cit. on pp. 82, 90, 166).

[122] T. Brage, J. Fleming, R. Hutton, *Mol. Phys.* **2000**, *98*, 1057–1065 (cit. on p. 84).

[123] P. Beiersdorfer, J. R. C. López-Urrutia, E. Träbert, *Astrophys. J.* **2016**, *817*, 67 (cit. on pp. 87, 156).

[124] T. Brage, P. G. Judge, C. R. Proffitt, *Phys. Rev. Lett.* **2002**, *89*, 281101 (cit. on p. 87).

[125] S. S. Hodgman et al., *Phys. Rev. Lett.* **2009**, *103*, 053002 (cit. on p. 87).

[126] B. B. Jensen et al., *Phys. Rev. Lett.* **2011**, *107*, 113001 (cit. on p. 88).

[127] E. Bäckström et al., *Phys. Rev. Lett.* **2015**, *114*, 143003 (cit. on p. 88).

[128] C. F. Fischer, *Can. J. Phys.* **1973**, *51*, 1238–1243 (cit. on p. 89).

[129] S. Kotochigova, K. P. Kirby, I. Tupitsyn, *Phys. Rev. A* **2007**, *76*, 052513 (cit. on pp. 90, 92).

[130] GitHub, Inc. ©2016, **2016**, https://github.com/ (cit. on pp. 90, 118).

[131] M. Kozlov, S. Porsev, M. Safronova, I. Tupitsyn, *Comput. Phys. Comm.* **2015**, *195*, 199–213 (cit. on p. 90).

[132] CI-MBPT @ CPC International Program Library, **2015**, http://cpc.cs.qub.ac.uk/summaries/AEWV_v1_0.html (cit. on p. 90).

[133] GRASP2K, version 1_1 @ CPC International Program Library, **2013**, http://cpc.cs.qub.ac.uk/summaries/ADZL_v1_1.html (cit. on p. 90).

[134] FAC @ GitHub, **2016**, https://github.com/fnevgeny/fac (cit. on p. 90).

[135] cFAC @ GitHub, **2016**, https://github.com/fnevgeny/cfac (cit. on p. 90).

[136] The GNU Scientific Library: GSL, **2016**, http://www.gnu.org/software/gsl (cit. on p. 90).

[137] J. Desclaux, P. Indelicato, MCDFGME V 2005.10, **2005**, http://dirac.spectro.jussieu.fr/mcdf/mcdf_code/mcdfgme_accueil.html (cit. on p. 90).

[138] S. Fritzsche, *Comput. Phys. Comm.* **2012**, *183*, 1525–1559 (cit. on p. 90).

[139] I. Grant et al., *Comput. Phys. Comm.* **1980**, *21*, 207–231 (cit. on p. 91).

[140] F. A. Parpia, C. F. Fischer, I. P. Grant, *Comput. Phys. Comm.* **1996**, *94*, 249–271 (cit. on p. 91).

[141] P. Jönsson, X. He, C. Froese Fischer, The grasp VU package, tech. rep., technical report DOE/ER/US, Department of Energy, **1998** (cit. on p. 91).

[142] The CompAS team, The international collaboration on Computational Atomic Structure (CompAS), **2016**, http://ddwap.mah.se/tsjoek/compas/index.php (cit. on pp. 91, 115, 118).

[143] L. Filippin, M. Godefroid, J. Ekman, P. Jönsson, *Phys. Rev. A* **2016**, *93*, 062512 (cit. on p. 93).

[144] C. F. Fischer, *Phys. Scr.* **2009**, *2009*, 014019 (cit. on p. 96).

[145] J. Ekman, M. R. Godefroid, H. Hartman, *Atoms* **2014**, *2*, 215 (cit. on p. 96).

[146] H. Nagaoka, Y. Sugiura, T. Mishima, *Japan. J. Phys.* **1923**, *2*, 121 (cit. on p. 97).

[147] H. Nagaoka, Y. Sugiura, *Japan. J. Phys.* **1923**, 2, 167 (cit. on p. 97).

[148] H. Nagaoka, Y. Sugiura, T. Mishima, *Nature* **1924**, *113*, 459–460 (cit. on p. 97).

[149] T. T. Inamura, *Hyperfine Interactions* **2000**, *127*, 31–34 (cit. on p. 97).

[150] W. Pauli, *Naturwissenschaften* **1924**, *12*, 741–743 (cit. on p. 98).

[151] J. Bieroń, P. Pyykkö, P. Jönsson, *Phys. Rev. A* **2005**, *71*, 012502 (cit. on p. 98).

[152] J. Bieroń, P. Pyykkö, *Phys. Rev. A* **2005**, *71*, 032502 (cit. on p. 98).

[153] J. Bieroń et al., *Phys. Rev. A* **2001**, *64*, 052507 (cit. on p. 98).

[154] J. Bieroń, P. Pyykkö, *Phys. Rev. Lett.* **2001**, *87*, 133003 (cit. on p. 98).

[155] J. Bieroń, C. F. Fischer, I. P. Grant, *Phys. Rev. A* **1999**, *59*, 4295–4299 (cit. on p. 98).

[156] R. L. Kurucz, *Phys. Scr.* **1993**, *1993*, 110 (cit. on pp. 98, 136).

[157] P. Zeeman, *Nature* **1897**, *55*, 347 (cit. on p. 98).

[158] P. Zeeman, *Philosophical Magazine Series 5* **1897**, *43*, 226–239 (cit. on p. 98).

[159] M. Andersson, P. Jönsson, H. Sabel, *J. Phys. B: At. Mol. Opt. Phys.* **2006**, *39*, 4239 (cit. on pp. 99, 137).

[160] M. Andersson, T. Lennartsson, H. Nilsson, C. Chen, *J. Phys. B: At. Mol. Opt. Phys.* **2012**, *45*, 135001 (cit. on pp. 99, 137).

[161] C. Schwartz, *Phys. Rev.* **1955**, *97*, 380–395 (cit. on pp. 101, 103).

[162] L. Armstrong, jr, *Theory of the hyperfine structure of free atoms*, New York: Wiley-Interscience, **1971** (cit. on pp. 101–103, 105).

[163] I. Lindgren, A. Rosén, *Case studies in atomic physics* **1974**, *4*, 93–149 (cit. on pp. 101–103).

[164] I. Lindgren, A. Rosén, *Case studies in atomic physics* **1974**, *4*, 150–197 (cit. on pp. 101, 103).

[165] I. I. Sobelman, *Atomic Spectra and Radiative Transitions*, Springer-Verlag Berlin Heidelberg New York 1979, **1979** (cit. on p. 104).

[166] N. J. Stone, tech. rep. INDC(NDS)-0658, IAEA, Vienna, **2014**, https://www-nds.iaea.org/publications/indc/indc-nds-0658 (cit. on pp. 104, 124, 131).

[167] M. Godefroid, G. Van Meulebeke, P. Jönsson, C. Froese Fischer, *Z. Phys. D - Atoms Molecules and Clusters* **1997**, *42*, 193–201 (cit. on pp. 104, 137).

[168] D. M. Chipman, *Phys. Rev. A* **1989**, *39*, 475–480 (cit. on p. 104).

[169] D. Wintgen, H. Friedrich, *J. Phys. B: At. Mol. Opt. Phys.* **1986**, *19*, 1261 (cit. on p. 105).

[170] W. R. S. Garton, F. S. Tomkins, *Astrophys. J.* **1969**, *158*, 839 (cit. on p. 105).

[171] K. T. Cheng, W. J. Childs, *Phys. Rev. A* **1985**, *31*, 2775–2784 (cit. on p. 105).

[172] Q. Wu, G. W. F. Drake, *J. Phys. B: At. Mol. Opt. Phys.* **2007**, *40*, 393 (cit. on pp. 107, 125, 128, 132).

[173] J. Grumer, *to be submitted to Comp. Phys. Comm.* **2016** (cit. on pp. 115, 117, 119).

[174] G. Wilson et al., *PLoS Biol* **2014**, *12*, e1001745 (cit. on p. 115).

[175] GNU Make, **2016**, http://www.gnu.org/software/make (cit. on p. 115).

[176] GDB - the GNU Project debugger, **2016**, https://www.gnu.org/software/gdb (cit. on p. 115).

[177] Vim - the ubiquitous text editor, **2016**, http://www.vim.org/ (cit. on p. 116).

[178] GNU Emacs - an extensible, customizable, free/libre text editor, **2016**, https://www.gnu.org/software/emacs (cit. on p. 116).

[179] Git - an open source distributed version control system, **2016**, https://git-scm.com (cit. on p. 116).

[180] M. Andersson, P. Jönsson, *Comput. Phys. Comm.* **2008**, *178*, 156–170 (cit. on pp. 117–119, 122, 125).

[181] M. Metcalf, J. Reid, M. Cohen, *Modern Fortran Explained*, Oxford University Press, **2011** (cit. on p. 117).

[182] D. J. Worth, State of the art in object oriented programming with Fortran, tech. rep., Technical Report, Science and Technology Facilities Council, 2008. RAL-TR-2008-002, **2008**, http://epubs.cclrc.ac.uk (cit. on p. 117).

[183] B. U. o. C. D. Univ. of Tennessee; Univ. of California, N. Ltd., LAPACK - the Linear Algebra PACKage, **2016**, http://www.netlib.org/lapack (cit. on pp. 118, 121).

[184] F. Robicheaux, T. W. Gorczyca, M. S. Pindzola, N. R. Badnell, *Phys. Rev. A* **1995**, *52*, 1319–1333 (cit. on p. 120).

[185] P. Indelicato, F. Parente, R. Marrus, *Phys. Rev. A* **1989**, *40*, 3505–3514 (cit. on p. 120).

[186] J. P. Marques, F. Parente, P. Indelicato, *Phys. Rev. A* **1993**, *47*, 929–935 (cit. on p. 120).

[187] W. R. Johnson, K. T. Cheng, D. R. Plante, *Phys. Rev. A* **1997**, *55*, 2728–2742 (cit. on pp. 120, 125, 127, 131, 134).

[188] The GNU Operating System - by the Free Software Foundation, **2016**, https://www.gnu.org (cit. on p. 121).

[189] Ubuntu (GNU/Linux distribution), **2016**, http://www.ubuntu.com (cit. on p. 121).

[190] CentOS (GNU/Linux distribution), **2016**, https://www.centos.org (cit. on p. 121).

[191] OpenSUSE (GNU/Linux distribution), **2016**, https://www.opensuse.org (cit. on p. 121).

[192] Gfortran - the GNU Fortran project of the GNU Compiler Collection (GCC), **2016**, https://gcc.gnu.org/fortran (cit. on p. 121).

[193] G. Gaigalas, T. Žalandauskas, Z. Rudzikas, *At. Data Nucl. Data Tables* **2003**, *84*, 99–190 (cit. on p. 125).

[194] H. Karlsson, U. Litzén, *J. Phys. B: At. Mol. Opt. Phys.* **2001**, *34*, 4475 (cit. on pp. 135–139, 141).

[195] A. Abt, *Astrophys. J.* **1952**, *115*, 199 (cit. on p. 136).

[196] H. Hühnermann, *Phys. Scr.* **1993**, *1993*, 70 (cit. on p. 136).

[197] G. M. Wahlgren, *Memorie della Societa Astronomica Italiana Supplementi* **2005**, *8*, 108, http://adsabs.harvard.edu/abs/2005MSAIS...8..108W (cit. on p. 136).

[198] A. Aboussaïd et al., *Phys. Scr.* **1996**, *53*, 28 (cit. on p. 137).

[199] T. Brage, M. Andersson, R. Hutton American Institute of Physics Conference Series, (Eds.: S. Zhu, J. Yan), **2009**, pp. 18–28 (cit. on pp. 137, 147).

[200] C. M. Jomaron, M. M. Dworetsky, C. S. Allen, *MNRAS* **1999**, *303*, 555–564 (cit. on pp. 142, 143).

[201] J. X. Prochaska, A. McWilliam, *Astrophys. J. Letters* **2000**, *537*, L57 (cit. on p. 142).

[202] K. Townley-Smith, G. Nave, J. C. Pickering, R. J. Blackwell-Whitehead, *MNRAS* **2016**, *461*, 73–78 (cit. on p. 143).

[203] R. A. Holt, T. J. Scholl, S. D. Rosner, *MNRAS* **1999**, *306*, 107–111 (cit. on p. 143).

[204] G. Nave, C. J. Sansonetti, U. Griesmann, *Fourier Transform Spectroscopy OSA Tech. Digest Ser.* **1997**, *3*, 38–40, https://www.nist.gov/node/693721 (cit. on p. 143).

[205] W. Livingston, L. Wallace, *An atlas of the solar spectrum in the infrared from 1850 to 9000 cm-1 (1.1 to 5.4 micrometer)*, **1991** (cit. on p. 144).

[206] B. Gustafsson et al., *A&A* **2008**, *486*, 951–970 (cit. on p. 143).

[207] U. Heiter et al., *J. Phys.: Conf. Ser.* **2008**, *130*, 012011 (cit. on p. 144).

[208] V. M. Placco et al., *Astrophys. J.* **2015**, *812*, 109 (cit. on p. 145).

[209] P. Beiersdorfer, J. H. Scofield, A. L. Osterheld, *Phys. Rev. Lett.* **2003**, *90*, 235003 (cit. on pp. 147, 155).

[210] T. Brage et al., *Astrophys. J.* **1998**, *500*, 507 (cit. on p. 152).

[211] M. Andersson, Y. Zou, R. Hutton, T. Brage, *Phys. Rev. A* **2009**, *79*, 032501 (cit. on pp. 152, 154).

[212] P. Amaro et al., *Phys. Rev. A* **2016**, *93*, 032502 (cit. on pp. 152, 154).

[213] S. Schippers et al., *Proposal to GSI G-PAC 40* **2011** (cit. on p. 152).

[214] D. Bernhardt et al., *J. Phys.: Conf. Ser.* **2012**, *388*, 012007 (cit. on p. 152).

[215] S. Schippers, *AIP Conf. Proc.* **2013**, *1545*, 7–16 (cit. on p. 152).

[216] C. Laughlin, *Phys. Lett. A* **1980**, *75*, 199–200 (cit. on p. 154).

[217] J. Li, C. Dong, P. Jönsson, G. Gaigalas, *Phys. Lett. A* **2011**, *375*, 914–917 (cit. on p. 158).

[218] S. Schippers et al., *Phys. Rev. Lett.* **2007**, *98*, 033001 (cit. on p. 158).

[219] S. Schippers et al., *Phys. Rev. A* **2012**, *85*, 012513 (cit. on p. 158).

[220] J. Li, T. Brage, P. Jönsson, Y. Yang, *Phys. Rev. A* **2014**, *90*, 035404 (cit. on p. 159).

[221] J. Li et al., *Phys. Rev. A* **2012**, *86*, 052523 (cit. on p. 160).

[222] C. J. Schrijver et al., *Astrophys. J.* **2008**, *675*, 1637 (cit. on p. 161).

[223] P. Judge, R. Hutton, W. Li, T. Brage, submitted to *Astrophys. J.* **2016** (cit. on p. 163).

[224] Y. Ralchenko, *Modern Methods in Collisional-Radiative Modeling of Plasmas*, *Vol. 90*, Springer, **2016** (cit. on p. 166).

[225] H. P. Warren, D. H. Brooks, *Astrophys. J.* **2009**, *700*, 762 (cit. on p. 166).

[226] H. P. Warren, D. H. Brooks, A. R. Winebarger, *Astrophys. J.* **2011**, *734*, 90 (cit. on p. 166).

LIST OF ACRONYMS

ASF	*atomic state function*
AS	*active set*
CAS	*complete active space*
CCC	*core-core correlation*
CC	*coupled cluster*
CI	*configuration interaction*
CME	*coronal mass ejection*
CompAS	*the Computational Atomic Structure group*
CPC-IPL	*Computer Physics Communications International Program Library*
CSF	*configuration state function*
CVC	*core-valence correlation*
DCB	*Dirac-Coulomb-Breit*
DC	*Dirac-Coulomb*
DFT	*density functional theory*
DHF	*Dirac-Hartree-Fock*
D	*double*
E1	*electric dipole*
E2	*electric quadrupole*
E3	*electric octupole*
E4	*electric hexadecapole*
EBIT	*electron-beam ion trap*
EOL	*extended optimal level*
ESR	*electron spin resonance*
Grasp2k	*the General-purpose Relativistic Atomic Structure Package*
GSL	*GNU Scientific Library*
HFS	*hyperfine structure*

HF	*Hartree-Fock*
HIT	*hyperfine-induced transition*
HUM	*Hylleraas-Undheim-MacDonald*
IC	*intercombination*
ITER	*International Thermonuclear Experimental Reactor*
JET	*Joint European Torus*
M1	*magnetic dipole*
M2	*magnetic quadrupole*
M3	*magnetic octupole*
M4	*magnetic hexadecapole*
MBPT	*many-body perturbation theory*
MCDHF	*multiconfiguration Dirac-Hartree-Fock*
MCHF	*multiconfiguration Hartree-Fock*
MCSCF	*multiconfiguration self-consistent field*
MIT	*magnetic-field-induced transition*
MP-MBPT	*Møller-Plesset many-body perturbation theory*
MRI	*magnetic resonance imaging*
MR	*multireference*
NMR	*nuclear magnetic resonance*
NSF	*nuclear state function*
PSF	*perturbed state function*
Q	*quadruple*
QED	*quantum electrodynamics*
QMC	*quantum monte-carlo*
RAS	*restricted active space*
RCC	*relativistic coupled cluster*
RCI	*relativistic configuration interaction*
Rhyze	*the relativistic hyperfine-Zeeman code*
RMBPT	*relativistic many-body perturbation theory*
SCF	*self-consistent field*

SDO	*Solar Dynamics Observatory*
SD	*Slater determinant*
S	*single*
T	*triple*
UT	*unexpected transition*
VVC	*valence-valence correlation*
XUV	*extreme ultraviolet*

Printed by Media-Tryck, Lund University, Lund 2016
Nordic Ecolabel 3041 0903

This is a thesis on atoms and ions; how the atomic electrons interact with each other, with the nucleus, as well as with external magnetic fields, and ultimately how atomic systems interact with light for the purpose of studying laboratory and astrophysical spectra. I come originally from the county of Värmland in central Sweden and studied physics in Lund. This work was performed at the Department of Physics at Lund University and defended on the 21st of October 2016.

LUND UNIVERSITY

LUND UNIVERSITY
Department of Physics
Division of mathematical physics
ISBN 978-91-7623-996-4